**UNIVERSITY OF STRATHCLYDE**

Department of Physics

# Design, microfabrication and characterisation of Photonic Integrated Circuits

by

Giuseppe Cantarella
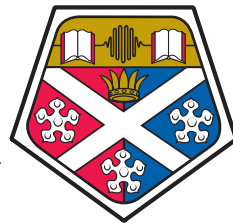


A thesis presented in fulfilment of the requirements for the degree of

*Doctor of Philosophy*

May 2017

This thesis is the result of the author's original research. It has been composed by the author and has not been previously submitted for examination which has led to the award of a degree.

The copyright of this thesis belongs to the author under the terms of the United Kingdom Copyright Acts as qualified by University of Strathclyde Regulation 3.50. Due acknowledgement must always be made of the use of any material contained in, or derived from, this thesis.

Signed: _____

Date: _____

## Acknowledgements

First of all, I would like to thank my supervisor, Dr. Michael Strain, for the excellent guidance and patience throughout this journey. The fantastic opportunity that was given to me has already changed the course of my life for the better, for that I'll be eternally grateful.

During my PhD I had the chance to meet some amazing people that I now consider not only colleagues but also friends. For their work, support and always interesting and productive discussions, I wish to particularly thank Paul Hill and John McPhillimy.

I'll always remember all the other guys from the Institute of Photonics that, even if not mentioned, will always have a place in my heart and in my memories.

I would also like to thank Prof. Marc Sorel and Charalambos Klitis, from the University of Glasgow, for the great work done together.

A particular thought goes to my family that have never tried to stop me from pursue my happiness and my personal gratification. Thanks for all your efforts and sorry for all the moments that, being so far away from you, I might have lost. I promise I'll do my best to always make you proud. Grazie.

Last but not least, Angela. Three years have gone and all my sweat and tears, all my screams and shouts, all my smiles and all my laugh, all the emotional breakdowns and all the physical catastrophes that have happened to me, and to us, during this period, have only been for you, my muse, my inspiration, my everything. This chapter of our lives is concluded and a bigger one is waiting for us...I am not scared of anything if you are by my side.

# Abstract

This doctoral dissertation deals with the design, fabrication and characterization of state-of-the-art Photonic Integrated Circuits (PICs) for non-linear applications.

Silicon PICs is a technology mainly used for application in telecommunications and quantum optics. The strong third order non-linearity of silicon makes it also attractive for non-linear PIC design. In FWM applications, SOI technology can be used not only for non-linear generation but also to fabricate photonic filters to remove the residual pump.

This thesis deals with three requirements for the realisation of on-chip FWM optical devices, the dual polarisation rejection of the pump on-chip and the integration and stabilisation of the FWM source and optical filter.

In this work two of the most used SOI photonic integrated filters, ring resonators and Bragg gratings, are presented. These devices present two different solutions for high extinction ($\approx 60$ dB) dual polarisation filtering. An integrated structure of non-linear source and filter is presented. The device used for non-linear generation is then monolithically integrated with a novel ring resonators cascade filter technology. FWM experiments were carried out obtaining an on chip pump high dual polarisation extinction of 62 dB with a low insertion loss for the propagating signal and idler of only 1.8 dB.

The realisation of a microprocessor feedback loop stabilisation system integrated with SOI non-linear structures is also demonstrated. The system is based on a local thermal heater element on-chip used to stabilise the PICs against thermal refractive index variations. Using this method, a silicon $\pi$-phase shifted grating with a cavity Q-factor of 40k is demonstrated to operate over an ambient temperature detuning range of $40\,^{o}$C and injection wavelength range of $1.5\,$nm, nearly 3 orders of magnitude greater than the resonant cavity linewidth.

The last part of this work is dedicated to the description of a custom made laser photolitography system for rapid prototyping of PIC designs, a tool designed to overcome the costs of the typical lithography systems and drastically decrease the time required for multiple micro-fabrications. The hardware and the software created for this tool are presented together with the first results on the fabrication of SU-8 Photoresist $(SU-8)$ on Silicon Dioxide $(SiO_2)$ waveguides, bends, Mach Zehnder interferometers and ring resonators.

# Contents

# List of Figures

xi

# List of Tables

# Abbreviations

| | |
|---|---|
| **CAD** | Computer-Aided Design |
| **CCD** | Charge-Coupled Device |
| **CMOS** | Complementary Metal Oxide Semiconductor |
| **CPUs** | Central Processing Units |
| **CROW** | Coupled Resonator Optical Waveguide |
| **CW** | Continuous Wave |
| **DLL** | Direct Laser Lithography |
| **EDFA** | Erbium Doped Fiber Amplifier |
| **FE** | Field Enhancement |
| **FFT** | Fast Fourier Transform |
| **FP** | Fabry Perot |
| **FWHM** | Full Width at Half Maximum |
| **FWM** | Four Wave Mixing |
| **HSQ** | Hydrogen Silsequioxen |
| **IR** | Infrared |
| **IT** | Information technology |
| **LED** | Light Emitting Diode |
| **MZI** | Mach Zehnder Interferometers |
| **NPA** | Nanophotonic Phased Array |
| **OD** | Optical Density |
| OH | Hydroxyl Group |
| **OSA** | Optical Spectrum Analyser |
| **PECVD** | Plasma Enhanced Chemical Vapour Deposition |
| **PIC** | Photonic Integrated Circuit |
| **PM** | Polarisation Maintaining |
| **Q-factor** | Quality Factor |
| **RIE** | Reactive Ion Etching |
| **ROI** | Region Of Interest |
| **RR** | Ring Resonator |
| **SEM** | Scanning Electron Microscopy |
| $SiO_2$ | Silicon Dioxide |
| **SOI** | Silicon on Insulator |
| $SU-8$ | SU-8 Photoresist |
| **TE** | Transverse Electric |
| **TM** | Transverse Magnetic |
| **TPA** | Two-photon absorption |
| **UV** | Ultraviolet |

# Chapter 1

# Introduction and background

## 1.1 Motivation and aim of the work

Information technology (IT) continues to follow Moore's Law of perpetually advancing computational performance within systems and devices. While computing systems in general and their Central Processing Units (CPUs) in particular continue to experience performance gains, the connections between them are nearing their physical limits [1]. The current tactic of adding an exponential number of cables to integrate and support a computing environment has resulted in performance bottlenecks, thermal and airflow issues as well as maintenance and cost ramifications [2]. In the last decade many big industrial companies like IBM [1] or INTEL [2], following this trend, focused their research on a new system of communication, the photonic integrated circuit.

A Photonic Integrated Circuit (PIC) is a device that integrates multiple photonic functions in a compact planar chip, and as such is analogous to an electronic integrated circuit. The major difference between the two is that a PIC provides functionality for information signals imposed on optical wavelengths typically in the visible spectrum or near infrared 850 nm - 1650 nm. PICs can allow optical systems to be made more compact and higher performance than with discrete optical components. They also offer the possibility of integration with electronic circuits to provide increased functionality [3].

Some of the main advantages of PICs with respect to the electonic circuits are certainly

the much bigger potential bandwidth and the absence of Joule effect. Next generation of processors will require a network of copper interconnections so dense that many industries (IBM, INTEL) are already exploring the idea to replace them with optical interconnections. PICs can therefore bring some advantages in field where integrated electronics already reached its limit, like telecommunication and computing.

The typical working wavelength is usually in the near-Infrared (IR) (between 1 µm and 1.6 µm). This is because of the absorption characteristic of the glass material used in the fibers. For short wavelengths Rayleigh scattering of inhomogeneities becomes important and towards Ultraviolet (UV) wavelengths electronic absorption starts to dominate, while around 1400 nm there is a strong absorption from Hydroxyl Group (OH) groups. This leaves two windows for telecommunication with similarly low absorption: one around 1300 nm and another one around 1500 nm . For longer IR wavelengths phenomena like absorption start to increase.

One of the benefits of this technology is that it is possible to fabricate state-of-the-art devices, even the more complicated, starting from a few main building blocks and just adding them together. Straight waveguides, bends, Bragg gratings and ring resonators represent some of the mainly used building block for the fabrication of complex PICs. The theory behind these structures and their major applications is the main topic of the next sections.

Silicon on Insulator (SOI) is one of the most mature and well developed photonic integration platforms [4, 5, 6, 7, 8], benefiting from the availability of Complementary Metal Oxide Semiconductor (CMOS) fabrication technology, where it is possible to use electronics fabrication facilities to make photonic circuitry [9]. The large refractive index contrast between the two materials allows a strong confinement of the optical mode to waveguide cross-sections with sub-micron dimensions, making SOI photonics an interesting technology for application in telecommunications [10, 11, 3], biosensing [12] and quantum optics [13, 14, 15].

The compatibility with a CMOS process allows the fabrication of complex structures, which represents the state of the art on the integration process. For example, it was recently demonstrated the possibility to create a large scale Nanophotonic Phased Array (NPA) consisting of $64 \times 64$ optical nanoantennas on a silicon chip [16]. All the 4,096 optical nanoantennas are tunable, it is therefore possible to balance them in power and align them

in phase to produce a sophisticated holographic radiation pattern [16]. This high level of integration reached by PIC opens the path towards the stage of computing and signal processing.

The idea of using PICs to implement logic functions and computing operations comes from the fact that electrical data transport has founds a bottleneck in bandwidth and power density [17]. Optical communications based on electronic-photonic systems can overcome these limitations. It has been demonstrated that, using a "zero-change" approach to the integration of photonics in the electronics manufacturing, fabricating the devices using the standard microprocessor foundry process, it is possible to create single-chip microprocessor that communicates directly using light [18].

PICs find their main application in telecommunication [17]. One example is represented by wavelength division multiplexed (WDM) fiber-optic communication systems, where an arrayed waveguide grating (AWG), fabricated using PICs technology is commonly used as optical multiplexers and de-multiplexers [19].

Due to their compatibility with the existing electronic integrated circuit technology, PICs are already used as a product to drive the new high speed communication market. An integration between both electronic and optic elements is in fact possible. PICs are for example involved in the latest 40G or 100 Gigabit Ethernet (100GbE) transceivers, devices used as interconnection between servers in all data centers [20]. PICs can be used not only on linear signal processing and data interconnection but can also find many applications in non-linear optics and quantum optics [15].

Quantum information science is based on the generation of quantum bits (qubits) and the realization of quantum gates in order to encode, transmit and process quantum information [21]. Photons, due to their low decoherence and high-speed transmission can be used as qubits and therefore quantum PICs can be fabricated [22]. Photonic qubits are easy to encode in many degrees of freedom like polarization [23], path [21], frequency [24] and orbital angular momentum [25]. One of the possible alternatives to generate qubits is through the use of single photon sources[15].

The importance of the use of PICs in quantum technology comes from the fact that

4

all the demonstrations referenced before relied on the use of inefficient and bulky devices to obtain single photon sources. Some examples could be represented by devices based on spontaneous parametric down conversion (SPDC), [26] single photon detectors based on avalanche photodiodes (APDs),[27] or optical circuits with bulk optical elements with very modest efficiency.

As well as in the telecommunication field, the practicality and scalability of quantum information technology requires the integration of individual components on a single chip. This is why PICs play a fundamental and promising role for future quantum information devices. The use of PICs enables a substantial improvement in performance and complexity of quantum photonic circuits and provides routes to scalability by the on-chip generation, manipulation and detection of quantum states of light [15].

PICs can be used in quantum technology with a variety of materials like silica-on-silicon [28, 29, 30], laser direct-writing silica [31], gallium nitride [32], lithium niobate [33], GaAs [34] and, last but not least, silicon-on-insulator [35, 36], used for its high $\chi^3$ non-linearity which is the starting point for applications like third harmonic generation or Four Wave Mixing (FWM).

It has been demonstrated, for example, that the generated signal and idler photons in a FWM process are correlated and their total energy must be equal to the one of the pump photons that created them [37]. This means that FWM can also be used to generate entangled photons [38, 39], key elements for Bell type experiments. The produced photon pair in a FWM experiments can also find applications in wavelength conversion [40, 41] and all-optical signal processing [42, 43]. The main topic of this doctoral dissertation is toward new technology for non-linear operations in PICs. This work is focused on presenting new technologies to obtain high-non-linear efficiency, routing of the produced photon pair, and pump rejection, all in the same integrated circuit.

My personal contribution is based on proposing solutions for three of the major problems encountered when working with non-linear optics and PICs; the control over the non linear process in order to obtain the maximum of efficiency, the stabilisation of this last process, and the rejection of the pump light used in the first step of the photon pair generation.

In order to maximise the non-linear efficiency, a selection of tunable SOI integrated devices is presented. These devices, as explained in the following chapters, allow operation at optimum condition for the non-linear process. Once the maximum efficiency is reached, it is necessary to stabilise the system against temperature and power shifts. In this work a stabilisation of silicon micro-resonators using a micro-processor based feedback control loop is therefore presented. Regarding the pump rejection this dissertation focuses on presenting a novel design of the well known photonic integrated filter based in SOI. On-chip silicon filters optimised for Transverse Electric (TE) polarisation have been demonstrated with high quality factors [44] and extinction values $\approx$ 45-50 dB [45, 46, 47, 48, 49]. High extinction values ($\approx$ 100 dB) have been reached in a few cases, using a grating filter coupled with two ring resonators [50] or using two $5^{th}$ order Coupled Resonator Optical Waveguide (CROW) filters on separate chips [51]. All of these results are optimised for TE rejection and do not take in account the light in the Transverse Magnetic (TM) polarisation. Significant scattering between the TE and TM modes, has been shown to occur in SOI waveguides, limiting polarisation extinction to $\approx$ 20 dB [52] due to the TE sensitivity to sidewall roughness in a typical SOI waveguide (220 nm $\times$ 500 nm). This effect leads to significant amount of light passing through the TE mode filter.

Within the presented scenario, this doctoral dissertation is therefore focused on the demonstration of high performance, state-of-the-art PICs fabricated for high-extinction, dual-polarisation operation, with application in FWM, and for active stabilization on high quality-factor cavity resonators.

## 1.2 Thesis outline

The dissertation is structured as follows:

In Chapter 2 all the main themes described in this introductory section will be detailed with their theory and applications. Descriptions of the functioning of the main PIC building blocks and of the main nonlinear effects, demonstrated in the following chapters, are provided.

In Chapter 3 the focus is on the performance of state-of-the-art, SOI, photonic integrated circuits. The effect of TE and TM polarised modes in standard ring resonator and Bragg

grating structures is presented and two dual-polarisation filter geometries with a high rejection ratio are demonstrated, with the aim of solving the filter polarisation mode dependency. The first dual polarisation filter is based on the implementation of plasmonic TM filters in a ring resonator geometry while the second is obtained from the superposition of specifically designed TE and TM Bragg gratings.

In Chapter 4, one of the devices developed and demonstrated in the previous chapter, will be used to demonstrate one of the many possible applications for these photonic integrated filters. In particular, results on nonlinear FWM experiments are demonstrated. In a typical spontaneous FWM application, the pump light on chip has a power in the order of 0 dBm while the produced photon-pair is in the order of -90 dBm [53]. In order to obtain a reasonable signal to noise ratio it is necessary to filter the pump light with a ratio of at least 100 dB. A device capable of filtering the pump light on chip below the detection limit for both TE and TM propagating mode, will be demonstrated in this chapter. In particular, a three ring cascade filter has been integrated with another ring for non-linear generation demonstrating a full monolithically integrated FWM source and pump filter system on-chip.

In Chapter 5, stabilisation of silicon micro-resonators using a micro-processor-based feedback control loop is presented. This process of stabilisation is a key requirement for the inclusion of PIC micro-resonator in larger photonic integrated circuits. In particular, thermal refractive index shift in non-linear applications can detune devices from their optimal working point. Using this method, a silicon $\pi$-phase shifted grating with a cavity Quality Factor (Q-factor) of 40 K is demonstrated to operate over an ambient temperature detuning range of $40\,°C$ and injection wavelength range of 1.5 nm, nearly 3 orders of magnitude greater than the resonant cavity linewidth.

The fabrication of the SOI waveguides investigated in this work did not take place in our laboratories. All the device were in fact fabricated in the James Watt Nanofabrication Centre at the University of Glasgow. During this work it was therefore necessary to find an easier way to rapidly prototype PICs without the need of involving a different research group or using expensive and complicated machinery (like the e-beam lithography) which are expensive and time consuming. This is the reason why, the work presented in the last chapter, Chapter 6,

deals with the description of a custom made laser lithography system used for microfabrication of PIC.

The direct laser lithography presented is a mask-less photolithography system that helps on cutting the cost of mask manufacturing and, as well as this, increases the achievable resolution with respect to the one obtained using mask aligner lithography, down to submicron dimensions [54]. The first part of the chapter deals with the description of all the system hardware and software including all the main fixed bugs. Once characterised, the system has been used to fabricate $SU-8$ on $SiO_2$ PIC-like straight waveguides, bends, Mach Zehnder Interferometers (MZI) and Ring Resonator (RR). All these devices have been then characterised and all the results are also presented in this chapter.

Finally, Conclusions about the presented results are given in Chapter 7, together with considerations on future activities and research.

# Chapter 2

# Photonic integrated circuits main building blocks

The following building block devices underpin the PIC design and application in the following chapters, so for ease of references, their operating principles are presented here.

## 2.1   Waveguides

A waveguide is a device designed to confine and direct the propagation of electromagnetic waves [7]. A full solution to the guided waves of the structure can be determined using Maxwell's equations but, for a general understanding, the theory of light guiding can be obtained using a more simple ray optics model [7].

Consider at first a light ray $E_i$ propagating in a medium with refractive index $n_1$ different from the refractive index $n_2$ of the outside area. When this ray of light scatters on the interface between the two media, at an angle $\theta_1$, part of the light is transmitted in $E_t$ and part is instead reflected in $E_r$. Snell's law indicates the relationship between the refractive indices $n_1$ and $n_2$, and the angles of incidence $\theta_1$ and refraction $\theta_2$:

$$n_1 \sin\theta_1 = n_2 \sin\theta_2 \ . \tag{2.1}$$

The process is described in the schematic presented in Figure 2.1.
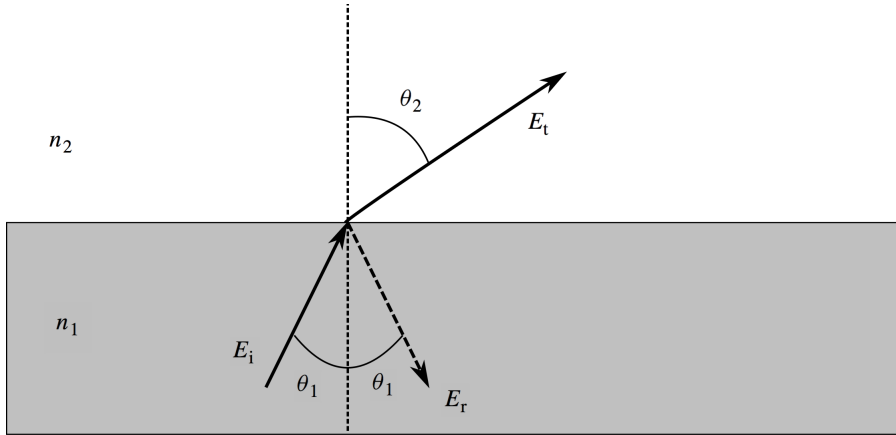
**Figure 2.1:** Simple schematic of Snell law applied to a straight waveguide

In the hypothesis that the refractive index of the fist medium ($n_1$) is higher than the refractive index of the second medium, it is possible to understand that increasing the incidence angle $\theta_1$ the corresponding $\theta_2$ will approach 90°. This equation leads to the definition of critical angle:

$$\sin\theta_c = \frac{n_2}{n_1} \ .$$
(2.2)

This angle represents the limit beyond which ligth is no longer transmitted and is instead trapped into the first medium in a phenomenon called total internal reflection [7]]. A schematic of this condition is presented in Figure 2.2.
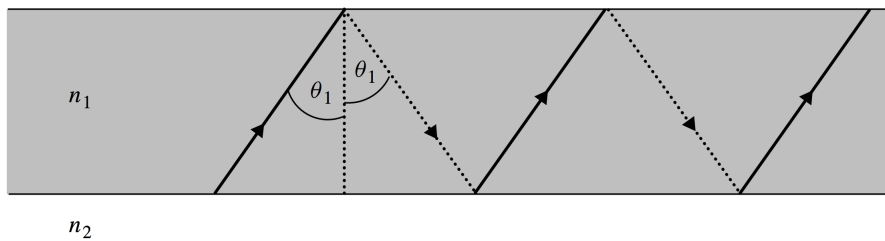


**Figure 2.2:** Simple schematic of critical coupling condition in a straight waveguide

This theory is the foundation of the waveguide functioning. A waveguide is in fact that device where the light is confined to a region of refractive index $n_1$ called core, higher than the refractive index $n_2$ of the surrounding material, called cladding. With further studies it will be clear how this is just a simplistic explanaition and that not all the light incident a

waveguide with an angle higher than $\theta_c$ can be propagated but rather the light propagation on a waveguide is quantized into optical modes. This condition is better expressed in:

$$2\kappa_0 n_1 h \cos(\theta_1 - \phi_u - \phi_l) = 2m\pi \ . \tag{2.3}$$

where m is an integer, h is the height of the waveguide, $\phi_u$ and $\phi_l$ are the phase shifts from the top and bottom facet of the core respectively and $\kappa_0$ is the wavevector in the direction of the wavefront. $\kappa_0$ It is related to wavelength, $\lambda$, by:

$$\kappa_0 = \frac{2\pi}{\lambda} \ . \tag{2.4}$$

From Eq. 2.4 it is possible to notice that, because m is an integer, only a discrete series of angles $\theta$ can solve the equation. For each solution there will therefore be a corresponding propagation constant in both orthogonal directions (for each polarisation). It is clear therefore that light can not propagate at any angle $\theta$, and that each allowed solution is known as a mode of propagation. The mode number is given by m and the relative polarisation. For example, $TE_0$ describes the fundamental mode or first order TE mode. When only one mode is allowed to propagate into the waveguide the structure is defined as single mode. The single mode condition is one of the first thing to look for when projecting the layout of a waveguide structure finalised to data communication and signal routing. Multimode light propagation structures usually have a relatively large light carrying core of several tens of microns and they are usually used for short distance transmissions with Light Emitting Diode (LED) based fiber optic equipment. Single-mode ligth carrier instead has a small light carrying core of microns to sub-microns scale and it can be used for long distance transmissions with laser diode based fiber optic transmission equipment.

It is possible to calculate which are the main constraint to obtain single mode propagation. The propagation of a guided mode in a waveguide can be associated to its propagation constant $\beta = \kappa n_{\text{eff}} = \frac{2\pi n_{\text{eff}}}{\lambda}$:

$$E = E_0 e^{-(\alpha + j\beta)L} \ . \tag{2.5}$$

where $n_{eff}$ is called effective index and represents the refractive index along the direction of propagation, and $\alpha$ is the attenuation constant.

The effective index is not constant and it has a dependency with the wavelength $\lambda$. This variation is expressed by the group index

$$n_g(\lambda) = n_{eff}(\lambda) - \lambda \frac{dn_{eff}}{d\lambda} \; . \tag{2.6}$$

All this parameters that describe the light propagation in a waveguide depend, apart from the chosen material, on the waveguide cross section geometry. Taking in consideration SOI waveguides, the technology used to fabricate the devices presented in this work, the light is confined in a silicon core, with refractive index of $n_{Si} = 3.47$ at $\lambda = 1550$ nm sorrounded by an $SiO_2$ cladding which has a refractive index of $n_{SiO_2} = 1.47$ at $\lambda = 1550$ nm and a low index top cladding (oxide or air). The high refractive index contrast between waveguide core and cladding allows a strong confinement in this small dimensions enabling light to be guided also in bends with very small radii without radiation losses.

The standard dimensions used for the waveguide presented in this work are 500 nm $\times$ 220 nm cross section size. As shown in the simulation presented in Chapter 4, a SOI waveguide with this geometry can be considered single mode with only a first order TE and TM mode propagating in its core at $\lambda \approx 1550$ nm. Some issues can arise due to this dual polarisation propagation and, as explained in the abstract, part of this work regards the study of novel design to overcome this problem.

## 2.2 Ring resonator

A ring resonator is formed when a straight waveguide is closed to form a circle or a racetrack shape. In a structure like this the light resonates with a precise frequency that is given from the fact that the optical path length is an integer number of wavelengths. From what was stated before it is possible to say that a resonance for the ring occurs when the phase $\phi$ is a multiple of $2\pi$, or when the wavelength is a whole number of the optical length of the ring:

$$\lambda_{res} = \frac{n_{eff}L}{m} \; . \tag{2.7}$$

With m integer, $n_{eff}$ the effective refractive index and L the round trip length.

A ring resonator is usually coupled to one or two waveguides. The coupling mechanism can be of different nature but in this work the rings are coupled to the waveguides using codirectional evanescent field coupling. Depending on the number of waveguides used in the ring resonator coupling the configuration takes different names. An all-pass ring resonator is the simpliest configuration and can be obtained by coupling one side of the ring resonator with a waveguide, as shown in Figure 2.3 (a). In this case the light is injected in the input waveguide and part of it is selectively trapped into the ring. The transmission spectrum (or through port) can be collected at the end of the injection waveguide and will show dips around the ring resonances. This ring resonator represents therefore a spectral filter, which can be used for applications in optical communications.
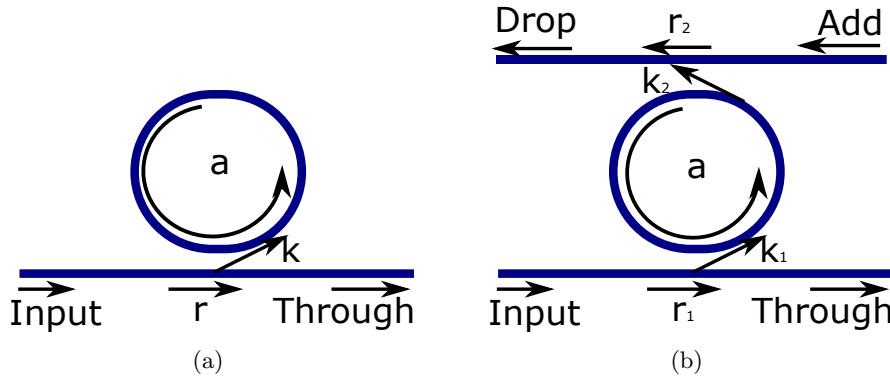


**Figure 2.3:** A simple schematic of All-pass, (a) and Add-drop (b) ring resonator.

Making some simple assumptions, for example that the reflections back into the waveguide are negligible, it is possible to calculate the spectral properties of an all-pass ring resonator assuming Continuous Wave (CW) operation and matching fields. Using these assumptions, the ratio of the transmitted and incident field in the bus waveguide can be calculated as:

$$\frac{E_{pass}}{E_{input}} = e^{i(\pi+\phi)} \frac{a - re^{-i\phi}}{1 - are^{-i\phi}} \ . \tag{2.8}$$

Where $\phi = \beta L$ represents the single-pass phase shift, L the round trip length and $\beta$ the propagation constant of the circulating mode. The term a is defined as the single-pass

13

amplitude transmission and it is a value that takes in account both propagation loss in the ring and loss in the couplers. This term is linked to the power attenuation coefficient $\alpha$ expressed in [1/cm] as $a^2 = \exp(-\alpha L)$.

The intensity transmission on the through port $T_t$ can be easily obtained by calcuating the square of Eq. 2.8:

$$T_t = \frac{I_{pass}}{I_{input}} = \frac{a^2 - 2ra\cos\phi + r^2}{1 - 2ra\cos\phi + (ar)^2} \; . \tag{2.9}$$

As it is possible to see, the transmission $T_t$ depends on the two terms related to the coupling on the ring resonator; r is defined as the self-coupling coefficient. Defining $\kappa$ as the cross-coupling coefficients, from these two last terms the power splitting ratio between the ring and the waveguide is calculated as $r^2$ and $\kappa^2$. To make this model valid, it is necessary to assume that these values satisfy the relationship $r^2 + \kappa^2 = 1$, this because is necessary to assume that there are no losses in the coupling section.

For ideal cavities with zero attenuation, $a \approx 1$, the transmission is unity for all values of detuning $\phi$. Under critical coupling when the coupled power is equal to the power loss in the ring $1 - a^2 = \kappa^2$ or $r = a$. the transmission at resonance drops to 0. The phase argument of the field transmission varies periodically with frequency. All-pass resonators delay incoming signals via the temporary storage of optical energy within the resonator. When the ring resonator is coupled to two waveguides, the incident field is partially transmitted to the drop port. Transmission for the through and drop prot can be calculated as [55]:

$$T_t = \frac{I_{pass}}{I_{input}} = \frac{r_2{}^2 a^2 - 2r_1 r_2 a\cos\phi + r_1{}^2}{1 - 2r_1 r_2 a\cos\phi + (r_1 r_2 a)^2} \; . \tag{2.10}$$

$$T_d = \frac{I_{drop}}{I_{input}} = \frac{(1 - r_1{}^2)(1 - r_2{}^2)a}{1 - 2r_1 r_2 a\cos\phi + (r_1 r_2 a)^2} \; . \tag{2.11}$$

The optimum condition for the ring coupling is when the ring is found to be at critical coupling, the condition where the round-trip loss factor of the ring is equal to the self-coupling coefficient

14

[56]. In this case, if the losses are negligible and $a \approx 1$ the critical coupling condition occurs at symmetric coupling ($\kappa_1 = \kappa_2$). If the losses are not negligible then the critical coupling occurs when $r_2 a = r_1$.

All the presented parameters have effect on the ring transmission and drop spectra illustrated in Figure: 2.4 compared with the transmission spectrum of an all pass ring resonator. In this case the value have been set to $a = 0.85, r = r_1 = r_2 = 0.9$.
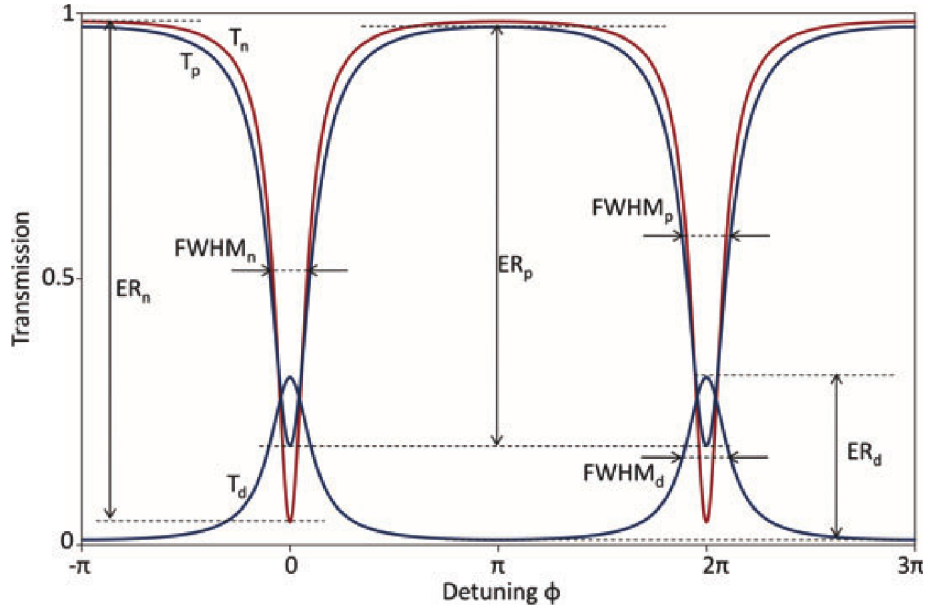


**Figure 2.4:** Transmission spectrum of an all-pass ring and the two outputs of add-drop ring with the important spectral features indicated. The spectra are plotted in function of the phase difference with the first resonance wavelength (indicated with 0 in the abscissa) [55].

As it is possible to see, the add-drop case presents a Full Width at Half Maximum (FWHM) that is slightly larger than the all pass case. This is due to the additional losses introduced by the second coupling section. The peak also presents a slightly smaller extinction (ratio between maximum and minimun power on the spectrum) due to the larger distance from the critical coupling condition.

The parameters presented in Figure: 2.4 can all be extracted from the equations used for the transmission intensity, Eq. 2.8, Eq. 2.10 and Eq. 2.11. The FWHM is calculated, for the

all-pass ring resonator as:

$$\text{FWHM}_{\text{allpass}} = \frac{(1 - \text{ra})\lambda_{\text{res}}{}^2}{\pi n_g L \sqrt{r_1 r_2} a} \ . \tag{2.12}$$

and for an add-drop ring resonator configuration:

$$\text{FWHM}_{\text{adddrop}} = \frac{(1 - r_1 r_2 a)\lambda_{\text{res}}{}^2}{\pi n_g L \sqrt{r_1 r_2 a}} \ . \tag{2.13}$$

The FSR, the spectral distance between two adiacent resonances, can be calculated as a function of the wavelength as:

$$\text{FSR} = \frac{\lambda^2}{L n_g} \ . \tag{2.14}$$

The group index, considered in this equation and already described in Eq. 2.7, takes in account the dispersion of the waveguide while, the corresponding group velocity, described as:

$$v_g = \frac{c}{n_g} \ . \tag{2.15}$$

is an indicator of the velocity at which the envelope of a propagating pulse travels. Both group index and group velocity are characteristics of the dispersive medium (or waveguide).

Another parameter to extrapolate from the spectra in Figure: 2.4 is the Q-factor, it describes the sharpness of the resonance relative to its central wavelength and can be expressed as:

$$Q - \text{factor} = \frac{\lambda_{\text{res}}}{\text{FWHM}} \ . \tag{2.16}$$

The Q-factor also physically represents the number of oscillations of the field before the circulating energy is depleted to $1/e$ of the initial energy.

Concentrating the attention on SOI ring resonators it is possible to obtain a full description of the losses that can be divided in different values. When light propagates in a ring resonator the losses can be divided in waveguide propagation losses, losses in the coupling section, originating from propagation losses, and bend losses due to mismatch losses at the straight-

bend transition. The propagation losses are usually dependent on the waveguide sidewall roughness and any mismatch in the waveguide width caused by the fabrication process. The loss for a roundtrip can therefore be calculated as:

$$a[dB] = a_{propagation}L + 2a_{coupler} + 4a_{bend} \ . \tag{2.17}$$

with $a_{propagation}$ the propagation loss per unit of length expressed in [dB/cm]. The calculated Q-factor, obtained in Eq. 2.16 can be rewritten using Eq. 2.12 to show the high dependency that this terms has with the ring resonator losses. From the equations it is clear that it is necessary to reduce the losses in the ring to obtain higher value for the Q-factor but unfortunately this value can only be adjusted up to a certain point. To adjust the Q-factor it is possible to increase the cavity length but doing so the propagation loss increases. Changing the geometrical parameters such as the ring radius and/or the coupling length it is therefore possible to design a ring resonator with very specific features in terms of loss, Q-factor, FSR and FWHM, parameters dependent on the application that the ring is designed for. Ring resonator are used to obtain a continual spectral filter. If instead a single pass filter is needed, the use of ring resonator is not recommended and, in that case, a better solution is represented by another photonic filter, the Bragg grating.

## 2.3   Bragg grating

Most of the Bragg gratings used in the telecommunication industry are fibre Bragg gratings (FBG). The Bragg gratings that have been fabricated for this work are instead based on PICs but the theory behind the properties of these devices is applicable in both cases. The brief theoretical overview on Bragg gratings presented here is more extensively demonstrated in [57] and [58]. A Bragg grating is a waveguide generally defined as a sinusoidal perturbation on the waveguide sidewalls, as shown in the SEM image of Figure 2.5 which generates a periodic modulation of the effective refractive index of the waveguide. The device pattern was defined using electron beam lithography with Hydrogen Silsequioxen (HSQ) as the resist layer, which was transferred to the silicon core by using Reactive Ion Etching (RIE) [59].
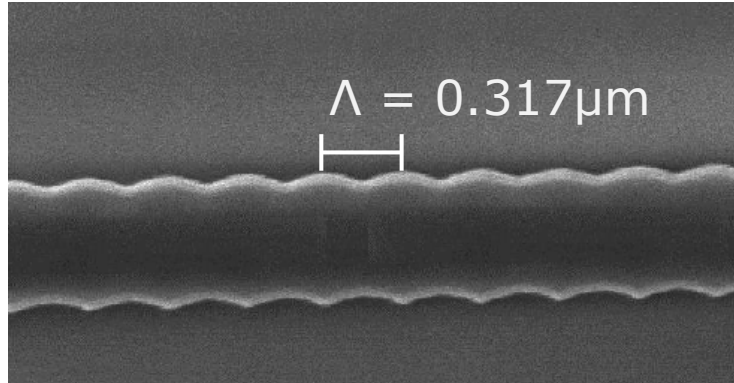
**Figure 2.5:** A SEM image of a SOI sidewall waveguide Bragg grating structure. The asymmetry between the two sidewall is due to a SEM optical artifact, the two sidewalls are fabricated to be identical within fabrication tolerances.

The changing width of the waveguide induces a local effective refractive index change and therefore local reflection points. Since this modulation is periodical, multiple reflections appear on the direction of propagation of the light with a correspondent phase change that is relative to this modulation and to the wavelength. All the reflected signals will be in phase when the wavelength is equal to a particular value called the Bragg wavelength; in this case all the signals add constructively and reflects in a direction opposite to the direction of propagation, with a center around the Bragg wavelength. All the other wavelength outside the Bragg grating stopband (defined and controlled by the waveguide width, the amplitude of the index perturbation, and the grating length) do not add constructively to the reflected signal and are therefore transmitted through the waveguide output.

A schematic of a Bragg grating with a description of all the parameters that is possible to control is given in Figure 2.6.
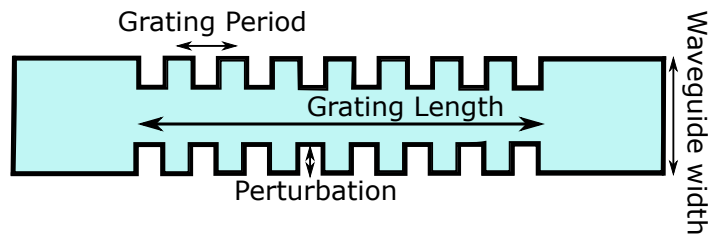


**Figure 2.6:** A schematic image of a waveguide Bragg grating structure showing all the possible control parameters.

In order to simplify the following theoretical description of the principles of a Bragg

grating, the discussion is limited to single mode, step index, uniform Bragg gratings with planes perpendicular to the waveguide direction of propagation.

Starting from the description given before on the basic principle of a Bragg grating it is possible to determine the Bragg wavelength using the principles of energy and momentum conservation. During the reflection at the grating planes, for the conservation of energy, is in fact impossible to observe any change in the frequency and, for the momentum conservation, the wavevector correspondent to the reflected wave $k_r$ must be equal to the sum of the grating wavevector $K$ and the wavevector relative to the incident light $\overrightarrow{k_i}$:

$$\overrightarrow{k_i} + \overrightarrow{K} = \overrightarrow{k_r} \ . \tag{2.18}$$

When the Bragg condition is satisfied all the incident ligth at that wavelength is reflected back and therefore: $\overrightarrow{k_r} = -\overrightarrow{k_i}$. At this condition Eq.2.21 can be rewritten as:

$$\frac{2\pi}{\lambda} n_{\text{eff}} + \frac{2\pi}{\Lambda} = -\frac{2\pi}{\lambda} n_{\text{eff}} \ . \tag{2.19}$$

Eq. 2.22 can therefore clearly rearranged in order to extrapolate an espression for the relationship between the Bragg wavelength, the effective refractive index and the grating period.

$$\lambda_B = 2 n_{\text{eff}} \Lambda \ . \tag{2.20}$$

Where $\lambda_B$ is the Bragg wavelength, $\Lambda$ is the grating period and $n_{\text{eff}}$ is the effective refractive index of the waveguide. It is necessary to remember that the effective refractive index that appears in Eq. 2.23 is not a constant but rather a function of the direction of propagation. Assuming that, in the case of forward propagation, this direction is along the z axis, the refractive index profile, $n_{\text{eff}}(z)$, along the Bragg grating, can be described by [60]:

$$\delta n_{\text{eff}}{}'(z) = \overline{\delta n_{\text{eff}}(z)}[1 + cos(Kz)] \ . \tag{2.21}$$

where $\overline{\delta n_{\text{eff}}(z)}$ is the refractive index perturbation averaged over a grating period.

The relationship described in Eq. 2.23 does not provide information on the grating stopband bandwidth or on the strength of the reflection. Coupled-mode theory can be used to model these optical properties for most gratings [61]. The relationship between the transmitted and reflected light in a Bragg grating can be imagined as a mode of amplitude $A_+(z)$ coupled into an identical counter-propagating mode of amplitude $B_+(z)$ that, for the coupled-mode theory follow the relationships in Eq. 2.22 and Eq. 2.23.

$$\frac{dA(z)}{dz} = i\hat{t}A(z) + i\kappa B(z) \ . \tag{2.22}$$

$$\frac{dB(z)}{dz} = i\hat{t}B(z) + i\kappa^* A(z) \ . \tag{2.23}$$

where $A(z) = A_+(z)\exp(i\gamma z), B(z) = B_+(z)\exp(-i\gamma z)$, and $\gamma = \beta - \frac{\pi}{\Lambda}$ is the detuning wavevector with $\beta$ the propagation constant. The two coupling coefficients $\kappa$ and $\hat{t}$ can be calculated, for sinusoidal variation of index perturbation along the waveguide as described in Eq. 2.24 and Eq. 2.25.

$$\kappa = \frac{\pi}{\lambda_B}(\eta \Delta_n) \ . \tag{2.24}$$

where $\eta$ is the fraction of the waveguide mode power confined to the grating.

$$\hat{t} = \delta + t \ . \tag{2.25}$$

where

$$t = \frac{2\pi \overline{\delta n_{eff}}}{\lambda} \ . \tag{2.26}$$

and

$$\delta = 2\pi n_{\text{eff}}\left(\frac{1}{\lambda} - \frac{1}{\lambda_B}\right) \ . \tag{2.27}$$

Assuming that at the output of the grating A(z)=1 and B(z) = 0 it is possible to calculate a

solution for Eq. 2.22 and Eq. 2.23, for a uniform grating of length L. From this solution it is possible to calculate the reflection coefficient ρ. This coefficient is given by ρ = B(L/2)/A(L/2) and it results in [60]:

$$\rho = \frac{\sinh^2(L\sqrt{\kappa^2 - \hat{t}^2})}{\cosh^2(L\sqrt{\kappa^2 - \hat{t}^2}) - \frac{\hat{t}^2}{\kappa^2}} \ . \tag{2.28}$$

An expression for the detuning, δ, can be obtained calculating the difference between the propagating wavelengths, λ, and the Bragg wavelength, $\lambda_B$ in the case of an infinitesimally weak grating. Eq. 2.22 and Eq. 2.23 also allow the maximum reflectivity to be calculated as:

$$R_{max} = |\rho|^2 = \tanh^2(\kappa L) \ . \tag{2.29}$$

This value is found at a correspondent wavelength of:

$$\lambda_{\max} = \left(1 + \frac{\overline{\delta n_{\text{eff}}}}{n_{\text{eff}}}\right)\lambda_B \ . \tag{2.30}$$

The Bragg grating transmission spectra can be obtained simply calculating in the ideal lossless case $|t|^2 = 1 - |r|^2$. Lumerica simulation for both spectra are shown in Figure2.7. Higher reflectivity (lower transmission) is obtained when the amplitude of the refractive index modulation is increased. It is also apparent the the bandwidth of the response is dependent on the grating parameters.
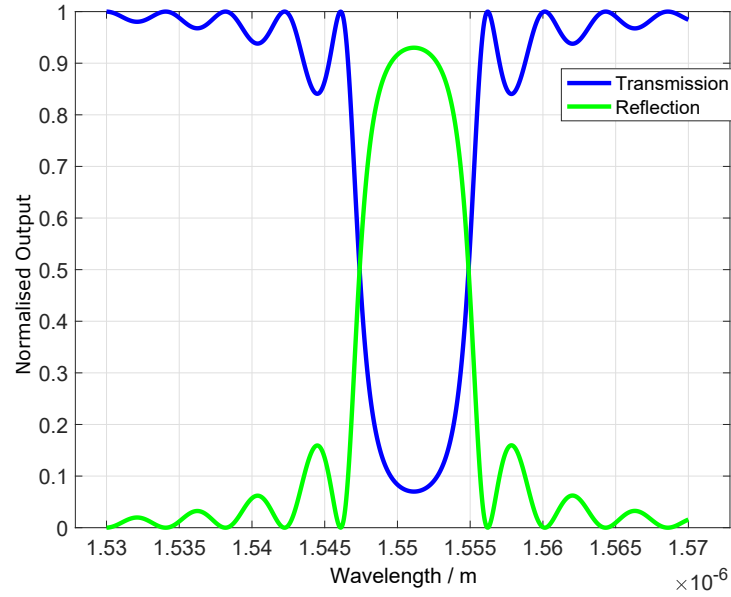
**Figure 2.7:** Simulations on Bragg gratings with perturbation of 6 nm, coupling coefficient $\kappa = 130 \ \text{cm}^{-1}$ for both reflection and transmission spectra.

Simulations on Bragg gratings with perturbation of 6 nm, coupling coefficient $\kappa = 130 \ \text{cm}^{-1}$ and varying length are shown in Figure2.8.
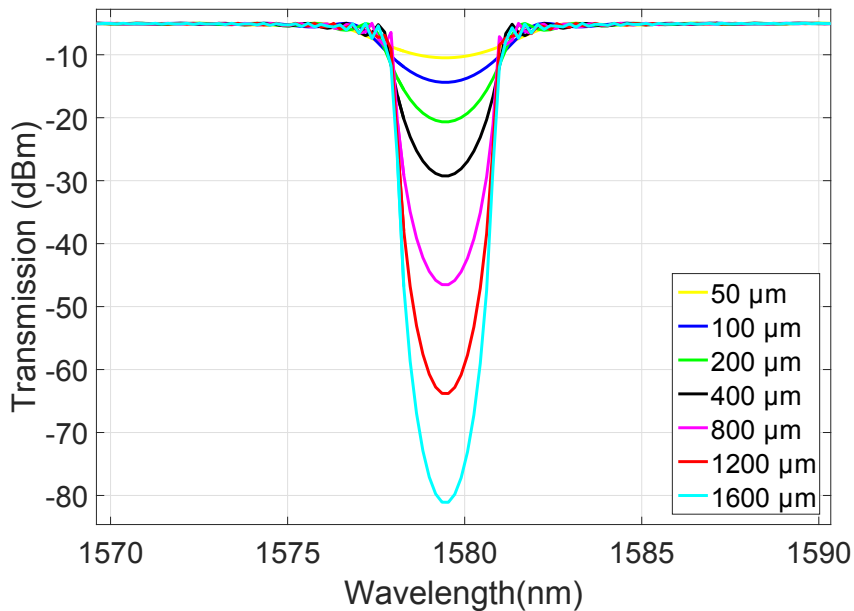


**Figure 2.8:** Simulated TE transmission spectra for Bragg grating devices with coupling coefficient $\kappa = 130 \ \text{cm}^{-1}$ and length varying from 50 µm to 1600 µm.

An estimation of the grating stopband bandwidth is calculated from the two maximum of

the transmission notch, correspondent to the zeros of the maximum reflectivity peak. This value is expressed as:

$$\frac{\Delta\lambda_0}{\lambda} = \frac{\overline{\delta n_{eff}}}{n_{eff}} \sqrt{1 + \left(\frac{\lambda}{\overline{\delta n_{eff}}L}\right)^2} \ . \tag{2.31}$$

For a low index perturbations the bandwidth is not dependent on index modulation. More accurately, for $\overline{\delta n_{eff}} << \frac{\lambda}{L}$ the first part of Eq. 2.31 can be expressed as:

$$\frac{\Delta\lambda_0}{\lambda} = \frac{\lambda}{n_{eff}L} \ . \tag{2.32}$$

Eq. 2.32 describes the limits of the bandwidth due to the grating length in the condition referred as the weak grating limit.

In the opposite case, for strong grating perturbation ($\overline{\delta n_{eff}} >> \frac{\lambda_D}{L}$ ) the modulation expressed in Eq. 2.31 reduces to:

$$\frac{\Delta\lambda_0}{\lambda} = \frac{\overline{\delta n_{eff}}}{n_{eff}} \ . \tag{2.33}$$

Eq. 2.33 describe how in this case the grating modulation is completely independent from its length. In this region, light which wavelength is in the stop-band does not penetrate the full length of the grating, this results in a reflectivity value tending towards 100 %.

Some other changes may be made to the Bragg grating structure in order to change its performance. In the case of a *chirped* [62] Bragg grating for example, the grating period is monotonically varied to produce a wider reflected band of wavelengths. The grating may also be *apodised* gradually decreasing the coupling coefficient from the centre towards both ends of the grating in order to suppress the spectrum sidelobes adjacent to the main reflection peak.[63].

## 2.4   Mach Zehnder interferometers

A typical MZI sensor is based on an optical waveguide that is split in two using a Y-junction. In a MZI a light beam is divided into two arms by a beamsplitter and then recombined by a

second beamsplitter. The transmission efficiency on the second beamsplitter will vary from 0% to 100% depending on the relative phase acquired by the beam along the two paths. MZIs, as well as a ring resonator, can be used as wavelength filters or as a device for non-linear applications [64]. The advantage of MZIs is that they are far less sensitive to thermal variations than rings, though they also typically have a much larger device footprint $\approx$ couple of mm [65].

The device is shown schematically in Figure 2.9
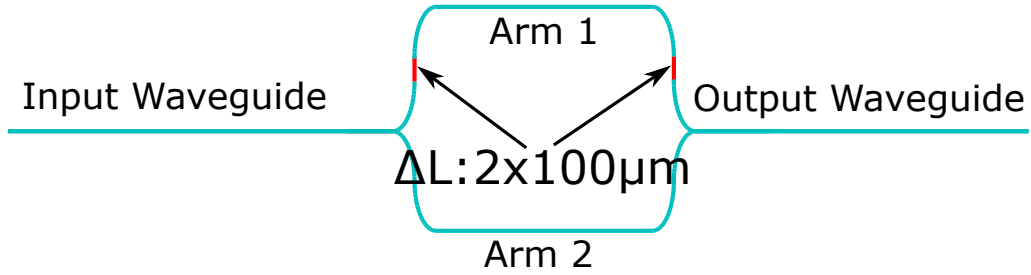


**Figure 2.9:** A schematic of a Mach Zehnder interferometer structure. $\Delta L$ represents the path length difference between arm 1 and arm 2 responsible for the phase shift generated in the electric field propagating in arm 1 with respect to the one propagating in arm 2.

Consider a single mode TE input wave propagating in the input waveguide. Assuming that the first Y-junction divides the wave evenly, the intensities in arm 1 and arm 2 of the interferometer will be the same. The electric fields $E_1$ and $E_2$ of both propagating modes in arm 1 and arm 2 of the interferometer will respectively be represented by:

$$E_1 = E_0 \sin(\omega t - \beta_1 z) \; .$$
$$E_2 = E_0 \sin(\omega t - \beta_2 z) \; . \tag{2.34}$$

The two fields are considered to have the same amplitude but different propagation constants. After the field separation in the first splitter, the two field $E_1$ and $E_2$ are in phase but, after the propagation in the respective arm they may no longer be in phase, either due to different refractive index in the arms, or due to different optical path lengths in the arms (like in the case considered in this work and shown in Figure 2.9). The intensity at the output waveguide, $S_T$, will therefore be calculated by:

$$S_T = (E_1 + E_2)^2 \; . \tag{2.35}$$

24

Assuming in the case treated in this work a different path lengths for the two waves, of $L_1$ and $L_2$. Expanding and substituting for $E_1$ and $E_2$ gives:

$$S_T = (E_0^2[1 + \cos(\beta_2 L_2 - \beta_1 L_1)]) . \qquad (2.36)$$

Using this equation it is possible to simulate the transmission spectra of a MZI in order to find the correct dimensions to use during the fabrication. A simulation where the path length change $\Delta L$ between the two arms has been fixed to 200 μm is shown in Figure 2.10. The plot is normalised to a maximum amplitude of 1. The term $(\beta_2 L_2 - \beta_1 L_1)$ represents the phase difference between the waves from each arm of the interferometer.
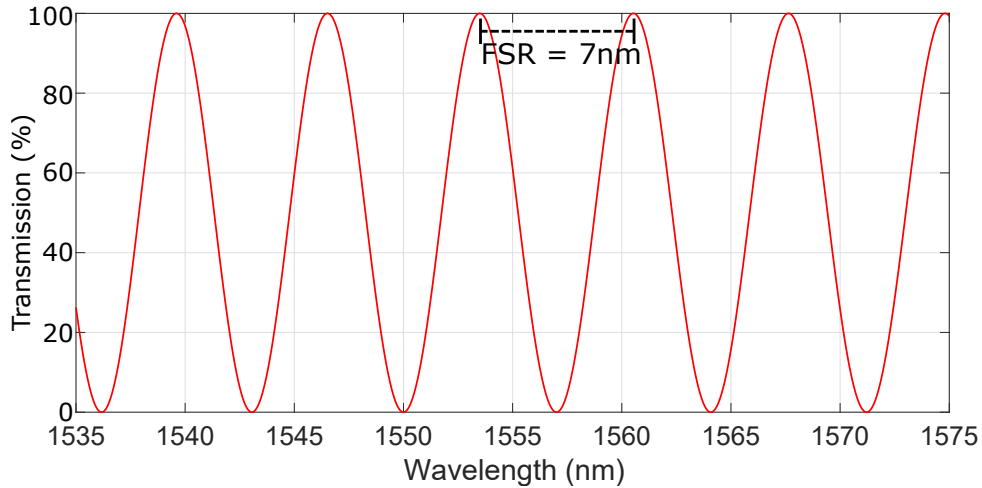


**Figure 2.10:** Simulation of a Mach Zehnder interferometer with $\Delta L = 200$ μm

When the two arms are identical, the transfer function will have maxima when $|\beta_2 L_2 - \beta_1 L_1| = 2m\pi$ with m integer. Similarly the transfer function will have minimum when $|\beta_2 L_2 - \beta_1 L_1| = m\pi$ with m integer. The value of FSR obtained around 1560 nm using a $\Delta L = 200$ μm results to be 7.6 nm.

## 2.5   Non linear optics in SOI

As stated before, the major part of the technology presented in this work is based on SOI technology. One of the main reason for this is that silicon photonics is an ideal platform for

nonlinear applications [66, 67, 68, 69]. This is mainly due to two reasons; the first is the high refractive index contrast between Si and SiO$_2$ (n$_{Si}$ = 3.47, n$_{SiO_2}$ = 1.47, around 1550nm) that allows a strong confinement with high power density in a small region and with low overall power required. The second is that Si as a significant third order nonlinearity (the non-linear coefficient n$_2$ is measured to be 100 times larger than the one found in SiO$_2$ (n$_{2Si}$ $\approx 3 \times 10^{-18}$ m$^2$/W). Due to its centro-symmetric lattice structure, Si does not exhibit native second-order nonlinearities. However, it has been demonstrated that it is possible, inducing strain into the material, to break this symmetry and observe electro-optic effects [70]. When no strain is applied to the material fabricating SOI waveguides it is possible to observe many third order nonlinear effects, including stimulated Raman scattering (SRS) [71, 72, 73]. This effect results in being useful for application in amplification [74, 75, 76, 77] and even lasing [78, 79, 80]. Another main outcome of the SOI third-order nonlinearities is the observed Kerr effect, which finds application in self-phase modulation [81] or cross-phase modulation [82]. Two-photon absorption (TPA) is another major effect that comes from the third order nonlinearity of Si. Its coefficients are calculated in [83] and it has been demonstrated that it can be used for applications like cross-phase modulation and cross-amplitude modulation [83].

### 2.5.1 Four wave mixing

Being a centro-symmetric material, bulk Si will not show any second harmonic generation but, as stated before, Si exhibits a significant Kerr effect and therefore third harmonc generation [41]. One of the main applications of the Kerr effect in SOI waveguide is FWM [43]. During classical FWM, two photons (called pump) interact in the generation of two new photons (called signal and idler), which, can present different frequencies related to the pump frequency [84].

Major applications of FWM are wavelength conversion [42, 43, 38, 39] and all-optical signal processing [85, 86] but, since the total energy of the correlated produced photons should be the same as the energy of the pump photons, FWM can also be used to generate entangled photons [87, 12]. When FWM is performed in a ring resonator and the wavelengths are on resonance with the ring, the effect is strongly enhanced [88]. This is due to the resonant nature

of the device that increase the power density without the need of an increasing input power. This phenomenon and its applications are better described in detail in Chapter 4 together with some novel applications.

### 2.5.2 Optical bistability

Another nonlinear effect to consider when using SOI resonant struture is the thermally induced skewing of the resonance peak for increased optical power, which can give rise to bistable behaviour [89, 90]. The effect is demonstrated in Figure 2.11 where the resonance peak of a drop port of an add drop filter is illustrated.
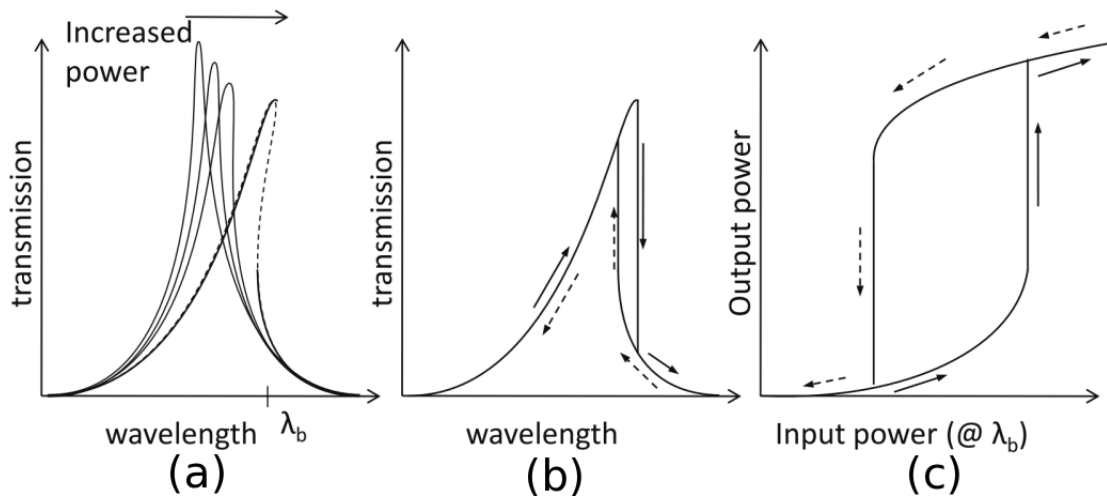


**Figure 2.11:** Nonlinear bistability in ring resonators. (a) skewing of the resonance at higher power levels, (b) hysteresis in a wavelength sweep, (c) hysteresis in optical resonance at a fixed wavelength [55].

For high power in the cavity the resonance peak shows a skewing towards the red side of the spectrum (as shown in Figure 2.11a) and, after a certain power level, the resonance peak goes back to its original resonance wavelength. This results in three possible transmission levels, of which only two are stable solutions. When a tunable laser is used, for this high power, the measurements will therefore be different in the case the spectrum is measured from red to blue or vice versa. Hysteresis in the power transmission will therefore be observed at a wavelength in the bistable region, as shown in Figure 2.11b and Figure 2.11c. Depending on the Q-factor of the ring, the power required to reach this bistable effect could vary. The

higher the Q-factor, the lower is the power required to reach this effect. In order to be able to use this bistability for application in, for example, signal modulation, it is necessary to stabilise the effect. A better description of the phenomenon together with a solution for the bistability stabilisation will be the main topic of Chapter 5.

### 2.5.3  Conclusions

After the description of the main technology used in this dissertation and of the main phenomena that is possible to observe in this field, it is possible to proceed with the detailed description of the work carried out in this research project.

The focus is, at first, on the performance of state of the art SOI photonic integrated circuits. The effect of TE and TM polarised modes in standard ring resonator and Bragg grating structures is presented and two dual polarisation filter geometries with a high rejection ratio are demonstrated, with the aim of solving the filter polarisation mode dependency. The first dual polarisation filter is based on the implementation of plasmonic TM filters in a ring resonator geometry while the second is obtained from the superposition of specifically designed TE and TM Bragg gratings. After this demonstration, one of the devices presented will be used to demonstrate nonlinear FWM experiments including dual polarisation pump light rejection. Stabilization of silicon micro-resonators using a micro-processor based feedback control loop is then presented introducing a silicon $\pi$-phase shifted grating with a cavity Q-factor of 40k, demonstrated to operate over an ambient temperature detuning range of $40\,^{o}$C and injection wavelength range of $1.5\,$nm, nearly 3 orders of magnitude greater than the resonant cavity linewidth. The description of the process of direct laser lithography will then take the last part of this dissertation including the presentation of the fabricated $SU-8$ on $SiO_2$ PICs. Waveguides, bends, MZI and RR have been characterised and all the results are presented.

# Chapter 3

# Dual polarisation integrated photonic filters

## 3.1 Introduction

Photonic filters are one of the key elements in optical communication systems [91] and have attracted significant interest due to their potential for a wide range of applications, including noise suppression [92], signal quality improvement, on-chip networking [93], spectroscopy [94] and pump filtering for non-linear optics [95]. Most of these do not require high performance in terms of extinction. However, in some applications like non-linear optics, this is one of the most demanding features [50]. All the devices presented in Chapter 3, Chapter 4 and Chapter 5 are fabricated by our collaborators in the University of Glasgow, using SOI technology.

When the light propagates in a planar SOI waveguide the orientation of either electric and magnetic field can be TE when the electric field is orthogonal to the planar surface or TM when the electric field is parallel to the planar surface. Historically, for most demonstration of switching network applications, the photonic integrated circuits are optimised for TE mode propagation. This is due to both the material design of the SOI wafer (favoring low TE losses) and to the carrier recombination selection of the semiconductor edge emitting lasers used to couple to this technology as a signal generator.

As stated in the introductive chapter, SOI is one of the most mature and well developed

photonic integration platforms [4, 96, 6, 7, 8], benefiting from the availability of CMOS fabrication technology, where it is possible to use electronics fabrication facilities to make photonic circuitry[9]. The large refractive index contrast between the two materials allows a strong confinement of the optical mode to waveguide cross-sections with sub-micron dimensions, making SOI photonics an interesting technology for application in telecommunications [10, 11, 3], biosensing [12] and quantum optics [13, 14, 15].

On-chip silicon filters optimised for TE polarisation have been demonstrated with high quality factors [44] and extinction values $\approx$ 45-50 dB [45, 46, 47, 48, 49]. High extinction values ($\approx$ 100 dB) have been reached in a few cases, using a grating filter coupled with two ring resonators [50] or using two 5th order CROW (coupled resonator optical waveguide) filters on separate chips [51]. All of these results are optimised for TE rejection and do not take in account the light in the TM polarisation. Significant scattering between the TE and TM modes, has been shown to occur in SOI waveguides, limiting polarisation extinction to $\approx$ 20 dB [52] due to the TE sensitivity to sidewall roughness in a typical SOI waveguide (220nm $\times$ 500nm). This effect leads to significant amount of light passing through the TE mode filter.

The focus of this chapter is on the performance of state-of-the-art PICs. Two dual polarisation filter geometries with a high rejection ratio are demonstrated here. Both structures aim to solve the filter polarisation mode dependency. The effect of TE and TM polarised modes in standard ring resonator and Bragg grating structures is presented. The first dual polarisation filter is based on the implementation of TM filters in a ring resonator geometry while the second is obtained from the superposition of specifically designed TE and TM Bragg gratings. Some of the devices developed here will be used in the system presented in Chapter 5 where one of the many possible applications for the photonic integrated filters is presented.

## 3.2   Device fabrication and technology

Two common filter geometries based on ring resonator and Bragg grating devices are presented in this section. The properties and the theory behind these devices are detailed in Section 2.2 and Section 2.3. As a reminder, it is possible to say that a ring resonator is an optical

waveguide that is looped back on itself assuming the shape of a ring or of a racetrack. The main difference between ring resonator and Bragg grating is that the ring presents periodic resonances while the Bragg grating is a single resonance filter device.

In a ring resonator these periodic resonances occur when the optical path length of the resonator L is exactly a whole number of wavelengths $\lambda_{\text{res}}$ as shown in equation 2.22:

$$\lambda_{\text{res}} = \frac{n_{\text{eff}}L}{m} \ . \tag{3.1}$$

with m integer and $n_{\text{eff}}$ the waveguide's effective index. An optical Bragg grating is instead a photonic filter obtained periodically varying the waveguide's sidewalls creating a periodic variation of the refractive index so that a large reflectivity may be reached in some wavelength range (bandwidth) around a certain wavelength which fulfills the Bragg condition:

$$\lambda_{\text{B}} = 2n_{\text{eff}}\Lambda \ . \tag{3.2}$$

where $\lambda_B$ is the Bragg wavelength, $\Lambda$ is the grating period and $n_{\text{eff}}$ the waveguide's effective index. For a full description of these devices the reader is referred to Chapter 1.

### 3.2.1 Fabrication details

The fabrication of the SOI waveguides investigated in this chapter was carried out in the James Watt Nanofabrication Centre at the University of Glasgow. The fabricated waveguides consist of a silicon core with height of 220 nm and width of 500 nm. These dimensions are standard in the creation of single mode TE propagation SOI waveguides. The reason for this is better explained from the simulation of first and second order TE mode propagation in a waveguide cross section shown in Figure 3.1 and Figure 3.2 respectively. For more information on the algorithm used in this simulations the reader is referred to section 6.5.1.
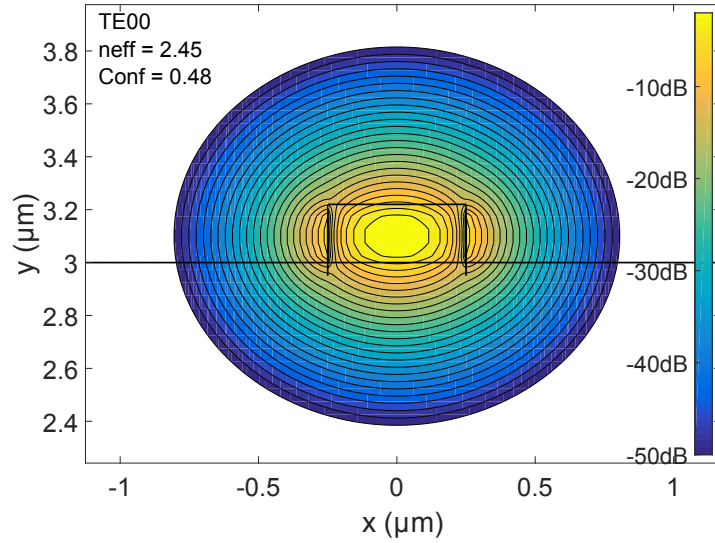
**Figure 3.1:** Mode propagation simulation for SOI waveguides with 220 nm height and 500 nm width for $TE_{00}$ mode. The junction point between the two modes is an artifact of the simulation software.
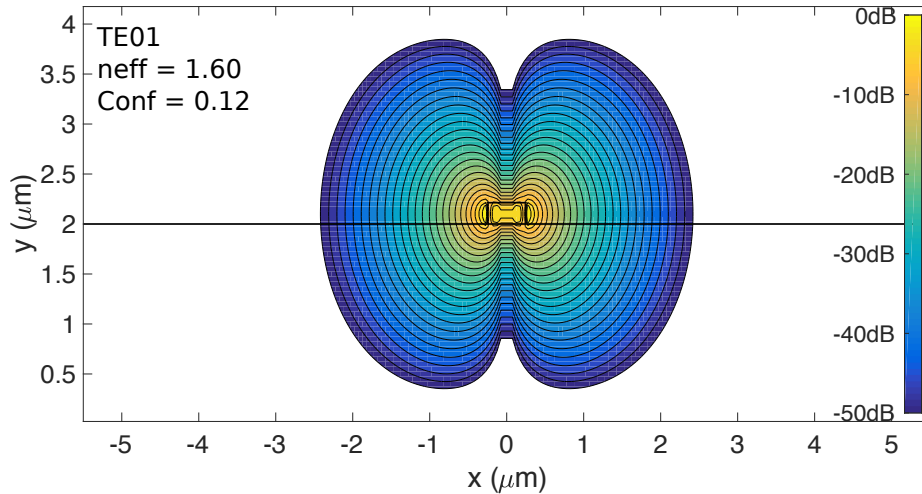


**Figure 3.2:** Mode propagation simulation for SOI waveguides with 220 nm height and 500 nm width for $TE_{01}$ mode. The junction point between the two modes is an artifact of the simulation software.

The values of effective refractive index and confinement factor shown in Figure 3.1 and Figure 3.2 are obtained from the simulations shown in Figure 3.3 a and Figure 3.3 b respectively for a 500 nm × 220 nm waveguide.

All the values obtained from the simulations for the $n_{eff}$ and the confinement factor can be plotted in function of the waveguide width. Both quantities establish the maximum value for the waveguide width necessary to obtain single mode propagation (limit expressed as the

33
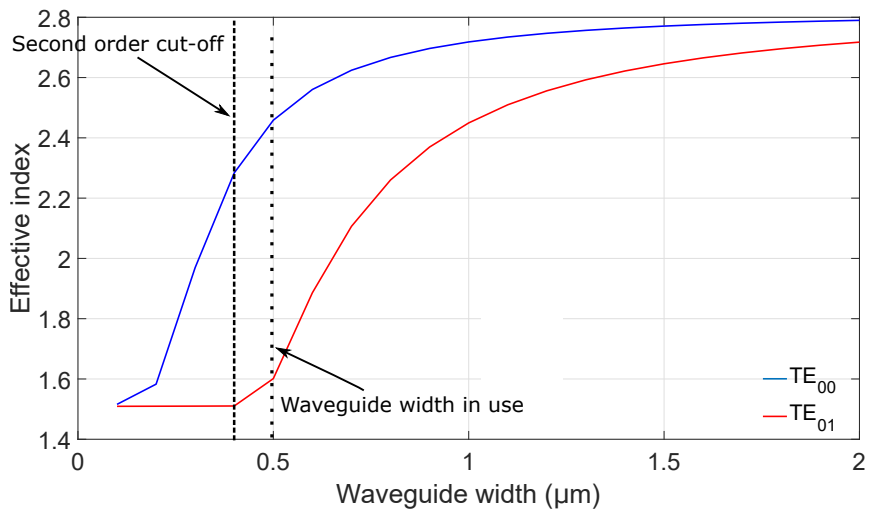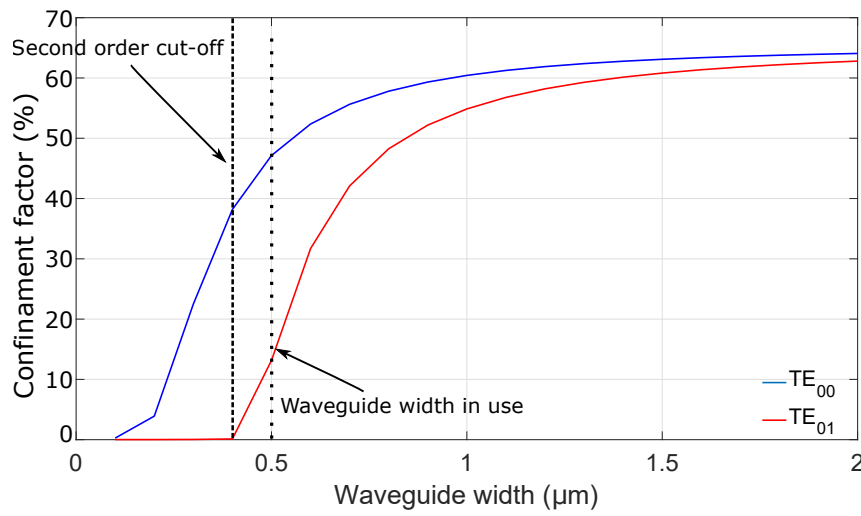
**Figure 3.3:** Effective refractive index (a) and Confinement factor (b) variation in function of waveguide width for a fixed height of 220 nm. The cut off point is shown to be around 450 nm.

"cut-off region" in both in Figure 3.3 a and Figure 3.3 b. In these simulations it is possible to see how, even though the width in use crosses the cut off point, the confinement factor which is considered as the ratio between the mode confined in the waveguide and the total field injected, for the width in use is only 12% a very low value which empirically ensure a single-mode propagation on a SOI waveguide fabricated using these dimensions.

The device patterning was defined using electron beam lithography with Hydrogen Silsequi-oxen (HSQ) as the resist layer, which was transferred to the silicon core by using Reactive Ion Etching. In order to increase the coupling efficiency inverse tapers and polymer waveguides were used to couple the light in and out of the chip. The polymer waveguides were fabricated in $SU - 8$, with dimensions of 5 µm in width and 3.5 µm in height. The silicon waveguides were coated with a 1 µm thick Plasma Enhanced Chemical Vapour Deposition (PECVD) $SiO_2$ as a buffer layer. All the gratings were defined as a sinusoidal perturbation on the waveguide sidewalls [97]. Examples of the layout and dimensions of the devices used in this work are shown in the Scanning Electron Microscopy (SEM) images of Figure 3.4 and Figure 3.5.
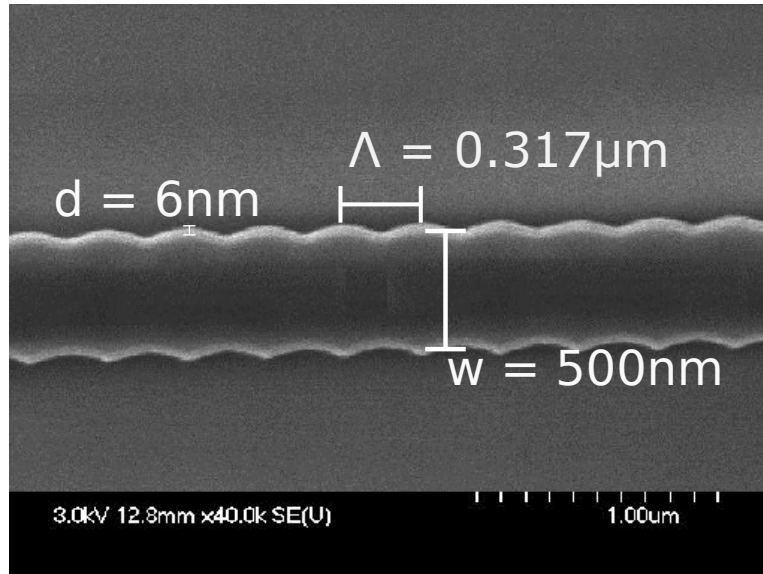


**Figure 3.4:** SEM images of sidewall gratings with coupling coefficient $\kappa = 130$ cm$^{-1}$.
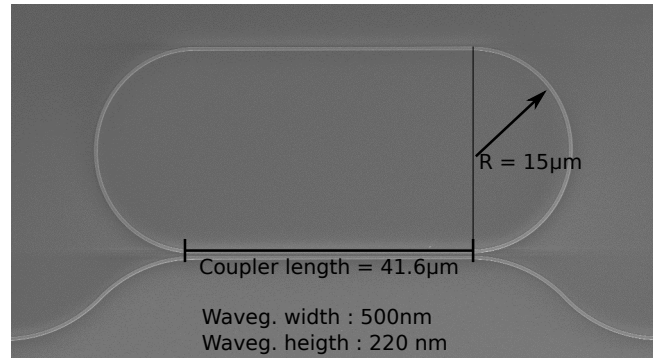
**Figure 3.5:** SEM image of an example of the single all pass ring resonator used in this work.

## 3.3 Measurement setup

The transmission spectra of the filters were measured by coupling light, using a Polarisation Maintaining (PM) fibre, from a tunable laser through a polarisation filter with an extinction ratio of 20 dB aligned with the TE mode to a PM lensed fibre and into the input polymer waveguide. The output light was coupled into a second PM lensed fibre and the output signal was sent to an Optical Spectrum Analyser (OSA). No polarisation selective off-chip filters were applied after transmission through the chip. The polarisation extinction before the chip was measured at 20 dB. A schematic of the experimental setup is shown in Figure 3.6.
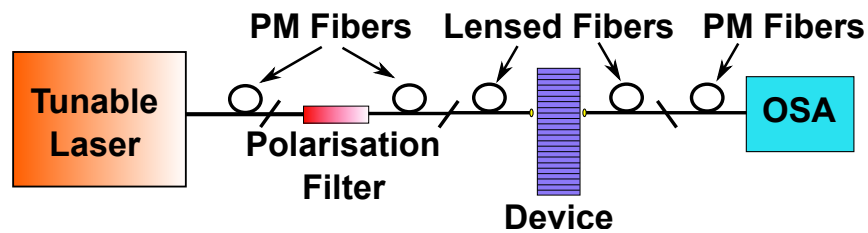


**Figure 3.6:** Experimental setup used for transmission measurements of SOI ring resonators and Bragg gratings.

Loss measurements for SOI straight waveguides co-fabricated with the filters were carried out using the experimental setup of Figure 3.6. An optical waveguide with polished endfaces (facets) is similar in structure to the cavity of a laser. Light propagates along the waveguide and may be reflected at either facet by an amount determined by the refractive index of the waveguide material and the external media (usually air). Therefore the waveguide structure may be regarded as a resonant cavity, with the waves undergoing multiple reflections as they

36

pass along the waveguide and back. Such a cavity is called a Fabry Perot cavity [98]. The optical intensity transmitted through such a cavity, $I_t$, is related to the incident light intensity, $I_0$, by the well-known equation [99]:

$$\frac{I_t}{I_0} = \frac{(1-R)^2 e^{-\alpha L}}{(1-Re^{\alpha L})^2 + 4Re^{\alpha L}\sin^2(\phi/2)} \ . \tag{3.3}$$

where R is the facet reflectivity, L is the waveguide length, $\alpha$ is the loss coefficient, and $\phi$ is the phase difference between successive waves in the cavity. The equation has a maximum value when $\phi = 0$ (or multiples of $2\pi$), and a minimum value when $\phi = \pi$; Therefore we can evaluate the ratio of the maximum intensity to minimum intensity as:

$$\xi = \frac{I_{max}}{I_{min}} = \frac{(1+Re^{-\alpha L})^2}{(1-Re^{-\alpha L})^2} \ . \tag{3.4}$$

we can rearrange this equation as:

$$\alpha = -\frac{1}{L}\ln\left(\frac{1}{R}\frac{\sqrt{\xi}-1}{\sqrt{\xi}+1}\right) \ . \tag{3.5}$$

therefore if we know the reflectivity R, and if we can measure the ratio of the maximum intensity to minimum intensity, $\xi$, the loss coefficient can be evaluated [99].

The coupling efficiency does not affect the calculation of loss coefficient, although it is implicit that the coupling efficiency remains constant. This method can be particularly useful for measuring low losses, under certain conditions. It is in fact demonstrated to be accurate if the reflectivity is known to better than 0.01, and is relatively high, of the order of 0.6. In our case the reflectivity is measured to be:

$$R = \frac{(1-n_{eff})^2}{(1+n_{eff})^2} = \frac{(1-2.42)^2}{(1+2.42)^2} = 0.172 \ . \tag{3.6}$$

using the Fast Fourier Transform (FFT) method [98], the average propagation losses was measured for both TE and TM modes resulting in a value of 0.5 dBcm$^{-1}$ for the TE propagation and 5 dBcm$^{-1}$ for the TM propagation. Fiber to polymer inverse taper losses were measured at 2.5 dB per facet. The designs, measurements and data analysis on the two dual polarisation

high extinction filters used are presented in the next section.

## 3.4  Dual polarisation effects in SOI filters

### 3.4.1  Ring resonators

In this work two different ring resonator designs are used to make high extinction filters: a
CROW geometry (in which the rings are coupled one with each other) and a cascade (in which
the rings are coupled by using straight waveguides in the coupler section). The two geometries
are described in Figure 3.7. In both CROW and cascade geometries, the number of resonators
can be increased in order to increase the filter rejection but, given the sensitivity of the OSA
detection system and the substrate light noise, later described in Chapter 5, the number of
the rings used in this work has been limited to three.
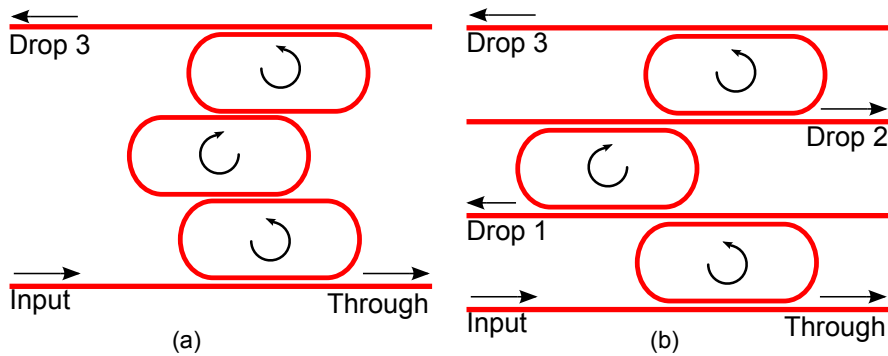


**Figure 3.7:** Comparison between the third order CROW geometry (a) and the Cascade geometry (b).

Two simulations that compare the output of each filter for TE transmission are presented
in Figure 3.8 and Figure 3.9. The simulations are obtained using a transfer matrix method
model of a ring resonator [100, 101] and considers resonators with a coupler length of 42 µm
and bend radius of 15 µm. All couplers are designed to produce a power coupling coefficient
of 0.1. Figure 3.9 shows how the cascade, being a set of first order filters, presents the notch
corresponding to the transmission of the next ring at each output. e.g. the drop signal after
two rings (Drop 2) presents a notch relative to the transmission of the third ring. This allows
tuning of the transmission of the third ring with the drop peak of the second.
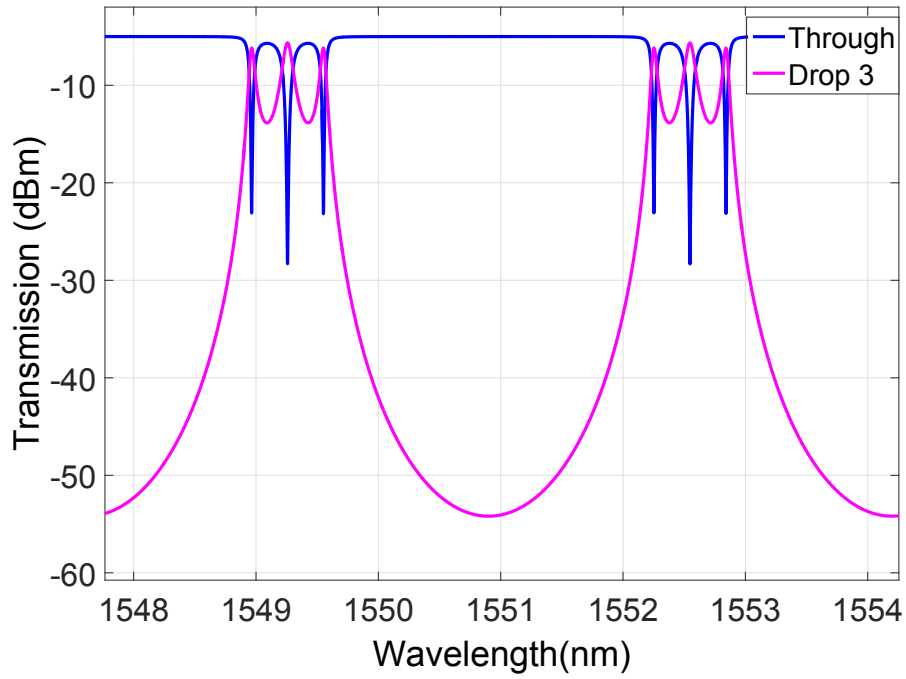
**Figure 3.8:** Simulated spectra of CROW drop outputs for the TE mode.
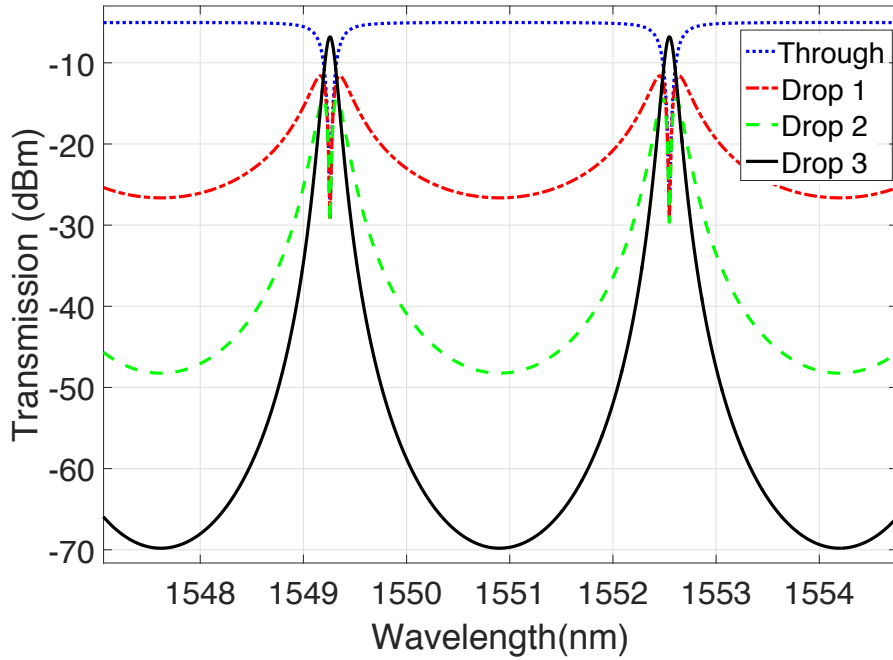


**Figure 3.9:** Simulated spectra of cascade drop outputs for the TE mode.

The CROW is effectively a third order filter, whereas the cascade is a series of three first order filters. This produces a bandwidth of 700 pm in the CROW case, and 100 pm for the

cascade, and a maximum extinction ratio, calculated to be 50 dB for the CROW and 65 dB for the cascade, a result 15 dB higher than the CROW. It is therefore clear how, using a cascade device rather than a CROW, it is possible to obtain, for the same number of rings, a narrower band with a higher rejection filters. Experimental results obtained using a single ring resonator shown in Figure 3.10 demonstrate the transmission spectra obtained injecting TE (blue and red curves) and TM (green and purple curves) respectively.

From the results in in Figure 3.10 it is possible to see that both TE and TM have a comparable power output. As demonstrated in [52], the significant scattering between TE and TM modes occurring in SOI waveguides, limits the polarisation extinction to $\approx 20$ dB. If then TE light is injected into the device, a TM mode will propagates as well with a power level which will be 20 dB lower than the TE one. A significant amount of TM light is therefore predicted in the TE rejection band. This light needs to be filtered in order to be able to use this device for further applications (e.g. FWM).
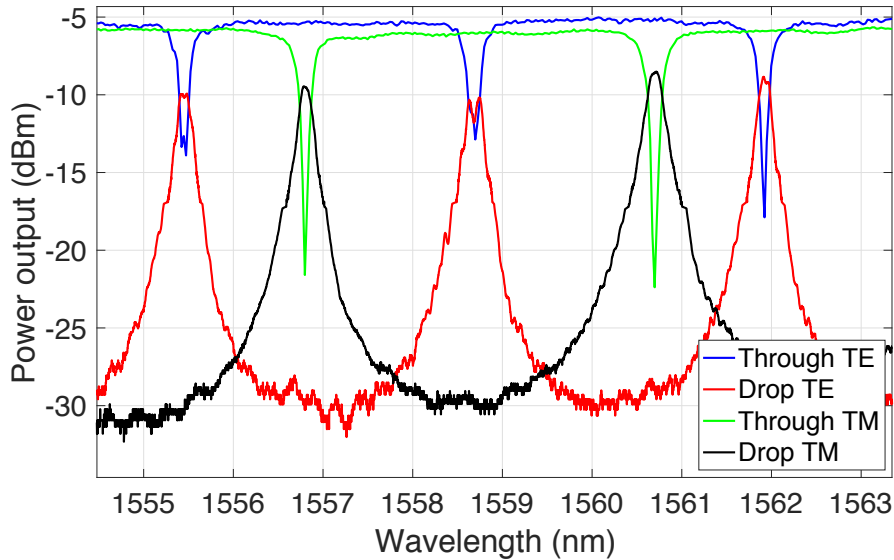


**Figure 3.10:** Experimental results obtained using a single ring resonator for different polarisation injection. TE (blue and red curves) and TM (green and purple curves).

Since the maximum extinction ratio obtained using this device is $\approx 20$ dB, it is not possible to see a TM propagating mode when TE is injected and vice versa. The TM propagation, when a TE mode is injected, is 20 dB lower than the TE itself, and it is therefore just at the bottom of the drop port noise floor. To be able to observe this effect it is necessary to use a

higher extinction ring (for example a 3 ring resonator cascade) but, in that case, the presence of the tuning mechanism necessary to align the resonance wavelengths would itself absorb the TM (as will be shown in the next section). The polarisation behaviour shown with the simulations and endorsed with the experimental results on the single rings it is confirmed by previous studies [102]. Even though these results are obtained using a CROW device with lower Q factor they can be used to confirm that the TM polarised mode can be disruptive for experiments where a TE only transmission is necessary.

The 20 dB lower TM transmission when TE mode is injected is simulated in Figure 3.11 and Figure 3.12 where the transmission of ideal TE and TM (20 dB lower) guided mode is shown. As it is possible to see due to the resonance wavelenght difference, injecting a TM level 20  dB lower than the TE the simulated transmission for either ideal TE or TM mode propagation for both cascade and CROW devices.
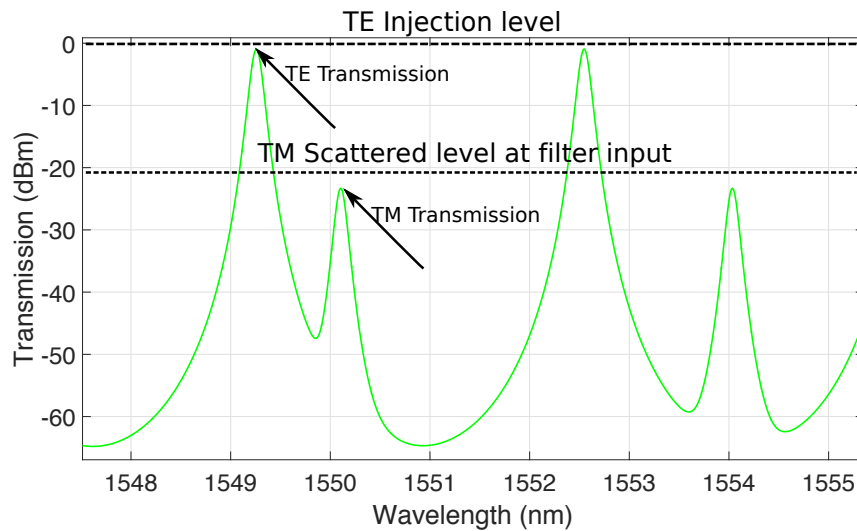


**Figure 3.11:** Simulated spectrum of TE + TM injection for a three ring cascade device.

41
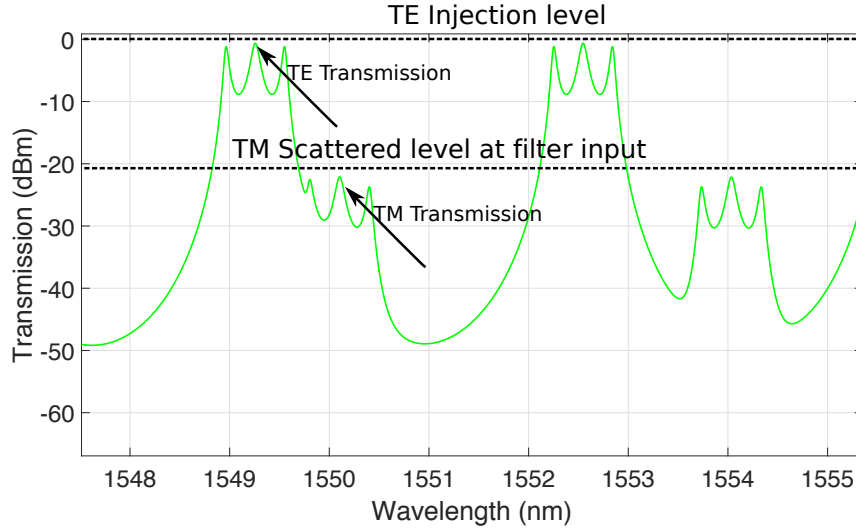
**Figure 3.12:** Simulated spectrum of TE + TM injection for a three ring CROW device.

### 3.4.2 Metal TM mode filters

As detailed above, in filters designed for TE applications, significant levels of TM polarised light can be transmitted. It is therefore necessary to filter the TM in addition to the TE. In Figure 3.13 a cross section of a TE and a TM mode in a SOI waveguide is shown. The TE mode (Figure 3.13(a)) is concentrated in the high index region (e.g. silicon core) while the TM mode, shown in Figure 3.13(b), shows a higher fraction of the mode energy propagating in the lower index region (e.g. silica).
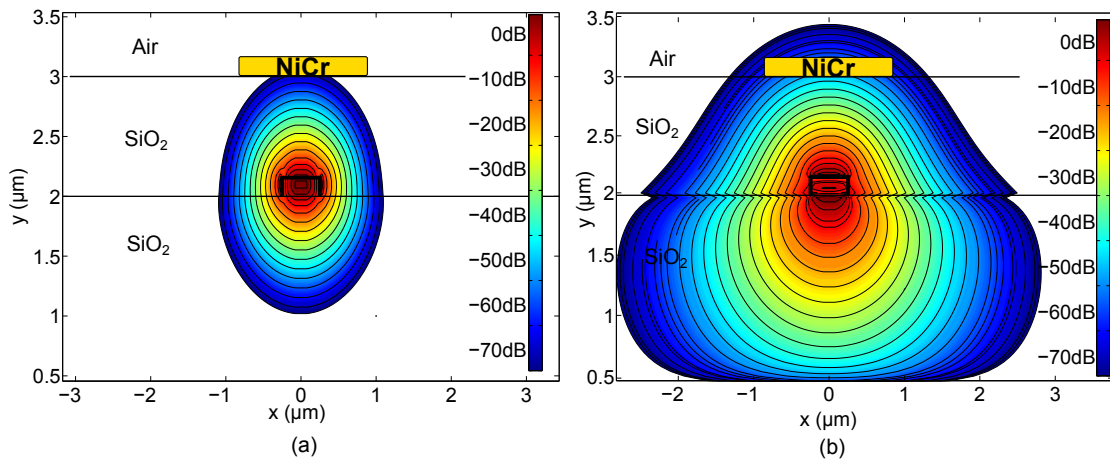


**Figure 3.13:** Mode cross section for TE (left) and TM (right) polarised field in a $220 \times 500$ nm silica waveguide.

By placing an additional metal layer on top of the device, as demonstrated in previous studies [103], it is possible to filter the TM without affecting the TE mode propagation. This is because the large TM field overlap with the metal enhances the TM losses but not the more confined TE. Based on this principle, a dual polarisation filter can be implemented by fabricating the metal layer on a TE filter design.

A set of straight waveguides were fabricated using this metal cladding and transmission measurements were carried out. The TE and TM propagation loss was obtained using a cutback method and the results demonstrate that the TE mode propagation shows a loss of around 0.5 dBcm$^{-1}$ in both cases with and without metal coating. In the case of TM mode propagation, the loss (shown in Figure 3.14) is found to be around 60 dBcm$^{-1}$ at 1550 nm, compared to the 5 dBcm$^{-1}$ for waveguides fabricated without metal. This solution is particular straightforward to implement in the tunable filter design presented here.
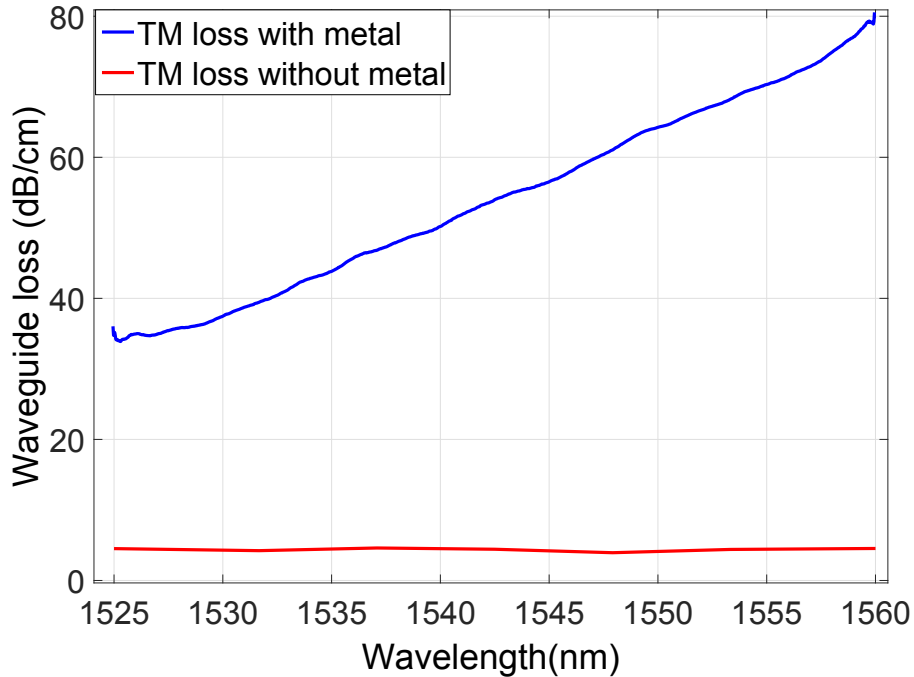


**Figure 3.14:** Measured waveguide loss as a function of the input wavelength for a TM injection in a single waveguide with NiCr cross sectional area of 50 × 900 nm.

All the ring resonators used in this work have NiCr heating elements fabricated above the ring waveguide cross section. This is in order to obtain the necessary resonance wavelength

tunability, as shown in [104]. This heating element then provides not only the tunability function but also the necessary TM absorption losses. In Figure 3.15(a) and Figure 3.15(b) a comparison of the effect of TE and TM propagation in a three rings cascade and CROW device using the solution described is shown.
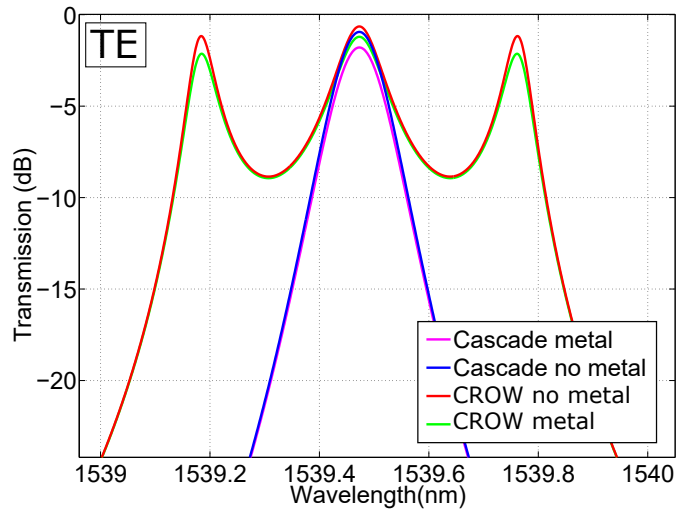


(a)
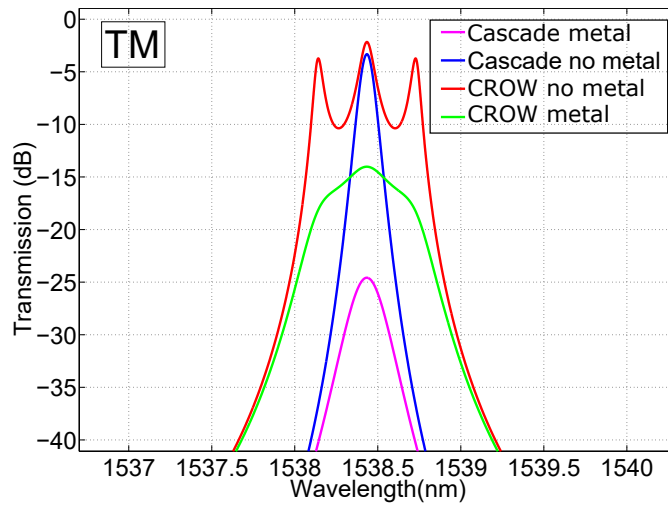


(b)

**Figure 3.15:** Comparison between the simulations of linear transmission of CROW and cascade output for (a) TE and (b) TM propagation using the metal layer

The simulations are obtained using a transfer matrix method model of a ring resonator [100, 101] and consider resonators with a coupler length of 42 μm and bend radius of 15 μm.

The metal loss is introduced by changing the value for the propagation loss with what obtained from Figure 3.14. The metal cladding here presented has been implemented in all the fabricated devices where the presence of resonant structure will enhance this effect. From Figure 3.15(a) it appears that in both geometries the presence of the metal doesn't affect the field propagation significantly, confirming the results obtained for the straight waveguides. In Figure 3.15(b) instead, the difference in loss between the two geometries is reduced by only 2 dB for devices without a metal layer while, once introduced, the metal layer produces a significant loss in the propagation in both cases. However, the loss produced is 10 dB higher for a cascade geometry than for the CROW filter. These simulations show then the possibility of fabricating a polarisation insensitive filter with a cascade ring resonator geometry with narrow pass band and high rejection over 62 dB .

The last simulation, in Figure 3.16, shows a cascade of 5 ring resonators. The reason for this is to show that, as described before, the limitations of the results presented here come only from consideration regarding the measurement system. Using a higher number of rings it would be possible to reach the value of extinction required for the applications described in the introduction.
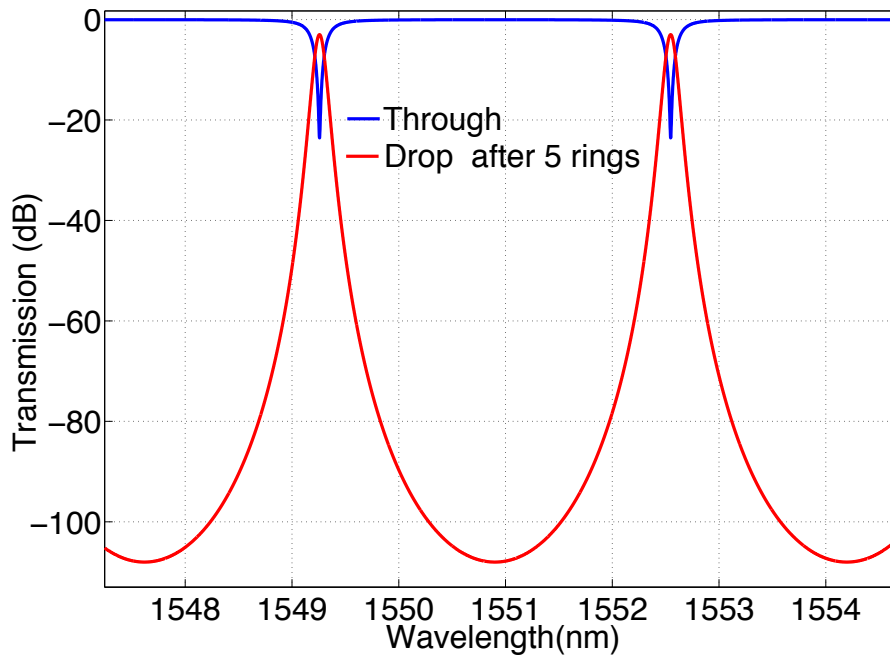


**Figure 3.16:** Simulation of a 5 ring Cascade geometry. In this case it is possible to reach extinction values over 100 dB .

The results obtained using this technology are described in the following section.

### 3.4.3 Ring resonator filter results

Figure 3.17 shows the measured output after three stages of the 3 ring cascade device for TE transmission, comparing this result with the simulation first shown in Figure 3.9. Injecting TE polarised light, with a TM component at -20 dB , the device filters both polarisation components with only 1.8 dB of insertion loss on the TE mode. The results present an excellent match with the simulation of a 3 ring cascade with the same parameters as the one tested.

In Figure 3.19 a measurement of the transmission spectrum at the Drop 3 port is shown for TM injection. Changing the injection light to a TM polarisation, the TE polarised light component is now injected at -20 dB (e.g. the inverse case of Figure 3.17).

In this measurement the TM propagation shows an excess loss due to the metal filter of 50 dB. Therefore, in a TE injection measurement (Figure 3.17 and Figure 3.18), where the TM polarised field was injected with -20 dB with respect to the TE, the TM component is filtered to below the noise floor of the measurement.
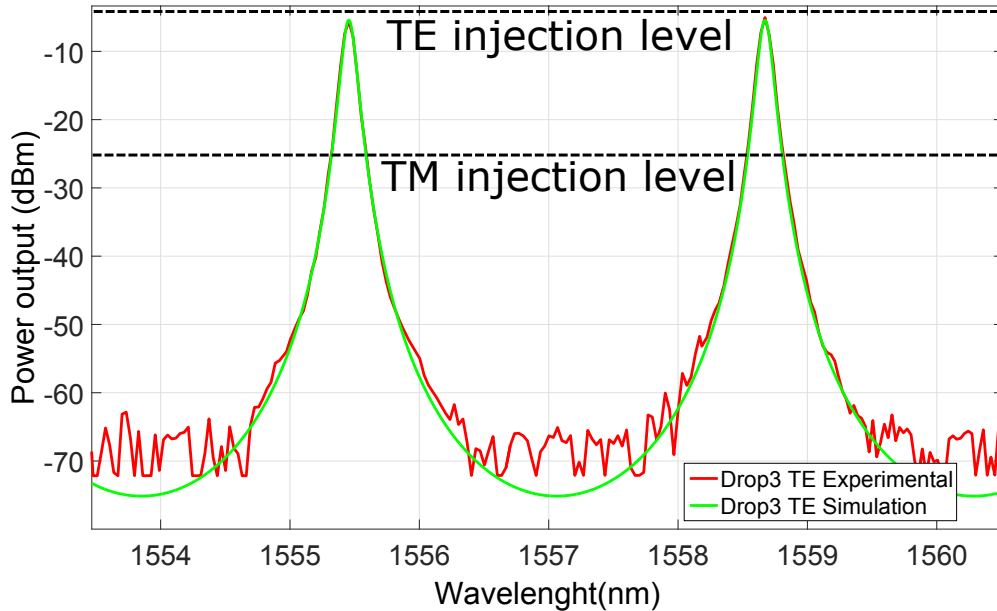


**Figure 3.17:** Drop 3 port transmission measurements of a cascade device for TE mode.
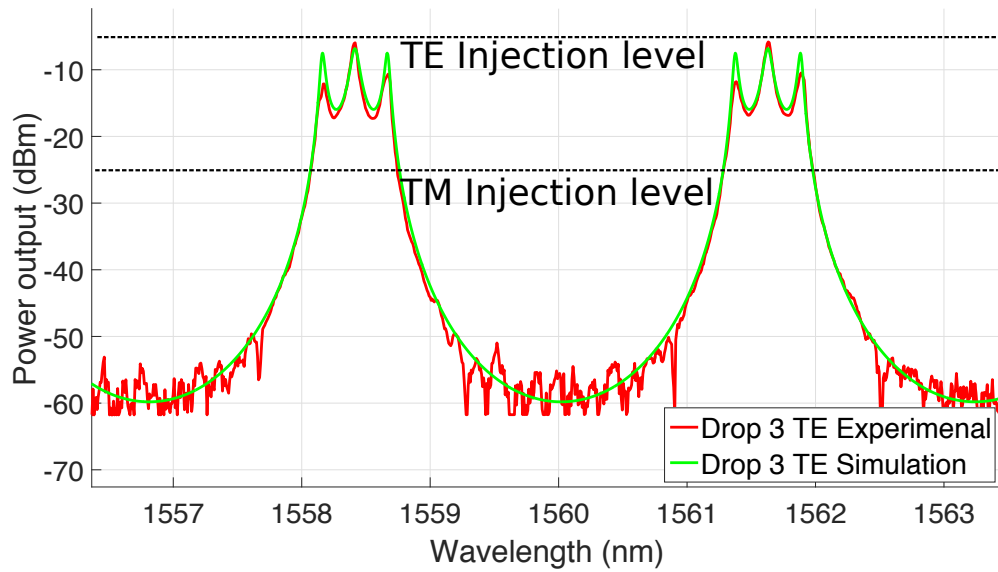
**Figure 3.18:** Drop 3 port transmission measurements of a CROW device for TE mode.

The low loss of the TE component is shown in Figure 3.19 where a strong TE signal at -27 dBm is measured, corresponding to the injected power minus the propagation loss.
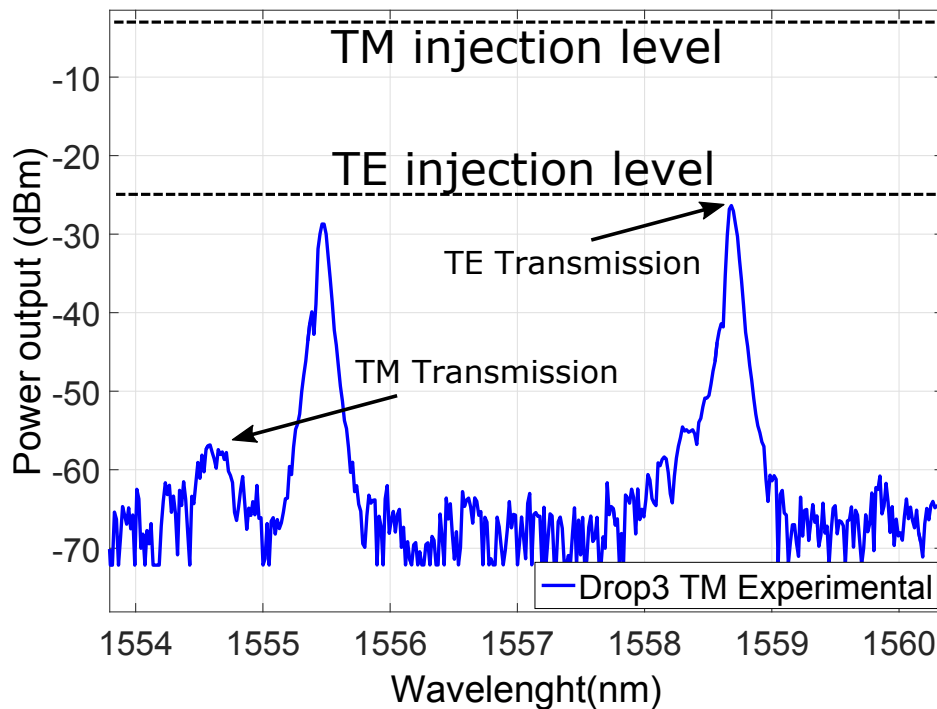


**Figure 3.19:** Drop 3 port transmission measurements of a cascade device for TM mode.

### 3.4.4 Bragg Gratings

A second common filter geometry is the Bragg grating, which presents a single, generally wideband spectral rejection feature. Integrated Bragg filters are already in use for telecommunication systems [105], signal processing [106, 107], hybrid III-V on silicon lasers [108] and quantum photonics [109, 110]. Sidewall gratings provide high extinction ratio and accurate control over the grating strength, as well as a simple fabrication processing since both waveguide and grating are defined in the same etching run. Unfortunately in this case the TM polarisation does not interact strongly with the waveguide sidewalls and is therefore transmitted through the device with marginal loss. This limits the use of these gratings in applications that require polarisation multiplexing and selectivity. From Figure 2.8 it was possible to see how the length of a grating controls the maximum extinction ratio that is possible to achieve using these devices.

All the Bragg grating simulations shown in this work were performed using Lumerical MODE solution with 2.5 VarFDTD [59]. As the Bragg grating theory confirms, increasing the length of the grating it is possible to increase the extinction ratio, defined in this case as the ratio between the out of band optical power and the minimum power of the filter response. In this case where the grating $\kappa$ is fixed to 130 cm$^{-1}$ the highest extinction is 75 dB with a transmission bandwidth at -3 dB of 3 nm . TM simulations are not shown because, as mentioned above, TM polarisation does not interact with the sidewalls and is therefore transmitted through the device with marginal loss (an extinction ratio < 0.5 dB is introduced in the stop-band for TM propagation). Measured transmission spectra for the device matching the simulation parameters are shown in Figure 3.20. Measurements confirm that increasing the length of the grating leads to an increase of the extinction ratio, calculated in this case considering the average in band output level.
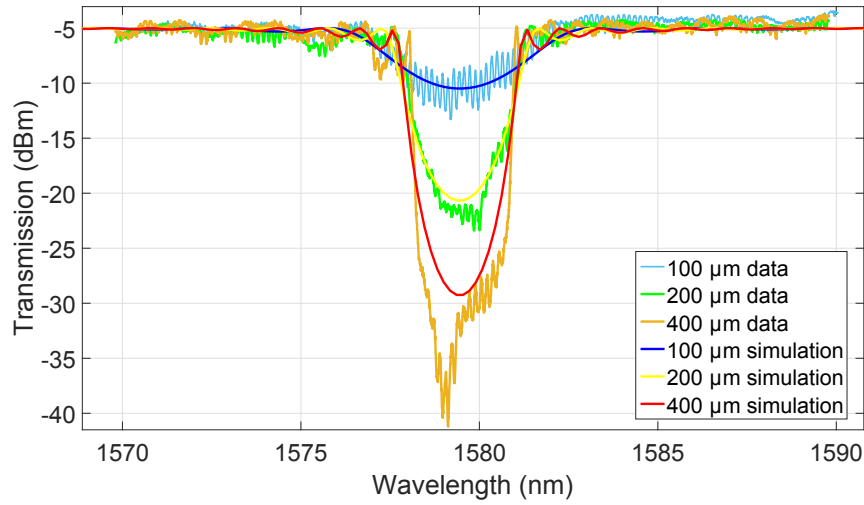
**Figure 3.20:** The experimental transmission spectra of κ of 130 cm$^{-1}$ perturbation gratings with variable length.

However, this value only increases up to a saturation point of around 25 - 30 dB. This level is correlated with TM propagation in the TE stopband limiting the extinction ratio of the device. This statement is made more clear from the results in Figure 3.21 were grating devices with grating length up to 1600 µm are measured.
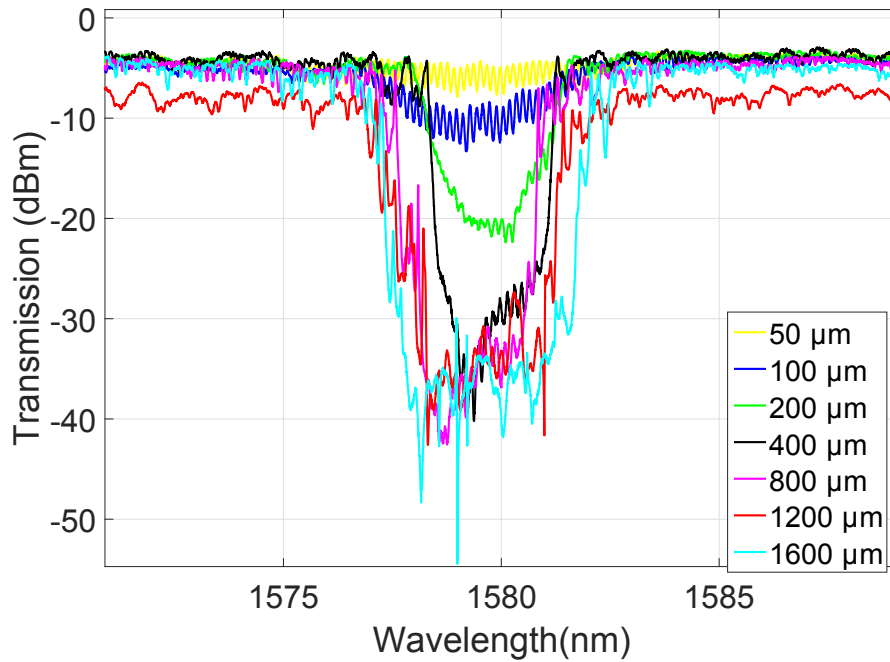


**Figure 3.21:** The experimental transmission spectra of κ of 130 cm$^{-1}$ perturbation gratings with variable length.

In order to summarise all the results obtained for these grating devices and make some conclusions, Figure 3.22 shows the extinction ratio of the filters as a function of the κL product for a variety of devices with length varying between 50 μm and 1600 μm, and with κ of 130 cm$^{-1}$, 180 cm$^{-1}$, 560 cm$^{-1}$ and 800 cm$^{-1}$.
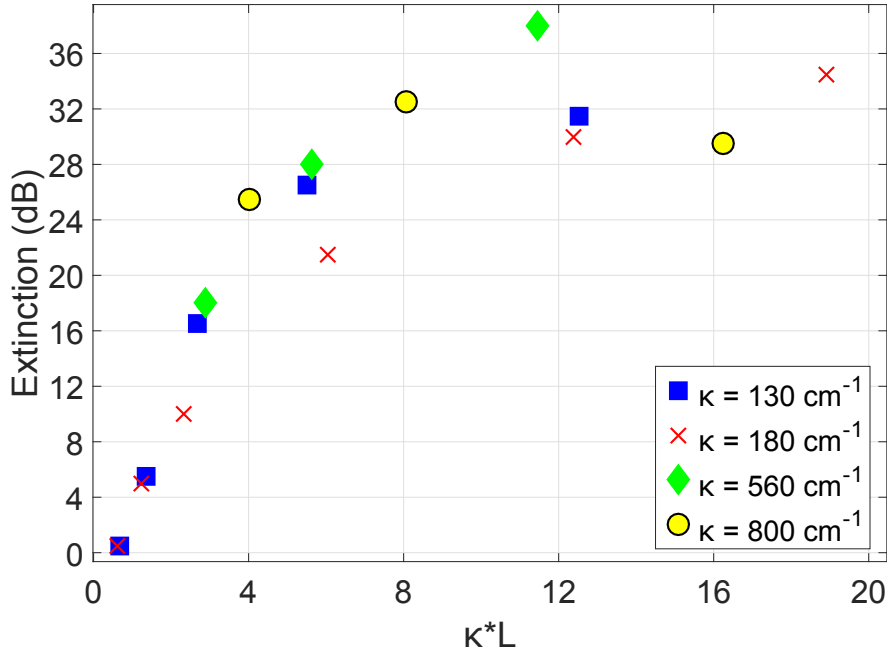


**Figure 3.22:** Filter extinction ratio against the κL product for the side-wall grating devices with different grating strength and length for a waveguide width = 500 nm .

The measurements show a rapid increase of the extinction ratio with κL until the extinction ratio saturates at around 32 dB. This level represents the maximum extinction of the TM light injection for this filters. The next section will give the details of the two proposed solutions for dual polarisation filtering for both, ring resonator and Bragg grating type devices.

### 3.4.5  TM filtered waveguides Bragg grating solution

As stated in the previous section adding a metal layer on top of the waveguide will enhance the TM losses without affecting significantly the TE propagation. Adding this metal layer, as stated in Figure 3.14, an extra 60 dB cm$^{-1}$ loss is introduced at 1550 nm for TM propagation while only 5 dBcm$^{-1}$ are affecting the TE propagation at the same wavelength. Even though the use of a TM filtered waveguides, in the case of Bragg gratings, will not benefit from the

resonance enhancement, experimental results demonstrate that, even for this single stop band filter the use of a metal over cladding improves the performance of the filter of at least 15 dB.
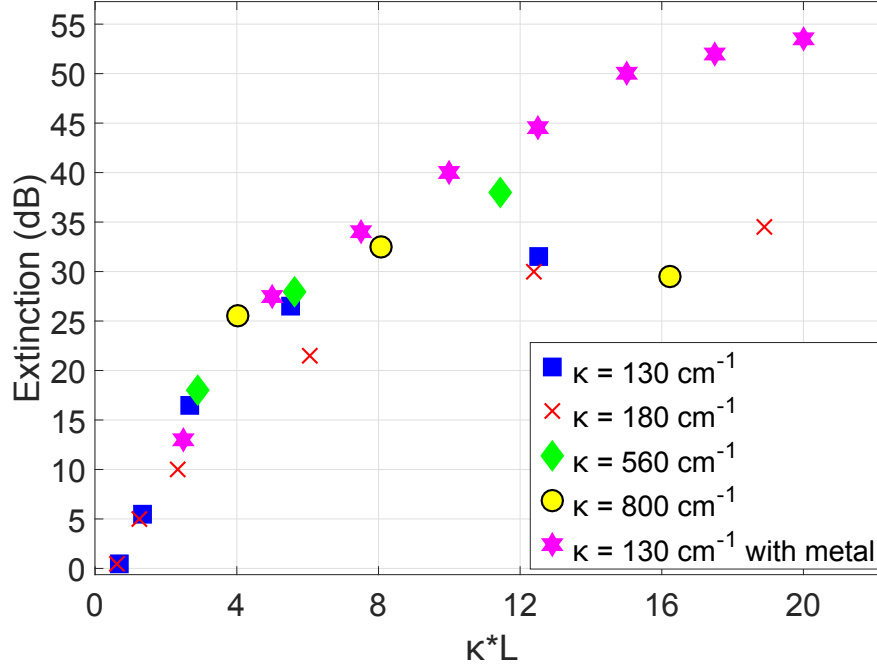


**Figure 3.23:** Results of Figure 3.22 compared to a grating with additional metal layer.

The results in Figure 3.23 show a comparison between the results of Figure 3.22 and those obtained using the same device geometry with the addition of a top metal layer. This solution reduces the TM polarised light propagated through the grating and therefore increases the maximum extinction value. The saturation extinction ratio level is increased to around 55 dB
.

## 3.5 Dual Bragg gratings devices

Comparing these last results shown in Figure 3.23 with those obtained in the previous section using the three ring resonators cascade it is possible to say that the ring performance are still not matched and therefore a stronger TM filter is required. The reason to fabricate a Bragg grating filter device with similar performance with respect to the ring device is because it could be used for applications where the use of a ring resonator is impossible. For example when it is necessary to fabricate a spectral filter resctricted to a single stopband than the use

of a ring device, with its characteristic periodical resonances, is not recommended while a grating would be more appropriate for this kind of application.

It has been demonstrated in previous work that features in the top surface of the waveguide show greater overlap with the TM mode and hence greater TM coupling [59]. Co-fabricating this top grating design together with the devices already in use it is therefore possible to increase the gratings TE on TM ratio matching the value obtained using the ring resonators. The top grating design consisted of etched holes in a silicon waveguide with various radii and lengths as shown in Figure 3.24.
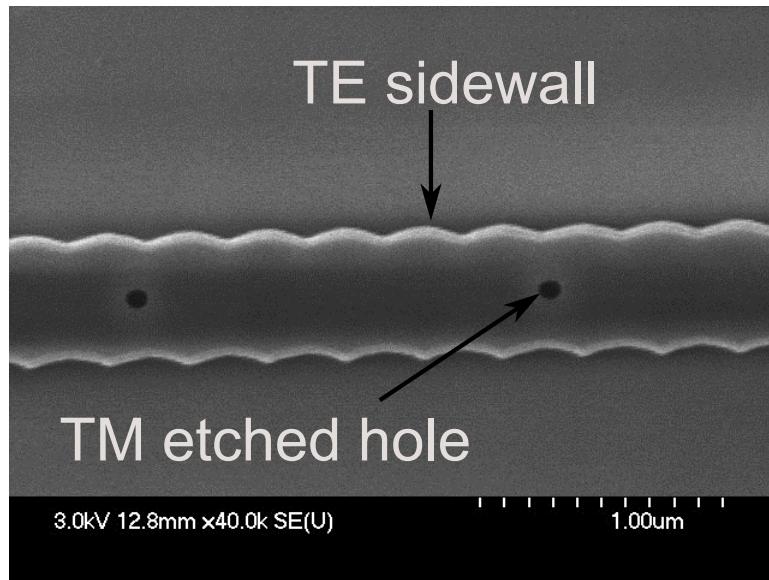


**Figure 3.24:** SEM images of sidewall gratings with overlapped top grating.

The value of TM stop-band that is possible to obtain using this top grating design vary with the radius of the etched holes. Figure 3.25 shows a simulation of TM propagation in these top grating devices for varying hole radius. The radius of the etched holes was varied between 40 nm and 100 nm with an increment of 10 nm.
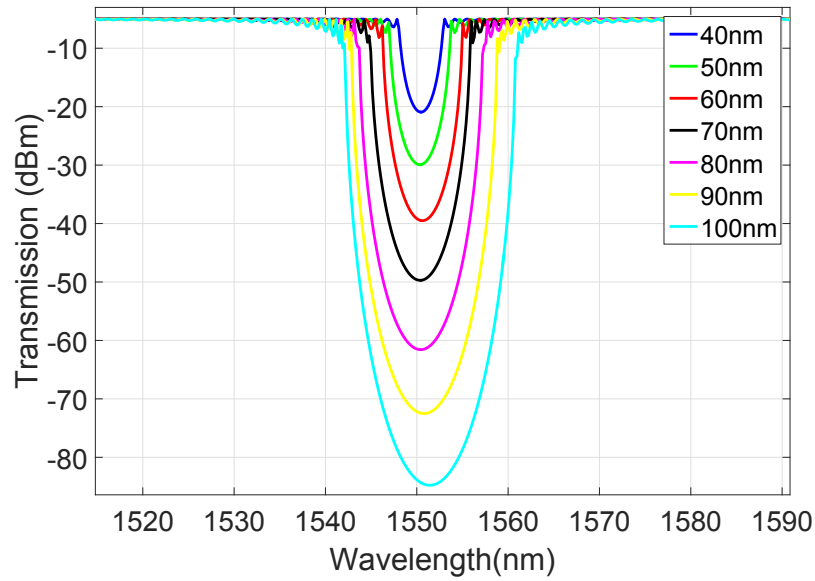
**Figure 3.25:** Simulated spectra of the top gratings for fully etched holes with varying radii. The gratings present a period of $\Lambda = 448$ nm in a 500 nm wide waveguide.

From the simulation is clear how increasing the radius of the holes results in an increase of the stop-band width finding a maximum width exceeding 20 nm for a hole radius of 100 nm .
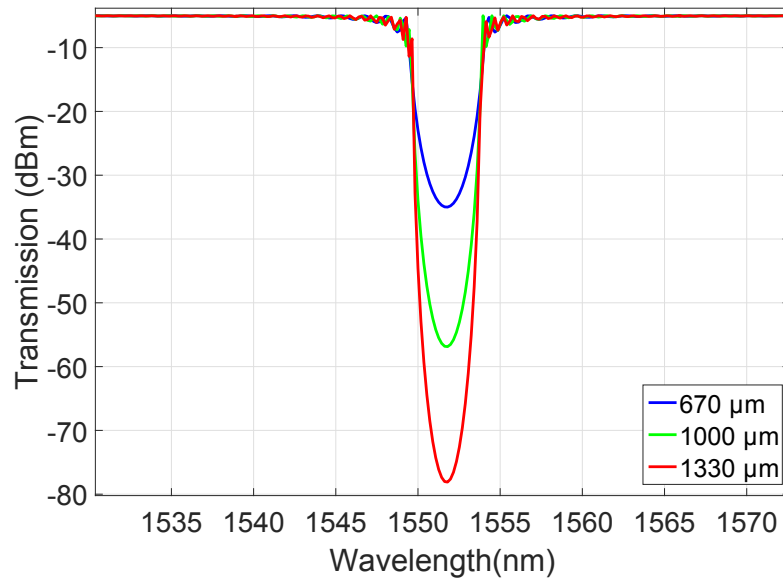


**Figure 3.26:** Simulated spectra of the top gratings for different grating length and for a radius of 40 nm.

Another simulation in Figure 3.26 shows instead that increasing the length of the gratings

does not affect the stop-band width but only improves the extinction ratio. Two SEM images of the TE and TM gratings used for single transmission measurements are shown in Figure 3.27 and Figure 3.28 respectively.
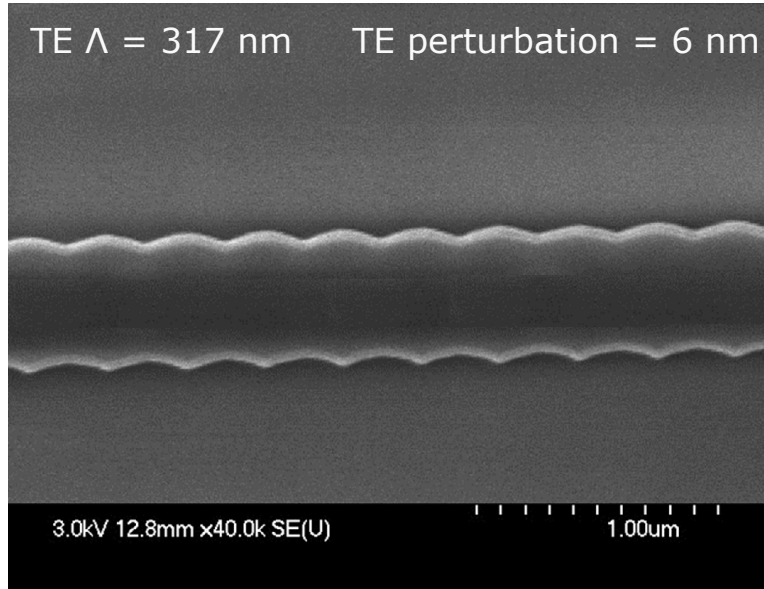


**Figure 3.27:** SEM image of the TE grating used presenting a period of $\Lambda = 317$ nm and a perturbation of 6 nm in a 500 nm wide waveguide.
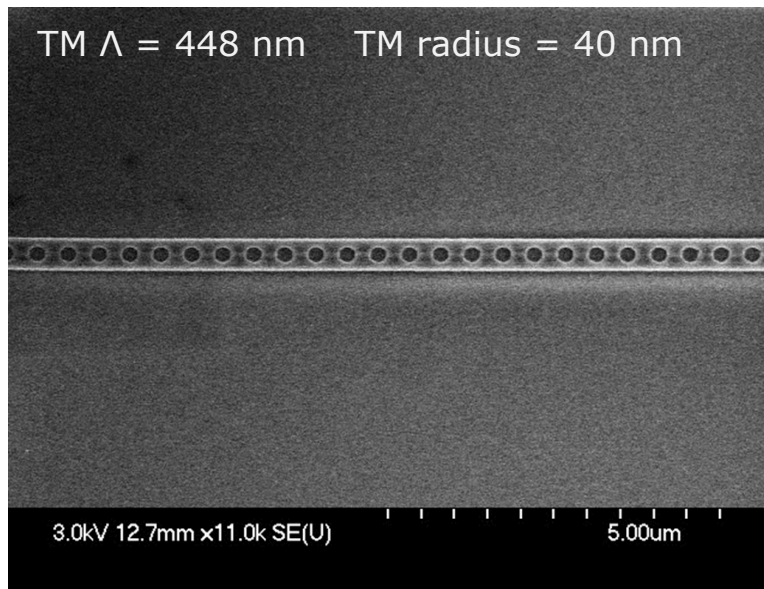


**Figure 3.28:** SEM image of the TM grating used presenting a period of $\Lambda = 448$ nm and a hole radius of 40 nm in a 500 nm wide waveguide.

Figure 3.29 shows transmission measurements for a TE and TM Bragg grating shown in

Figure 3.27 and Figure 3.28 respectively.
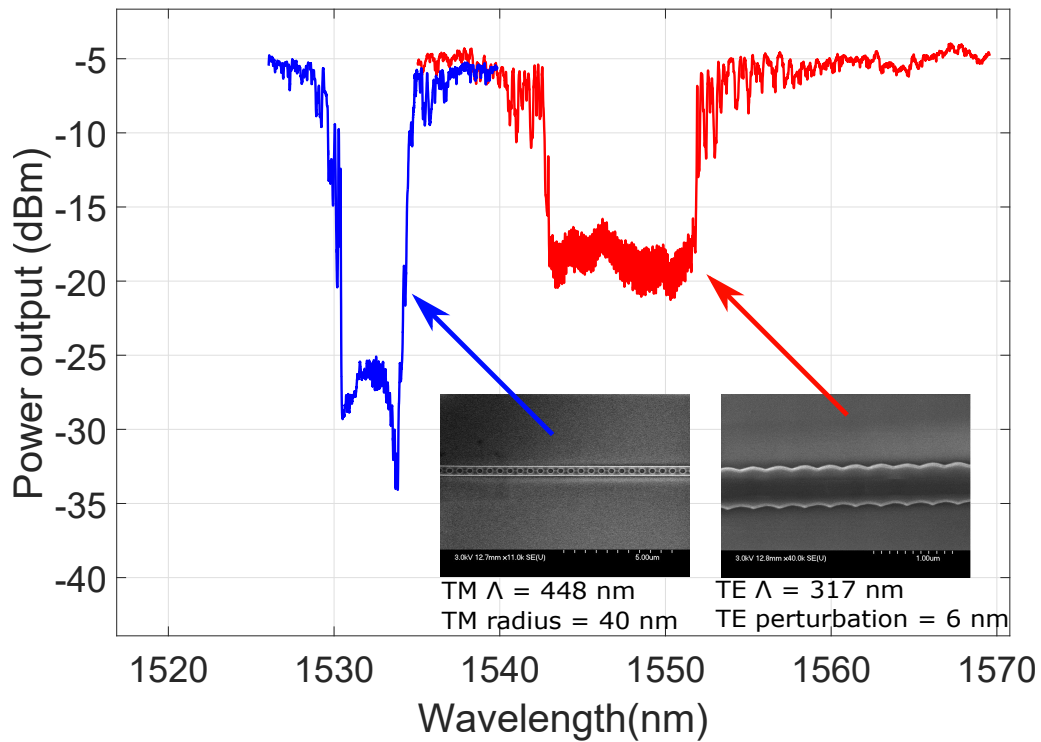


**Figure 3.29:** Transmitted power of a TE Bragg grating for TE injection and of a TM Bragg grating for TM injection.

The red curve represents a TE Bragg grating spectrum measured after TE injection while the blue curve relates to a TM Bragg grating for TM injection. Due to their different structure they present different bandwidth and extinction levels. Even though the TM grating is able to filter more TE polarised mode, both gratings reach a saturation level due to transverse polarisation scattering. In order to clearly observe the case where both TE and TM filters are overlapped, individual filters with different stopband widths were selected.

Co-fabricating the two devices in one waveguide section has an effect on both resonance wavelengths. For the TE mode, the inclusion of the top etched holes slightly reduces the effective index of the TE mode leading to a decrease in its resonance wavelength. For the TM mode, the addition of the sidewall grating, due to non-full clear out of the trough of the modulation profile, leads to an increase of the TM effective index with respect to a single mode waveguide, increasing its resonance wavelength. An effect of these changes in resonance wavelengths is that the two stopbands overlap in one region, creating the desired

dual polarisation filtering effect. Results are presented in Figure 3.30. The fact that the TE and TM stop-band have, in this case, slightly different bandwidths is helpful to confirm the positive effect of overlapping the two gratings, shown in Figure 3.29, in one device.
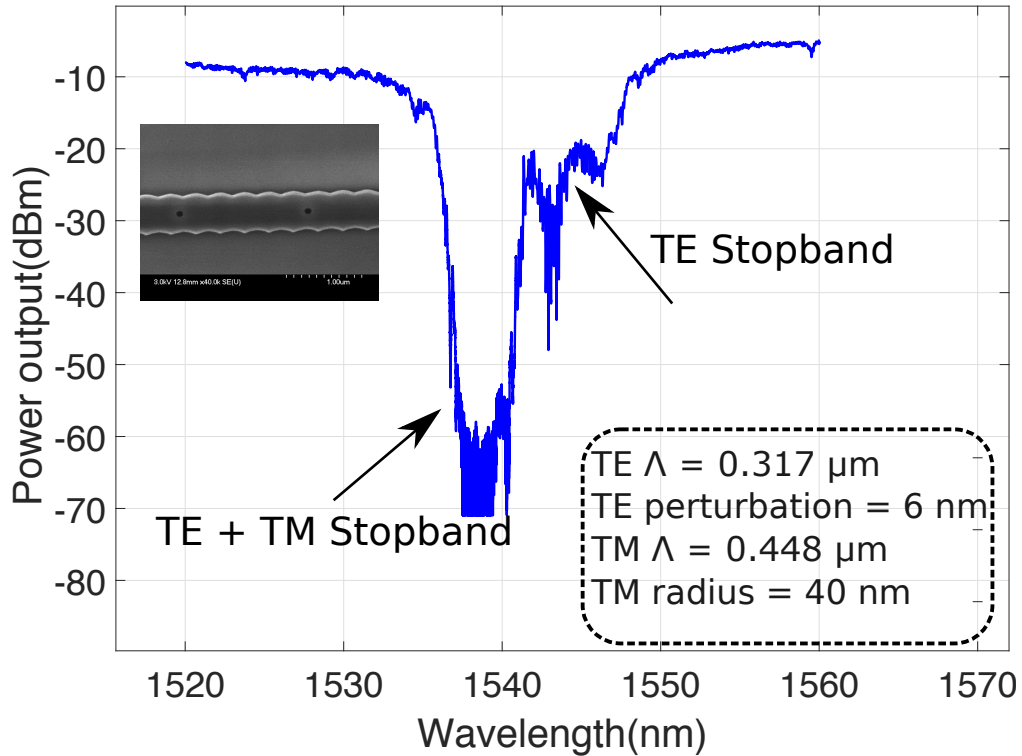


**Figure 3.30:** Transmitted power of the overlap between sidewall and top gratings for TE and TM filtering. An example of a typical Cofabricated TE-TM grating is shown in the SEM image on the insert.

The right portion of Figure 3.30 shows the effect obtained when the two grating stopbands are not overlapped. In this case the TM is allowed through, with only TE filtered. Once the two stopbands are aligned, as shown in the left side of Figure 3.30, the device filters both TE and TM guided modes with an extinction ratio over 60 dB. These results are comparable with those obtained using ring resonators in the previous section. A similar result in terms of extinction ratio and dual polarisation rejection has been obtained with both ring resonators and Bragg gratings. The addition of a TM absorbing metallic layer or top TM grating provides an increase of full TE and TM filtering when injecting a TE signal with extinction of 20 dB.

## 3.6 Conclusions

Wavelength selective filters represent one of the key elements for PICs and many of their applications in linear and non linear optics. TE to TM scattering and transmission are often limiting factors in the design of PICs optimized for TE transmission. Two different geometries of dual polarisation filters based on a cascaded three ring resonator geometry and a Bragg grating respectively, have been demonstrated. Both of these device geometries exhibit high rejection over 60 dB for both TE and TM guided modes. In the next chapter, an application of this technology will also be demonstrated monolithically integrating the filter with an efficient four-wave mixing microring device to filter unwanted pump light on chip. Combining the ring resonator filter technology with a resonant structure for non-linear generation, FWM experiments were carried out obtaining an on chip pump extinction of 62 dB and insertion loss of signal and idler of 1.8 dB.

# Chapter 4

# SOI Photonic integrated circuits for non-linear processes

One of the fields in which it is possible to use the photonic intregrated filters described in the previous chapter is non-linear optics. These devices are found to be particularly useful for applications in four-wave mixing experiments. It is in fact possible to use this filters for two main tasks, filtering the excess pump light and routing the generated photon pair. The first task is crucial in order to obtain a positive outcome from this application. The high power photon of the pump can in fact trigger, after the process, secondary order non-linear effects which can result detrimental for the purpose of the experiment. As stated in the introduction of Chapter 1, in a typical spontaneous FWM application, the pump light on chip has a power in the order of 0 dBm while the produced photon-pair is in the order of -90 dBm [53]. In order to obtain a reasonable signal to noise ratio it is necessary to filter the pump light with a ratio of at least 100 dB .

In this chapter, an introduction on the theory of FWM with details on the performance obtained on FWM in ring resonator will be presented. After this introduction, the results obtained using a ring resonator for FWM generation monolithically integrated with a 3 ring cascade filter will be shown. Using this device it is possible to generate photon pairs through FWM and, subsequently, filter all the pump light, on chip. The pump light is filtered for both TE and TM propagating mode, without affecting the propagation of the photon pair, collected

with low loss at the output of the device.

## 4.1   Four-wave mixing in integrated photonics

FWM is a third-order, non-linear effect occurring when two photons of a beam (pump) scatter with a non-linear material. The result of this scattering is the generation of two new photons at different frequencies (idler and signal) [111]. Four-wave mixing is a Kerr-type effect. The Kerr effect can be described as the non-linear polarization generated when intense light propagates in a medium. This non-linear polarisation modifies the propagation properties of the light changing the refractive index of the material following 2.24: [112]

$$\Delta n = n_2 I \tag{4.1}$$

where $n_2$ is the non-linear index and I the optical intensity.

FWM can occur in any material with a third order $\chi^{(3)}$ non-linearity [113]. Silicon is found to be very useful as a material for third order non-linear application. Silicon in fact exhibits a Kerr non-linearity more than 200 times larger than fused silica [37]. In SOI technology, as a result of the high refractive index contrast that allows to confine the light in very small dimensions, an enhancement of non-linear effects is experienced in this material. This feature enables FWM within a silicon waveguide only a few centimeters long [37].

FWM occurs in optical non-linear materials when two or more different wavelength travel in the same path length incurring in Kerr-type scattering effects. The first main difference is between degenerate and non degenerate FWM. In the non degenerate case the mixing is between three input frequency components $\nu_{pump_1}$, $\nu_{pump_2}$ and $\nu_{signal}$ generating the idler signal $\nu_{idler}$ while in the degenerate case the two pump photons present the same frequency and they add together in intensity. A schematic of the two process is shown in Figure 4.1
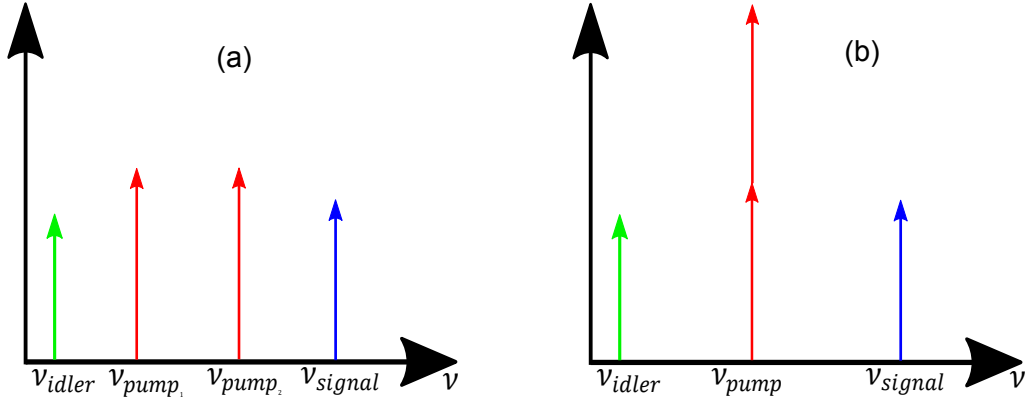
**Figure 4.1:** Schematic of the FWM Theory in the case of (a) non degenerate and (b) degenerate FWM process

In the non degenerate case, the idler frequency $\nu_{\text{idler}}$ can be determined by Eq. 2.25:

$$\nu_{\text{idler}} = \nu_{\text{pump}_1} + \nu_{\text{pump}_2} - \nu_{\text{signal}} \tag{4.2}$$

while for the degenerate case, the idler frequency $\nu_{idler}$ can be determined by Eq. 2.26:

$$\nu_{\text{idler}} = 2\nu_{\text{pump}} - \nu_{\text{signal}} \tag{4.3}$$

this condition is the frequency phase-matching condition. Degenerate FWM is usually expressed using non-linear coupled-mode equations detailed in [112] where the non-linear coefficient $\gamma$ is defined as Eq. 2.27:

$$\gamma = \frac{2\pi f_{\text{p}}}{c} \frac{n_2}{A_{\text{eff}}} \tag{4.4}$$

with $n_2$ non-linear refractive index, $A_{\text{eff}}$ the waveguide effective area and c the speed of light in a vacuum.

### 4.1.1 Possible applications of four-wave mixing

Optical parametric processes such as four-wave mixing (FWM) find their application in many fields like all-optical switching [64, 96], multiwavelength broadcasting [10], and correlated/entangled photon pair generation for quantum optical systems [110, 114]. Many of the applications presented here take place using ring resonators. This because the non-linear effect

can be greatly enhanced by the use of resonating structures. The next section will explain the reasons of this statement supporting it with experimental results.

## 4.2 FWM in ring resonators

Resonant enhancement of these non-linear effects allows their realization with low optical pump powers [110, 49] and therefore the possibility of their inclusion in multicomponent PICs. To take advantage of the resonant enhancement for FWM in a ring resonator, the pump and signal frequencies are typically aligned to resonances, and if the process is phase matched, the idler wave will also be resonant, yielding a tremendous enhancement in efficiency [88]. The internal FWM conversion efficiency $\eta$, defined as the ratio between the generated idler and input signal powers at the output ($10\text{Log}_{10}\frac{P_{\text{idler}}}{P_{\text{signal}}}$) takes into account the cavity enhancement factor due to the ring geometry and is defined by 2.28 [88]:

$$
\begin{aligned}
\eta &= 10\text{Log}10\frac{P_{\text{idler}}}{P_{\text{signal}}} = \left|2\pi R\gamma\right|^2 P_{\text{pump}}{}^2 FE_p{}^4 FE_i{}^2 FE_s{}^2 \\
\eta &= 10\text{Log}10\frac{P_{\text{idler}}}{P_{\text{signal}}} = \left|2\pi R\gamma\right|^2 P_{\text{pump}}{}^2 FE^8
\end{aligned}
\tag{4.5}
$$

where $2\pi R$ is the resonator length, $P$'s are the optical powers and Field Enhancement (FE) is the field enhancement factor estimated for the resonator geometry. This factor comes equally from light recirculation and energy buildup [115] and is related to the ring Q factor from the equations in [88]. In this equation the $P_{\text{signal}}$ is measured away from a ring resonance and when $P_{\text{pump}} = 0$ mW. The idler output power is measured at the output of the chip and all the losses (propagation and coupling loss) are considered equal for both signal and idler beam.

### 4.2.1 Critical coupling

In order to optimise the FWM efficiency presented in Eq. 4.5, it has been demonstrated that the ring resonator needs to operate at critical coupling, e.g., the condition where the round-trip loss factor of the ring is equal to the self-coupling coefficient [56].

Figure 4.2 shows a calculation of the raised FE factor (FE[8]) [115] for FWM, due to ring

resonator presenting the same parameters as the one used for the experiments described in the next section, as a function of κ. The plot can be divided in two main regions. The under-coupled regime of the ring (e.g., $\kappa < \kappa_{crit}$) where the FE factor drops off very quickly and the over-coupled regime ($\kappa > \kappa_{crit}$)) where the FE factor also reduces, but with a shallower gradient.
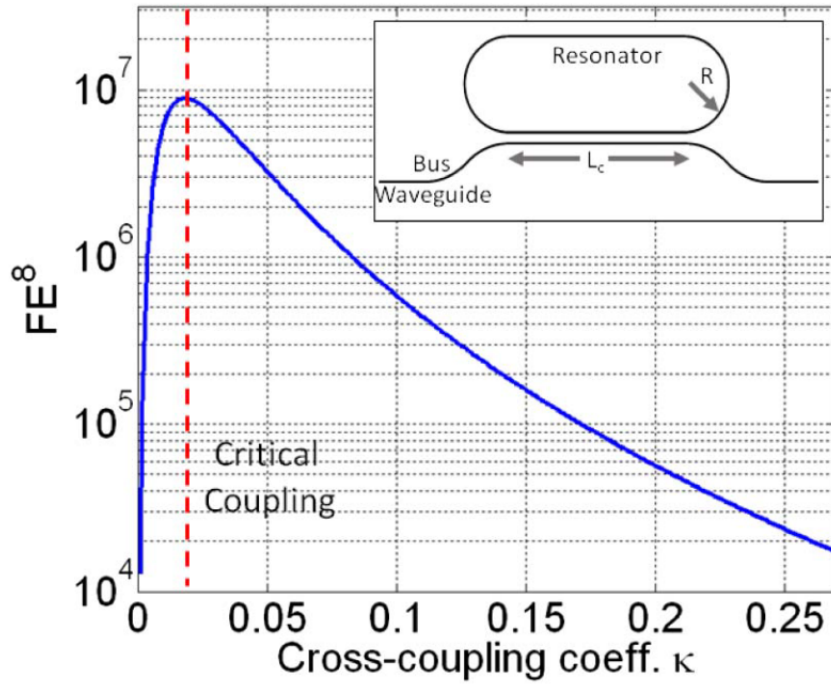


**Figure 4.2:** Calculation of the raised field enhancement factor ($FE^8$) for a silicon microring resonator. (Inset: schematic of the ring resonator device.) [116]

In order to better explain the relationship between the field enhancement factor and the FWM efficiency Figure 4.3 shows results on FWM efficiency in function of the coupling coefficient. These results, as well as the one shown in Figure 4.2 are obtained in [116], a previous work that utilise ring resonators that have the same characteristics and geometry of the one used in this work.
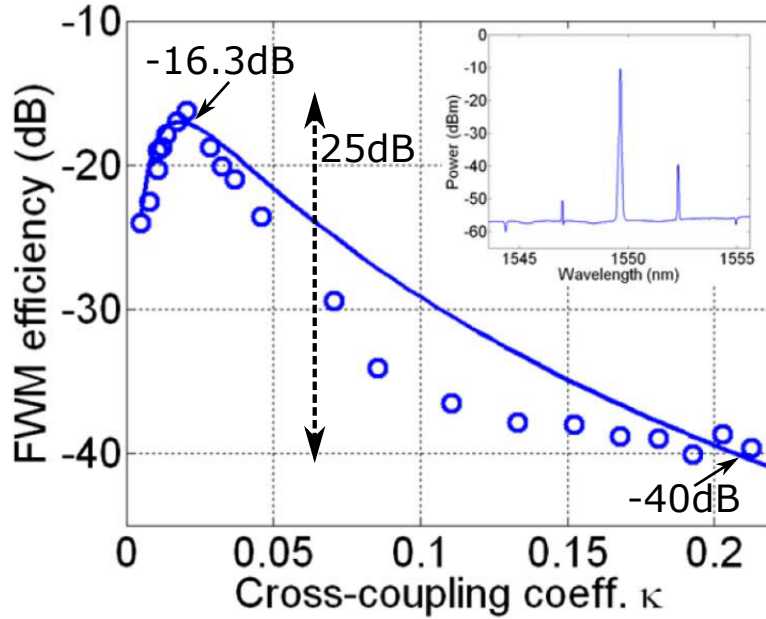
**Figure 4.3:** Measured optical FWM efficiency as a function of power dissipated on the tunable coupler, for Pp = 0.7 mW. The solid line shows the theoretical model, and the open circles are measured data. (Inset: measured FWM spectrum at critical coupling point).[116]

In Figure 4.3, a FWM efficiency of 40 dB for the as-fabricated case is compared to the 16.3 dB peak efficiency obtained at critical coupling. A 25 dB enhancement that confirms the dependency of the FWM efficiency to the coupling coefficient and therefore to the FE factor. The figure shows also that after the maximum point, when the ring is over-coupled, a drop of 10 dB is experienced in the FWM efficiency value for a change of only 0.015 in κ, highlighting the potential sensitivity to fabrication variation and the necessity of fabricating devices that have a very precise and well defined κ. Unfortunately the fabrication tolerances can shift a resonator cross-coupling coefficient by a few percent making almost impossible to precisely control the value of κ during fabrication. One solution is to fabricate a device that allows post-fabrication tuning of the coupling coefficient. As demonstrated in [116], using an asymmetrically placed resistive heating element, it is possible to electrically control the ring resonator coupling coefficient from an as fabricated value of 0.18 to a minimum value of 0.02, crossing the critical coupling point of the ring.

### 4.2.2 Tunable ring resonators

Details on the tuning of the ring coupling coefficient are presented in [104]. In this work, tunable evanescent field couplers [104] are used to control two main parameters of the ring filters, the resonance wavelength and the coupling coefficient, shown in Figure 4.4. This system, using asymmetrically placed resistive heater fabricated above the evanescent field coupler, allows tuning of the resultant FWM efficiency through the tuning of $\kappa$. This solution has been already used to demonstrate high tunable efficiency FWM in ring resonator [116].
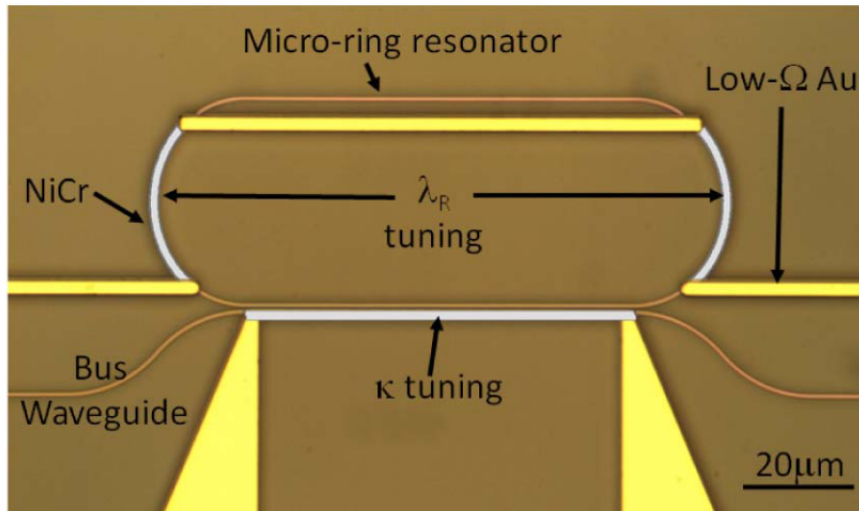


**Figure 4.4:** Optical micrograph of a silicon microring resonator with tunable cross-coupling coefficient ($\kappa$) and central wavelength ($\lambda_R$). NiCr elements are in false color to contrast with low resistance tracks.[116]

All the results that will be now shown are obtained following what previously demonstrated in [104] and [116] but using devices similar to the one presented in Chapter 3. The ring used for this experiments has in fact the same fabrication characteristics and the same coupler length of 42 µm as the one presented in Chapter 3 but present instead a bend radius of 30 µm, double to what presented in Chapter 3. This is to allow the FSR to be double that of the ring in Chapter 3 in order to carry out experiments that will be presented in the next section.

The tuning process consists of applying a thermal gradient between the two waveguides of the evanescent field coupler. This gradient will detune their effective refractive indeces and will consequently dephase the coupler. This dephasing results in a lower cross-coupling coefficient to

the ring, that, to obtain critical coupling, needs therefore to be designed slightly over-coupled. The tuning of the resonance wavelength occurs with the same thermal tuning process that, this time, induces an optical path length change of the ring, shifting the resonance wavelength. The direct tuning of the resonance wavelength can be obtained over a full FSR, this allows to compensate any change due to coupler tuning and to align the resonance wavelength at a set point for further applications. Figure 4.5 shows the transmission spectra of the device, with dissipated power on the resistive heater as a parameter.
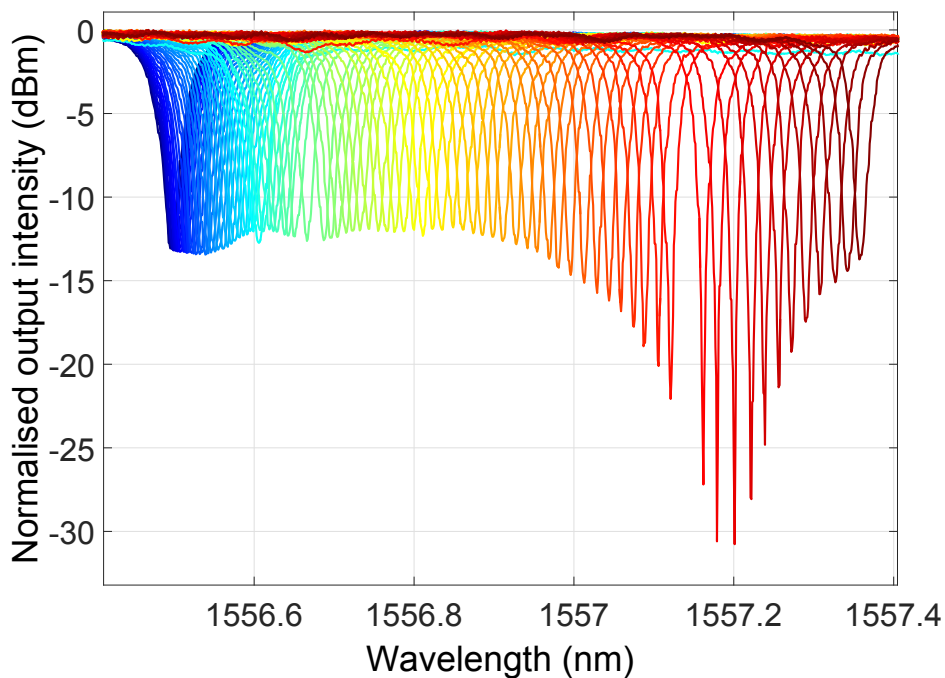


**Figure 4.5:** Measured transmission spectra for a microring resonator with varying power dissipated (from 0 mW to 25 mW) on the $\kappa$ tuning heater.

For the transmission spectra the same experimental setup used for the measurements presented in Chapter 3 is here used. A first indication of the critical coupling point is the extinction ratio of the resonance, this value reaches its maximum when the critical coupling point is approached. Figure 4.6 shows the extinction ratio values obtained as a function of the tuning power.
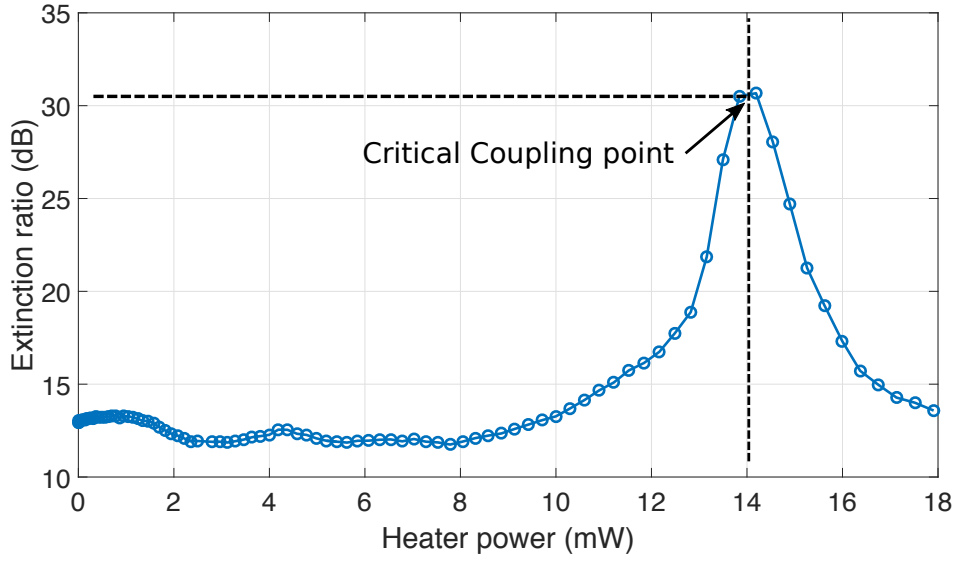
**Figure 4.6:** Extinction ratio as a function of power dissipated in the heater.

The dependency of the ring coupling coefficient, as well as the quality factor, with the power dissipated, can be obtained by curve fitting the transmission spectra to a transfer matrix model of an all-pass ring resonator [100]. An example of this fit method is shown in Figure 4.7. The figure shows a curve fit of the ring resonance at the critical coupling point (calculated to be $\kappa \approx 0.053$.
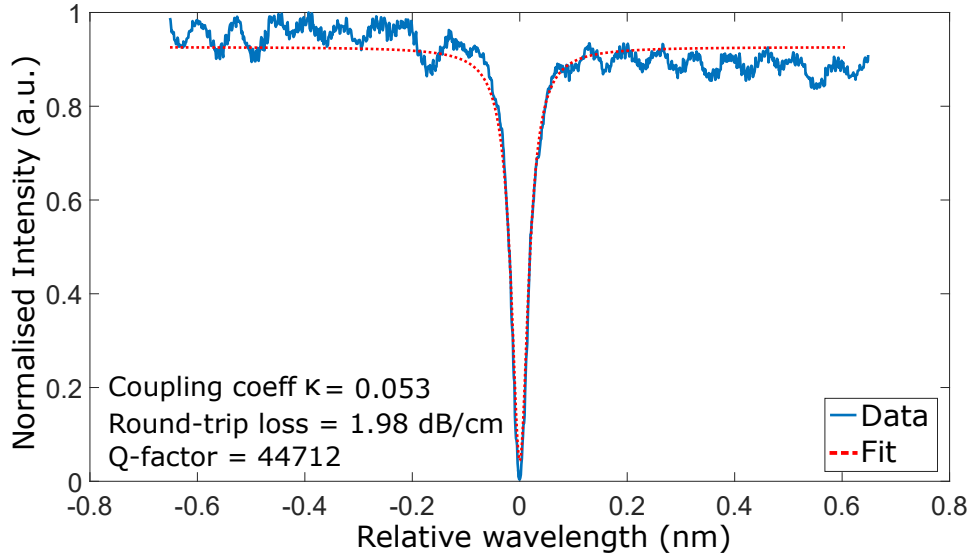


**Figure 4.7:** Fit of ring resonance at critical coupling using matrix method with extracted value of $\kappa$ and Q-factor.

Repeating the same fitting algorithm for all the resonances shown in Figure 4.5 it is possible

to extract the coupling coefficient and the Q-factor as a function of the dissipated power as shown in Figure 4.8 and Figure 4.9 respectively.
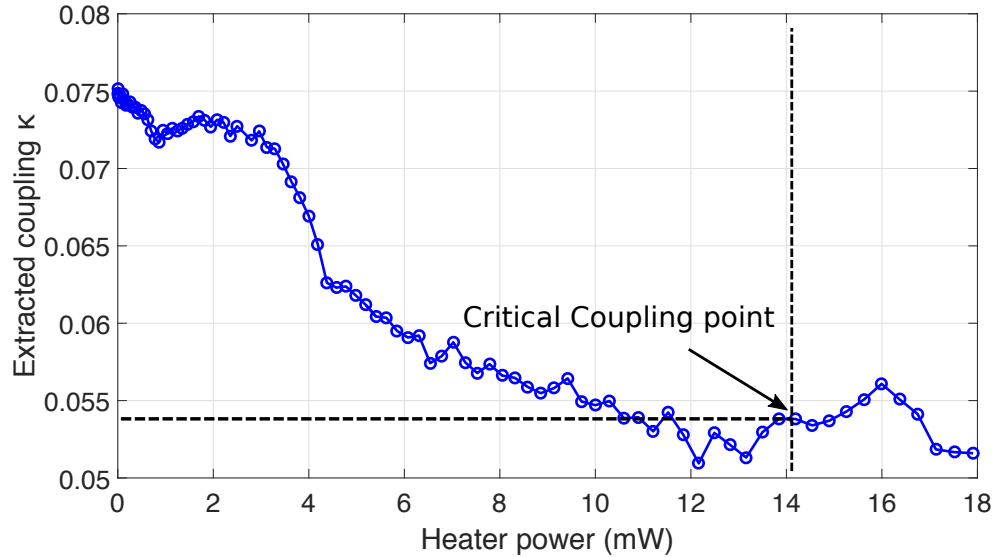


**Figure 4.8:** Ring cross-coupling coefficient $\kappa$ as a function of power dissipated in the heater.

The power required to reach the critical coupling point is shown as dashed lines on the plots. The ring coupling coefficient was tuned from the as-fabricated value of $\kappa = 0.075$, across the critical coupling point ($\kappa = 0.053$), down to a value of $\kappa = 0.05$. Further tuning of the coupling coefficient was limited to avoid damage to the heater device.
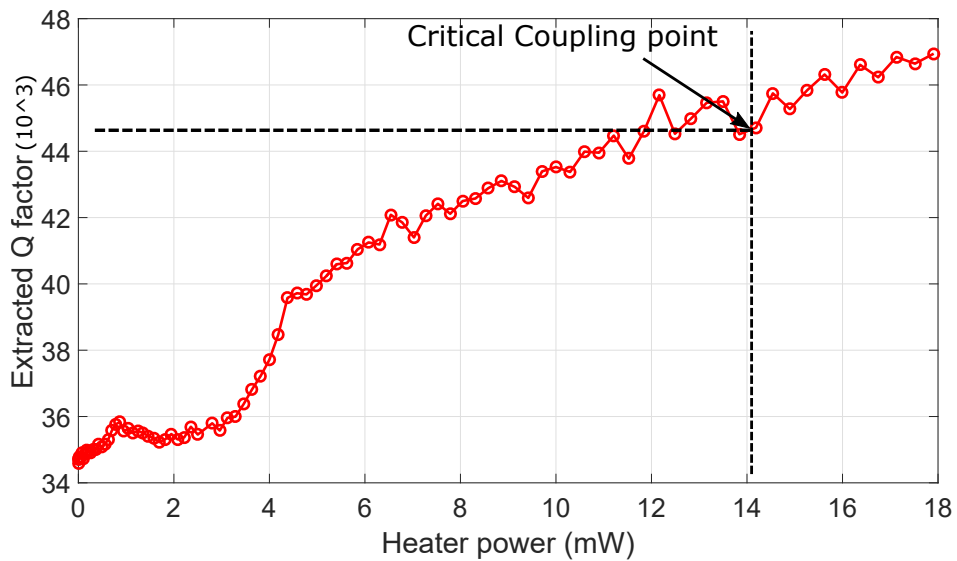


**Figure 4.9:** Ring loaded Q-factor,calculated from the measured linewidth of the resonance, as a function of power dissipated in the heater.

The tuning in cross-coupling coefficient, shown in Figure 4.8, produced a Q-factor change between 34000 and 47000 which plot is shown in Figure 4.9 . The loaded Q-factor of the device at its critical coupling point was 44700. Using the tunable ring resonator device shown in this section it is possible to perform stimulated FWM experiments at the optimum conditions to obtain the maximum of efficiency. These experiments and their results are shown in the next section with previous introduction on the differences between two possible FWM process, the spontaneous and the stimulated FWM.

## 4.3   Main experimental results

### 4.3.1   Spontaneous and stimulated FWM

The two possible FWM described in Section 4.1 have in common the presence of an input signal beam. However, as described in literature [117], this non-linear effect can occur with (stimulated FWM) or without (spontaneous FWM) an input signal beam. Observing spontaneous FWM is of particular interest for application in quantum photonics. This effect is in fact also known as parametric fluorescence and is related to the generation of correlated photon pairs. These pairs are often used to create qubits in quantum information and quantum computation [118]. As explained in [117], it is difficult to obtain information regarding the FWM efficiency only observing spontaneous processes but it is possible to relate the efficiency of spontaneous FWM to the efficiency of the stimulated case, as the two processes originate from the same material non-linearity.

Defining $\nu_{\text{signal}}$, $\nu_{\text{pump}}$ and $\nu_{\text{idler}}$ as the signal, pump and idler frequency respectively, as presented in Figure 4.1, it is possible to say that, for any three resonances with the same $\Delta$Energy in a single-channel side coupled ring resonator, taking the case of a similar Q factor and group velocity and assuming $\nu_{\text{signal}} = \nu_{\text{pump}} = \nu_{\text{idler}}$, the idler resonance power can be expressed as follow:

$$P_{\text{i,ST}} = (\gamma 2\pi R)^2 \left( \frac{Q v_g}{\nu_p \pi R} \right)^4 P_s P_p{}^2 \qquad (4.6)$$

for the stimulated case, and:

$$P_{i,ST} = (\gamma 2\pi R)^2 \left( \frac{Qv_g}{v_p \pi R} \right)^3 \frac{h v_p v_g}{4\pi R} P_p^2 \qquad (4.7)$$

for the spontaneous process, with R ring radius. Conditions to obtain this expressions are the critical coupling condition for the $P_{pump}$ and a $P_{signal}$ tuned to the lowest energy resonance. If the system respects such conditions, these expressions can be calculated following [119].

An interesting comment can be made on the ratio between spontaneous and stimulated powers in a regime of equal pump power $P_{pump}$:

$$\frac{P_{i,SP}}{P_{i,ST}} = \frac{1}{4Q} \frac{h v_p^2}{P_s} \qquad (4.8)$$

from this expression is in fact clear how this ratio is uniquely dependent on the resonance quality factor and a characteristic power $h v_p^2$ no matter what the ring size is. Considering all the equations described so far the main outcome is that using a stimulated process, given the Q-factor, it is possible to determine the number of pairs generated in the, more difficult to obtain, quantum process.

### 4.3.2 Stimulated FWM experiments and results

The experimental setup used is similar to the one described in the previous section with the addition of another tunable laser source used as a pump, amplified through an Erbium Doped Fiber Amplifier (EDFA) and coupled to the first fiber through polarization controls. A 3 dB coupler is also set to the lensed fiber input to the device as shown in Figure 4.10. No polarisation selective off-chip filters have been applied after transmission through the chip.

In order to calculate the power level at which the efficiency of the FWM process is saturated by non-linear losses the device was set to operate at critical coupling and the FWM efficiency was measured varying the power on chip from the EDFA. Results on this measurement are shown in Figure 4.11 and compared with the theoretical curve obtained using the equations described in Section 4.3.1.
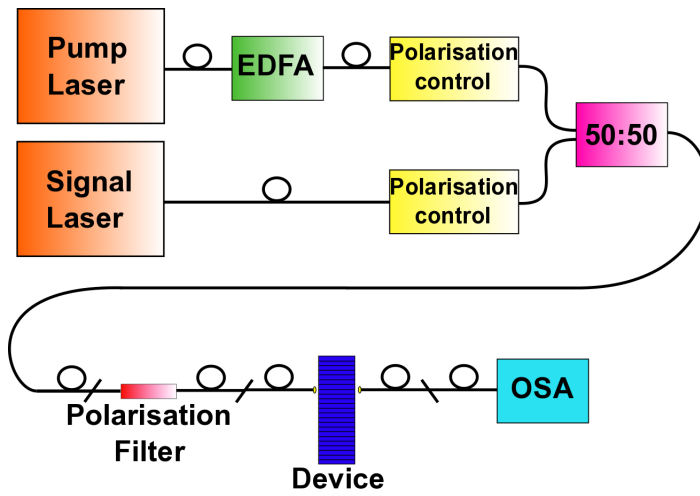
**Figure 4.10:** Experimental setup used for the FWM experiments presented in this section.
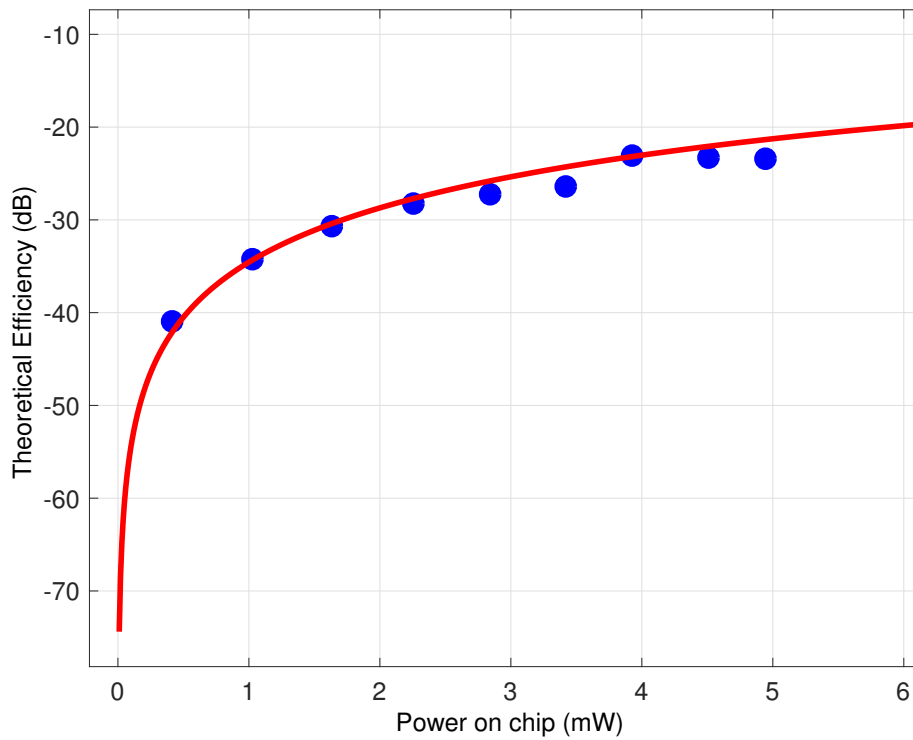


**Figure 4.11:** Measured FWM Efficiency compared with the theoretical curve as a function of the pump power on chip.

This result shows that the FWM efficiency value at critical coupling is saturated by non-linear losses when the pump power on chip is set above 3 mW. This will therefore be the

value of power used in the next FWM experiments. The pump laser wavelength was aligned to a resonance of the ring, around 1557 nm, and the signal laser aligned to the adjacent resonance on the longer wavelength side of the pump. Results on the stimulated FWM obtained with this configuration are shown in Figure 4.12.
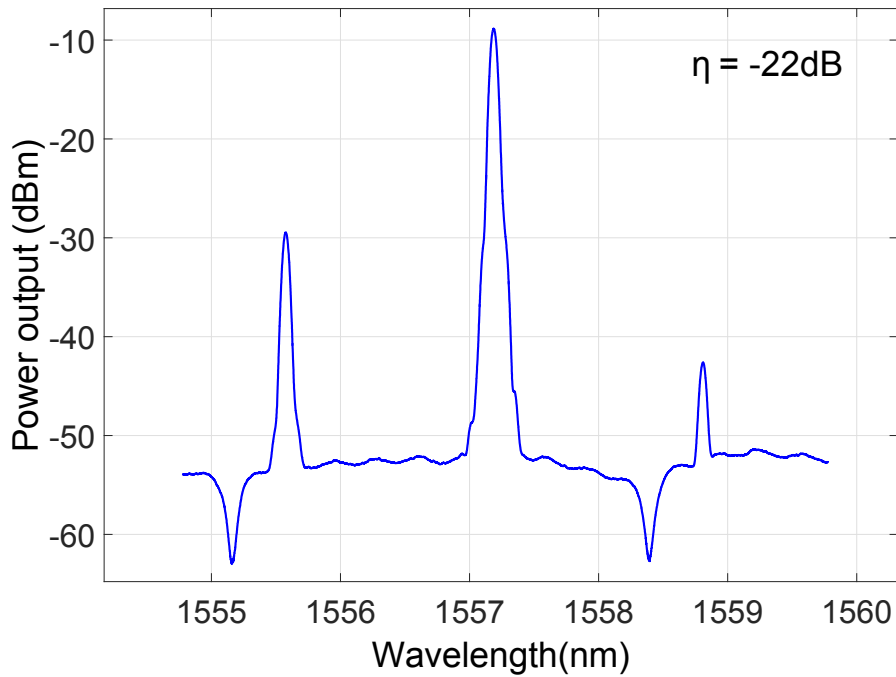


**Figure 4.12:** Main results of FWM Experiment. The figure shows the signal measured at the output of the waveguide showing a 22 dB efficiency calculated from the difference between the signal power output level (left peak), measured off resonance, and the idler output power level (right peak).

Once that the general theory regarding FWM has been introduced and the performance that is possible to obtain using ring resonator on this non-linear process have been demonstrated, it is possible to introduce the main result obtained. As in fact briefly described in the chapter introduction, an on chip dual polarisation filtering of the pump light during a FWM process has been demonstrated. This results, as said before, is obtained by monolithically integrating a ring resonator, used for the FWM generation, with a 3-ring cascade filter. The details on the device fabrication and characterisation are described in the next section together with the results regarding the pump filtering and the photon pair low loss routing, obtained using this novel device.

## 4.4 Full monolithic device for FWM application

In order to show full on chip dual polarisation filtering, one of the possible applications is demonstrated here. In this case the 3 ring cascade filter has been integrated with another ring for non-linear generation, demonstrating a full monolithically integrated FWM source and pump filter system on-chip. The schematic of the device is presented in Figure 4.13.
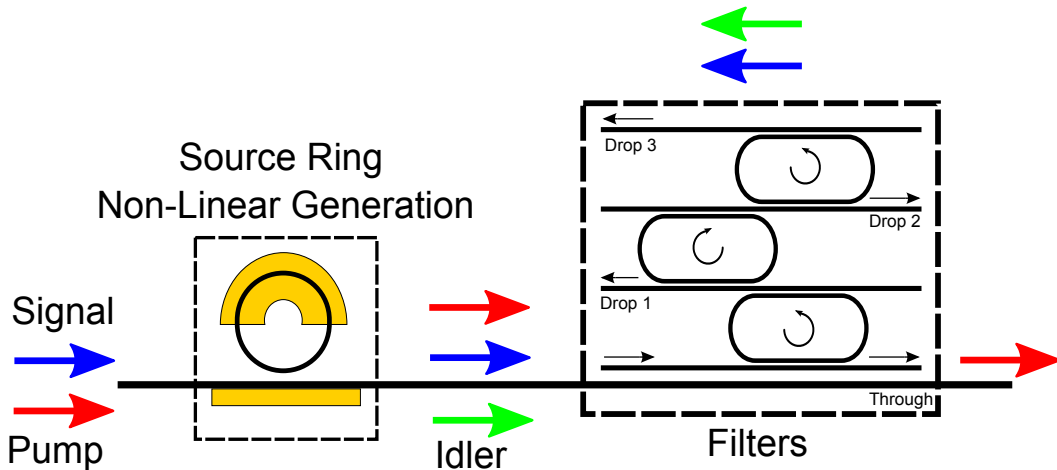


**Figure 4.13:** A schematic of the monolithically integrated four-wave mixing source with dual polarisation cascade filter.

### 4.4.1 Monolithic device and pump filtering

The experimental setup used is the same as the one shown in Figure 4.10 used for the stimulated FWM experiments. In order to perform the non linear generation and filter the pump light after the process the system needs to be tuned and aligned as follow.

From the schematic in Figure 4.13 it is possible to see how the first ring resonator is responsible for the non linear generation while the 3-ring cascade will perform the pump filtering process. It is therefore necessary at first to align all the three resonance wavelengths involved in the process (signal, idler and pump) in a way that will allow to the signal and the pump to be transmitted through the filter device and to the pump to be appropriately filtered. To do so the first ring resonator has been designed with double the radius respect to the ring used for the filter and it therefore has a FSR that is half of the cascade one. Having this will allow to align the signal and the idler wavelength with two of the cascade filter resonances

positioning the pump wavelength in between them as shown in Figure 4.14
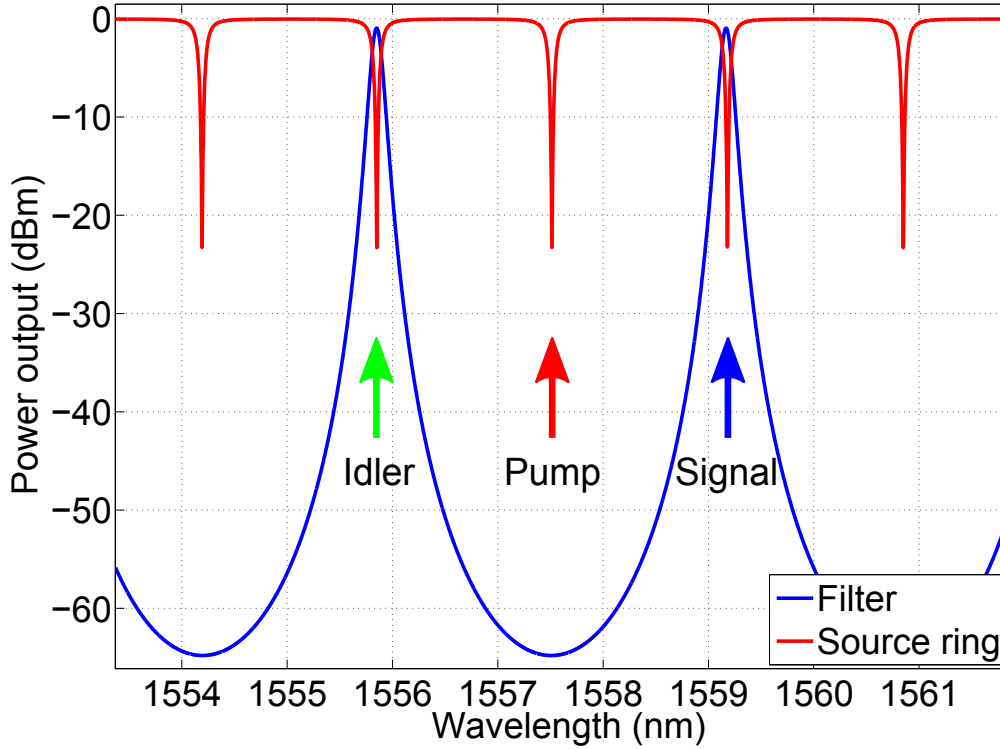


**Figure 4.14:** Resonance alignment to perform to obtain efficient ring resonator and pump filtering.

As explained before, the tuning process consists on applying a thermal gradient on the ring resonator. This gradient will induces an optical path length change of the ring, shifting the resonance wavelength. The direct tuning of the resonance wavelength can be obtained over a full FSR, this allows to compensate any change due to coupler tuning and to align the resonance wavelength at a set point for further applications. Other heating elements are also present in the first ring resonator to allow the tuning of the cross coupling coefficient as detailed in Section 4.2.2.

### 4.4.2  Tuning process

The tuning process is obtained using a multi-probe that allows to electrically control all the 4 rings at the same time applying the appropriate detuning voltage to each of them. The steps to follow on this tuning process are detailed as follows. The first step is to obtain critical coupling condition on the ring resonator used for the non linear generation. The effect of this

tuning process is detailed in Figure 4.15.
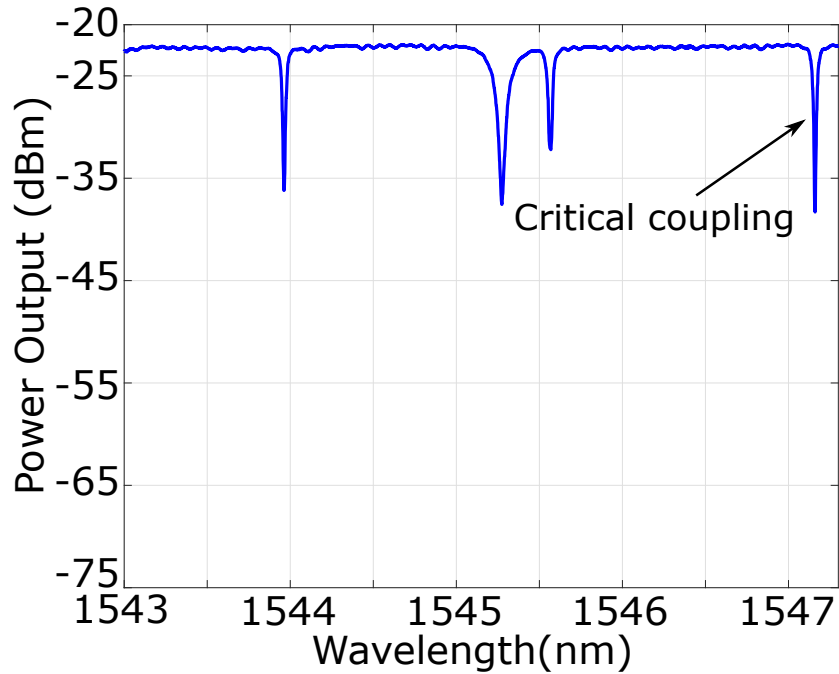


**Figure 4.15:** This is the first step in which the Source ring is tuned to the critical coupling condition.

Once the source ring is at its critical coupling point, the filter resonance wavelengths needs to be aligned with that of the source ring. Applying some voltage to the filter as well as to the first ring will cause a shift of the first resonance wavelength aligned in the previous step. It is therefore necessary to slightly tweak all the values of voltage when a new probe channel is activated. Figure 4.16 shows the through port resonance of the cascade filter when aligned with the source ring.
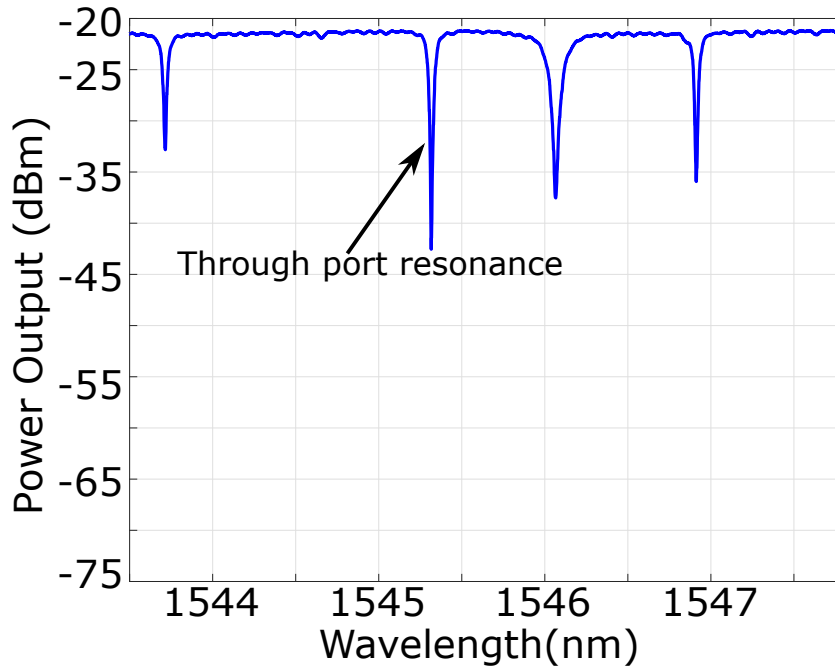
**Figure 4.16:** This is the second step in which the Through-port is aligned with the resonance of the source ring.

The next step is to align between each other all the resonances of each ring resonator on the filter. This will allow the signal and idler to be collected at the output after the third ring with the smallest propagation loss. Figure 4.17 , Figure 4.18 and Figure 4.19 show the transmission spectrum of the first, second and third ring respectively, once aligned with each other as well as with the source ring.
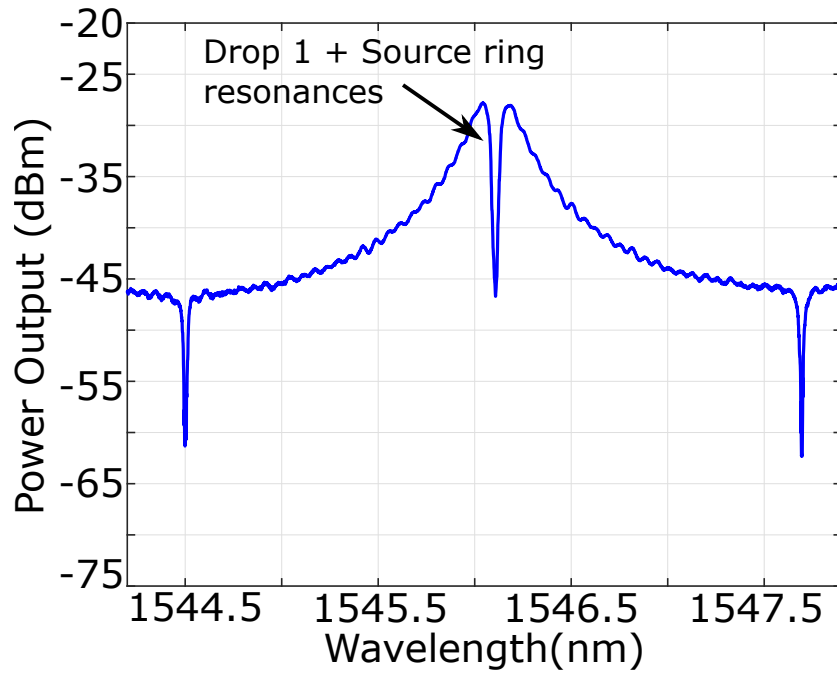
**Figure 4.17:** This is the third step in which the Drop 1 port is aligned with the resonance of the source ring.
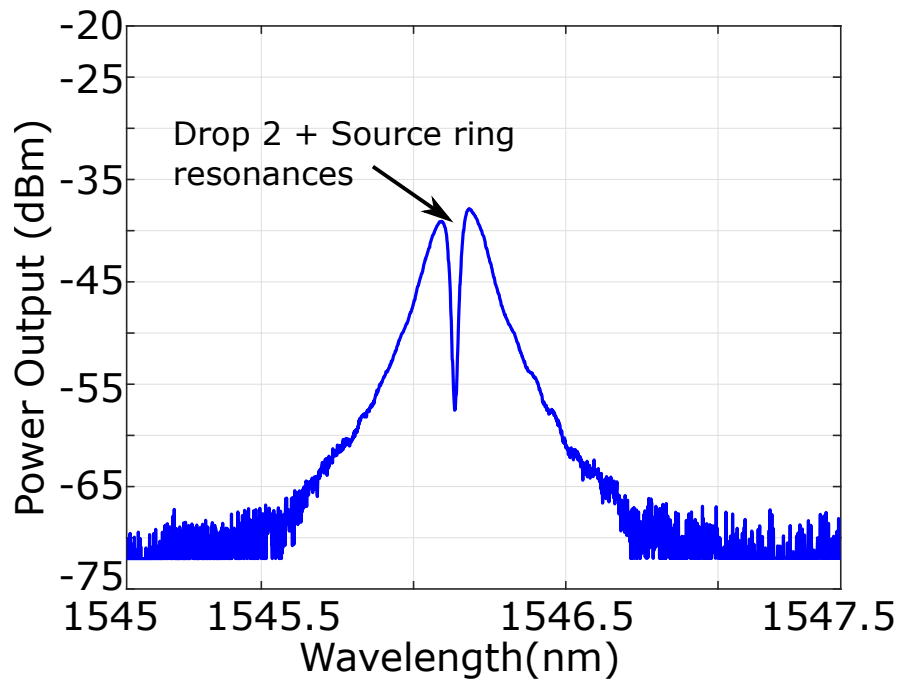


**Figure 4.18:** This is the fourth step in which the Drop 2 port is aligned with the resonance of the source ring.
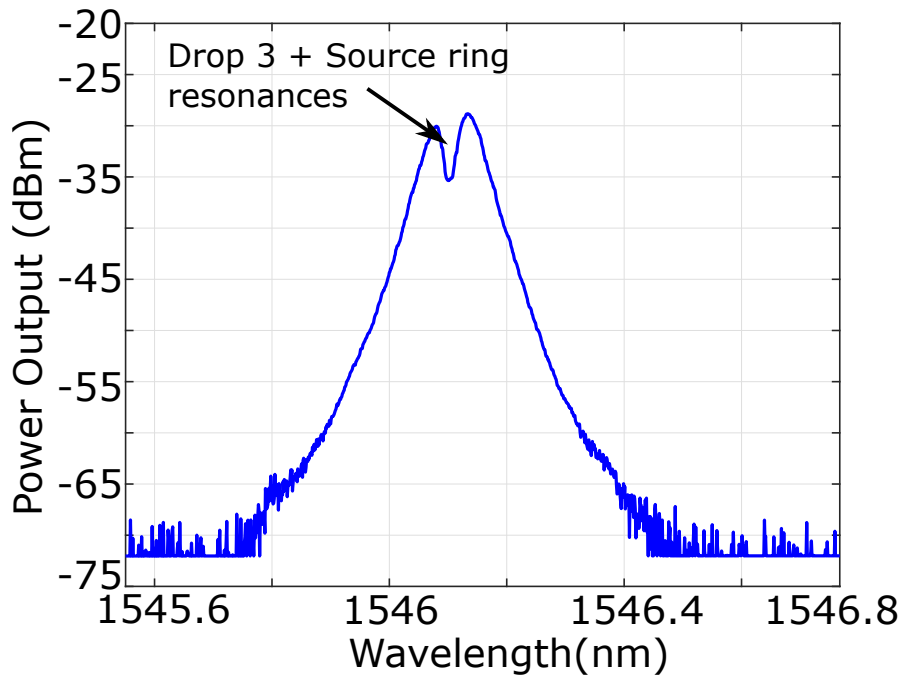
**Figure 4.19:** This is the last step of the tuning process in which the Drop 3 port is aligned with the resonance of the source ring.

This tuning process is fundamental for the FWM and pump filtering and it is in always in operation during the experiment. As it will be possible to see in the next chapter, due to thermal instability caused by the high power pump light, the last alignment, shown in Figure 4.19 is not easy to maintain and it is very likely to be lost. A solution could be represented by a feedback loop control system that constantly monitors the alignment and corrects it when necessary. Such a system will be shown in the next chapter together with its applications in another non linear process in PIC.

### 4.4.3 FWM and pump filtering results

The process is made of four main steps. In the first one, shown in Figure 4.20 the signal and the pump are injected in the untuned device; it is therefore necessary to calculate the voltage to apply to each channel to tune the rings' resonance wavelengths correctly.
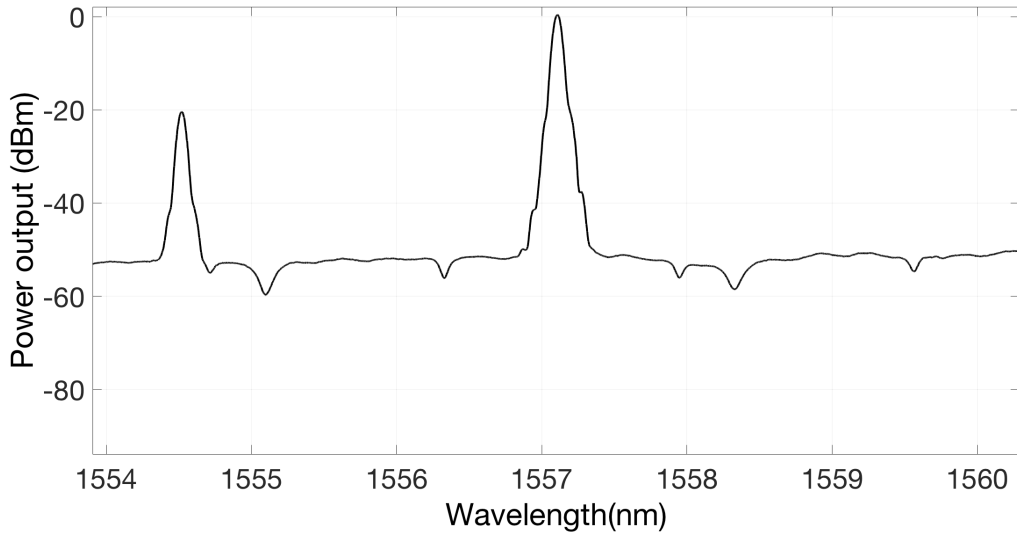
**Figure 4.20:** Filter through-port output. The signal and pump light are injected into the device in an untuned condition.

Once the first ring is tuned to reach the critical coupling condition the signal can be tuned in wavelength to be aligned with one of the source ring resonances while the pump is directed to the next source ring resonance. Using a pump power of 4 mW a FWM non linear generation with peak conversion efficiency of -22 dB observed in the filter through port as shown in Figure 4.21.
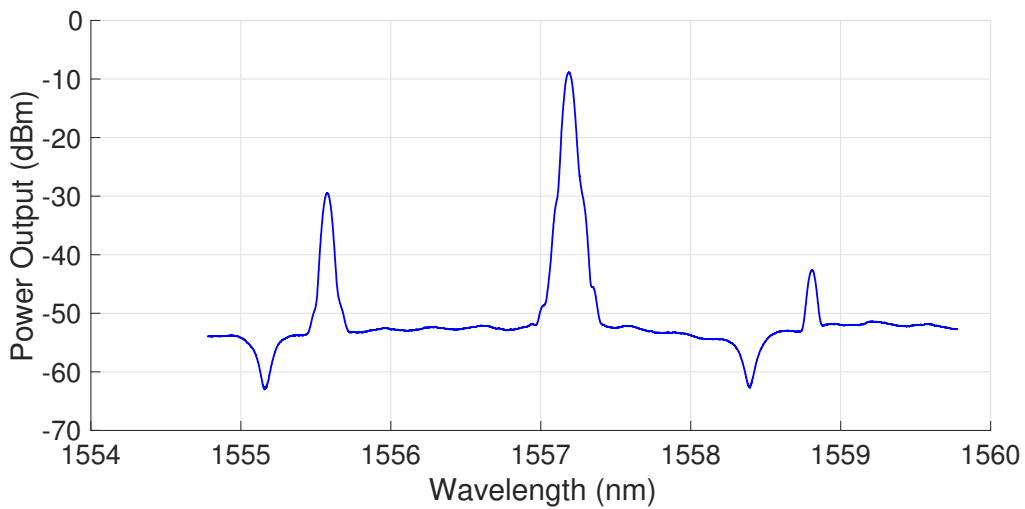


**Figure 4.21:** Filter Through port output, the FWM process is visible after the source ring is tuned to the critical coupling condition.

After the non-linear generation has been performed the filter is then tuned to have its

resonance wavelengths aligned with the source ring. It is therefore observed in Figure 4.22 how the signal and the idler reduce their power output on the through port since they are now being transmitted through the 3 ring cascade to be collected at the output of the filter. The pump, which wavelength does not match any of the filter resonances, won't be transmitted through the filter.
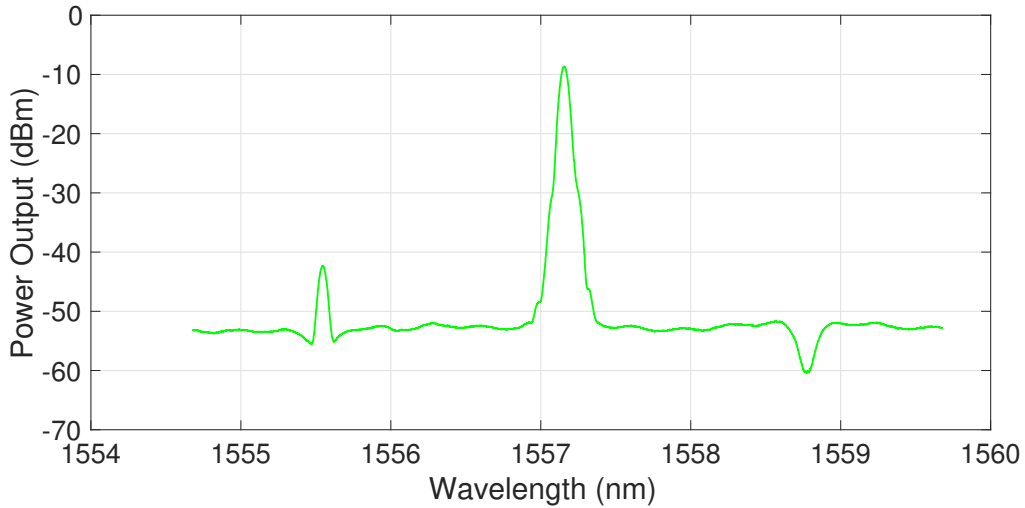


**Figure 4.22:** Filter through-port output after alignment of the filter resonances with the source ring. The signal and the idler are coupled in the 3-ring cascade filter and will be visible at the drop-3 port.

Figure 4.23 shows the output after the three stage of filtering. The residual pump light transmitted through the drop-3 port is reduced down to the substrate scattering noise level of our system. Transmitted signal and idler show insertion losses of 1.8 dB, matching the linear transmission measurements.
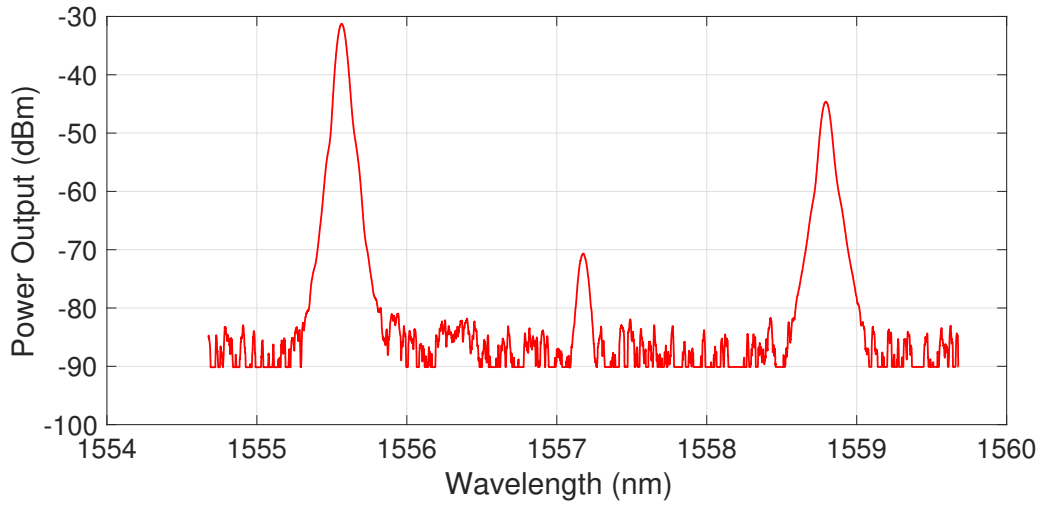
**Figure 4.23:** Filter drop 3 port output. This signal is collected after the three stage of filtering. The signal and the idler have been transmitted through the ring and the pump, out of resonance, has been filtered away. Substrate scattering light is visible around 1557 nm.

Tuning the pump light between two of the filter's resonances it was then possible, as summarised in Figure 4.24, to transmit the signal and the generated idler to the Drop 3 output filtering the pump light.
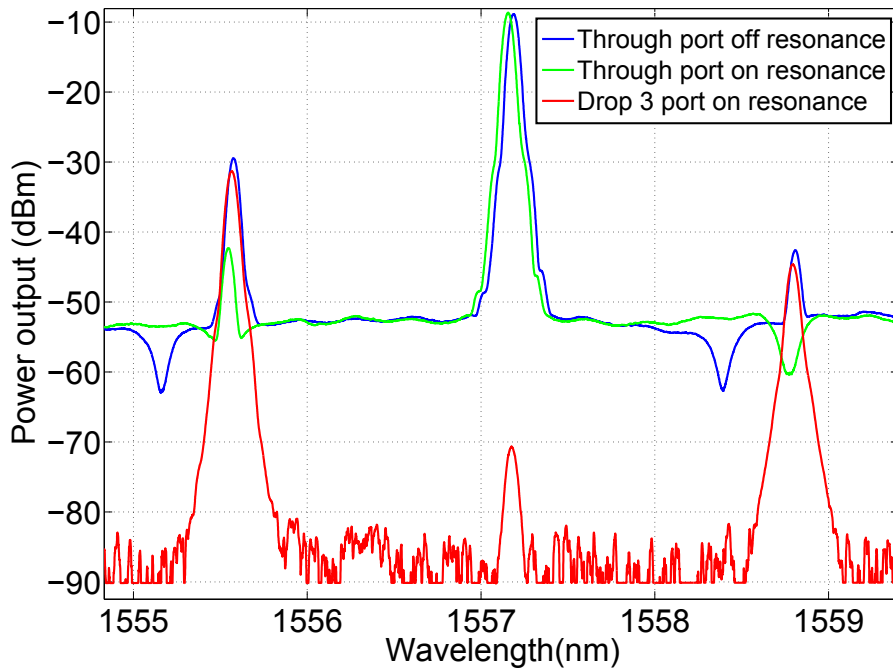


**Figure 4.24:** four-wave mixing with filtered pump power. The blue curve shows the FWM at through port with the source ring off resonance while the green and the red curves show the FWM at through and drop-3 port respectively with the source ring on resonance.

The peak appearing around 1557 nm in the drop-3 port in Figure 4.23 and Figure 4.24 is in fact not related to waveguide transmitted pump light but rather to scattered light in the device substrate. Figure 4.25 shows that this scattered light is related to the distance of the output fibre from the filter's output waveguide. To decrease its level by 10 dB it was necessary to move the output fibre 1 mm away from the output waveguide, confirming that this signal is not due to guided light.
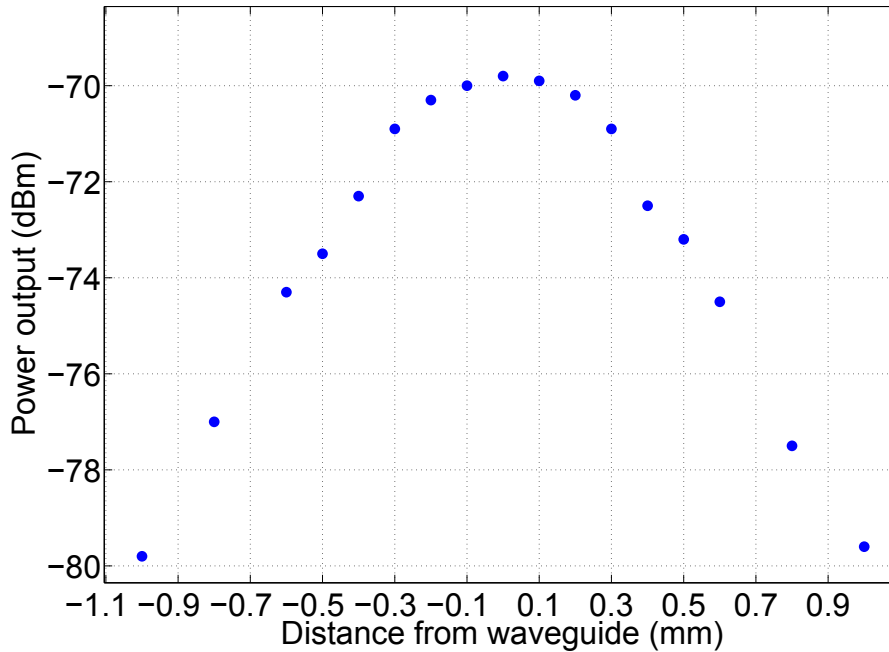


**Figure 4.25:** Substrate light scattering captured by the output lensed fibre as a function of the distance from the output filter's waveguide.

## 4.5   Conclusions

In this section the non-linear four-wave mixing effect has been exploited including a review of possible applications in integrated photonics with particular attention on application with ring resonators. It has also been shown how the FE factor has a main role on the FWM efficiency optimisation and how, given fabrication tolerances, this value can shift drastically only with a change in resonator cross-coupling coefficient of a few percent. An active tuning of the device post-fabrication needs therefore to be implemented in the chip electrically controlling with resistive heating elements, the ring coupling coefficient. FWM efficiencies were demonstrated

at milliwatt power levels using this tunable ring device. In the last section, combining this non-linear generation device with the ring resonator cascade filter technology presented in Chapter 3, FWM experiments were carried out obtaining an on chip pump extinction of 62 dB and insertion loss of signal and idler of 1.8 dB.

# Chapter 5

# Active control of PICs

Stabilization of SOI resonating structures is a key requirement for their future integration in PICs. One particular effect to control is the thermal refractive index shift that, in non-linear applications, can detune devices from their optimal working point. In this chapter a micro-processor based feedback control loop is used as a cavity stabilization scheme. This control loop is implemented to stabilise the operation of a silicon $\pi$-phase shifted grating over an ambient temperature detuning range of $40\,^o\mathrm{C}$ and injection wavelength range of $1.5\,\mathrm{nm}$, a value nearly 3 orders of magnitude greater than the resonant cavity linewidth.

## 5.1 Introduction

A wealth of useful non-linear modes of operation have been demonstrated on SOI platform, including: Kerr non-linearity for FWM [120, 121, 122], photon pair generation [123], thermal refractive index non-linearity for optical bistability and all-optical signal processing functions [124]. Thermal refractive index variation of the resonant wavelength is increased in the case of micro-resonator devices; this is due to the higher photon lifetime in the cavity and to the resonant enhancement of the field in a small mode volume. In order to obtain the maximum of performance in non-linear application it is important to operate the system at the point of maximum resonant enhancement, which requires precise alignment of the resonator wavelength and input laser signal. The alignment between the resonator and the laser can be achieved

by tuning the laser from the blue spectral side of the resonant line into the cavity. In the alignment, the power in the cavity increases with the wavelength and therefore the thermally induced refractive index of the resonant line shift. The thermal refractive index increase shifts the resonant line towards the red as the laser wavelength approaches the cold cavity peak. Once reached a critical point of detuning to the red side of the cold cavity peak, the system comes back to the cold cavity state since the thermally induced refractive index shift is no longer sufficient to align the cavity resonance with the laser line. In Figure 5.1 the measured transmission spectrum for a silicon waveguide resonator is shown. In this figure is it possible to see how the injected power is sufficient to induce a thermal refractive index effects. The device used for this demonstration is a $\pi$-phase Bragg grating which details will be discussed in Section 5.2.1.
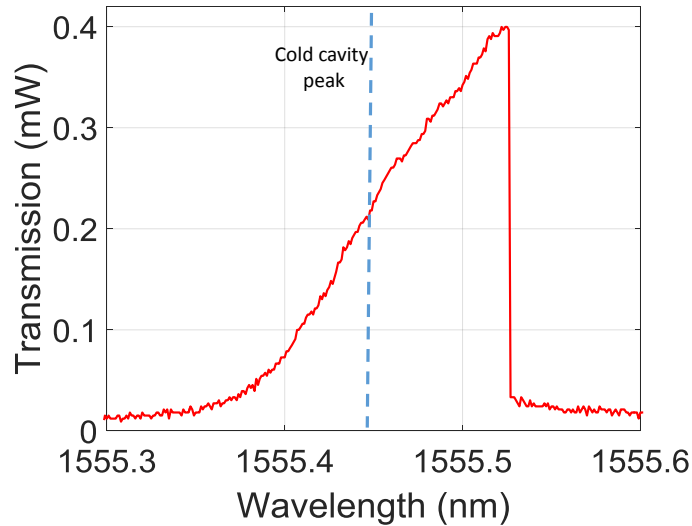


**Figure 5.1:** Demonstration of resonantly enhanced thermal refractive index detuning effects using the transmission spectrum of a silicon $\pi$-phase shifted grating.

Another effect that can induce detuning in SOI micro-resonator structure is the variation in the environmental conditions. Silicon in fact exhibits a relatively high thermal coefficient of refractive index, $1.8 \times 10^{-4}$ K$^{-1}$ [125]. This thermal coefficient plays an important role in wavelength detuning processes. Taking, for example, a Bragg grating device, which resonance wavelength is proportional to the effective index and the grating period, a change of $0.1$ K on a grating with a period of $318$ nm and an effective index of 2.445, can result in a resonance shift of over $10$ pm. This shift can significantly affect the operation of the device since its value is of

the same order of a high-Q cavity resonance linewidth. Given a fixed wavelength it can in fact generate a device detuning from the laser signal disrupting its non-linear operations reverting the resonant enhancement to the cold cavity case. It is therefore clear how these effects needs to be controlled and corrected in order to avoid discontinuities in any experimental setup.

Cavity stabilization in silicon photonic devices has already been demonstrated using both electrical [126] and thermal [127] elements on-chip. All these demonstration have been designed in order to track the cavity line in linear optical applications such as data communications. These applications are not suitable for non-linear application where the dithering, used for the symmetric cavity lineshape stabilisation will push the device towards the long wavelength side, after the "switch-off" point.

In this work a stabilisation scheme suitable for cavities operating in the non-linear regime is demonstrated. This system allows to actively stabilized the cavity using a simple thermal control element. In the next section, details on the device technology and fabrication processes are presented together with experimental setup designs and details of the stabilization scheme.

## 5.2 Materials and Methods

### 5.2.1 $\pi$-phase shifted Bragg grating design and fabrication

In order to demonstrate the effects of active stabilization on high-Q cavity resonators, a $\pi$-phase shifted Bragg grating geometry is used. Nevertheless, the demonstrated effects are applicable across resonator types.

High-Q, $\pi-$phase shifted gratings have been demonstrated [128]. These devices can be used for single resonance line operation maintaining moderate cavity lengths. In this case, the grating is realised as a sidewall modulation of the silicon ridge waveguide [129]. Using this system it is possible to integrate the grating with single mode waveguides in the same fabrication process controlling the grating spectral response through modulation of the grating period and amplitude [130]. The $\pi$-phase shift is fabricated as a half-period delay in the grating modulation at the centre of the device, created as a section of straight waveguide. The grating delay of $\Lambda_0/2$ is realized at the midpoint of the perturbation amplitude in order to

create a $\pi$ phase shift.

Figure 5.2(a) shows a schematic of the device while a SEM image of the $\pi-$phase shift section is shown in Figure 5.2(b).
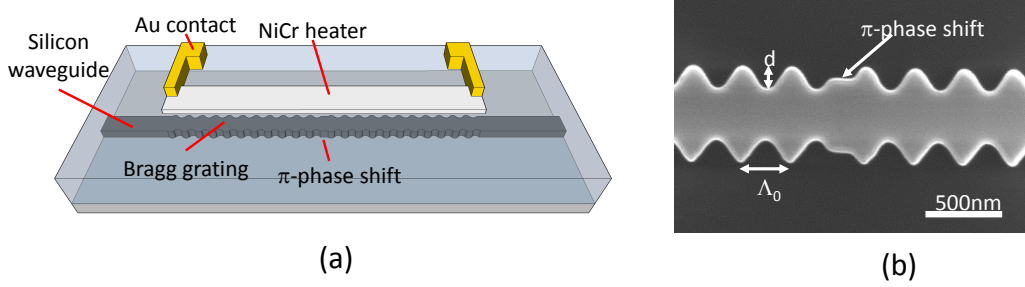


**Figure 5.2:** (a) Schematic of a silicon $\pi-$phase shifted grating with resistive heating element for wavelength tuning and thermal stabilization. (b) SEM image of the phase shift section at the centre of a grating device (a device with d=70 nm is shown to best illustrate the grating modulation profile).

The cavity wavelength tuning mechanism used in this work is achieved by fabricating a thermal tuning element above the grating device, as shown in Figure 5.2(a). By applying a voltage across the heater localized temperature variations can be applied to the device and therefore control exerted over its resonance wavelength [126, 131]. The devices fabricated in this work were produced on a SOI wafer with a 220 nm thick silicon core. Gratings were defined using e-beam lithography with HSQ as a mask. The waveguides were nominally 500 nm wide with a 5 nm perturbation amplitude, $d$. The grating was 628.5 periods long. The devices were clad with a PECVD and spin-on-glass coating, and finally a resistive heater was fabricated directly above the grating as an 800 nm wide, 50 nm thick layer of NiCr. The NiCr heater was contacted using low resistance gold tracks.

### 5.2.2 Measurement setup

The measurements presented in this work were carried out using a setup which schematic is shown in Figure 5.3. The tunable laser output was coupled onto the silicon chip via a lensed optical fiber and polarization control. A compact InGaAs camera was used to measure the top scattering from the chip and the output facet was imaged onto a photo-detector via a microscope objective. Transmission spectra were measured by using the tunable laser in swept

mode and measuring the output power on the oscilloscope.
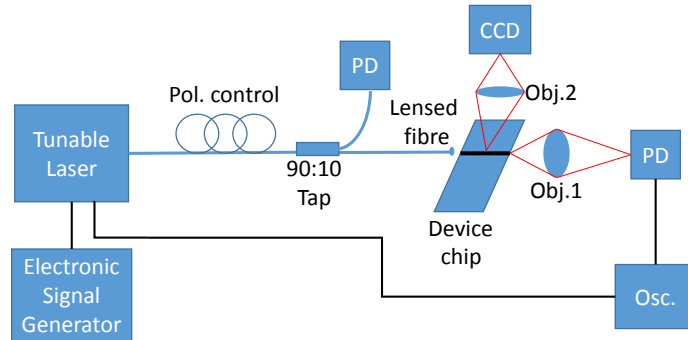


**Figure 5.3:** Schematic of the measurement setup. Obj.1 and 2 are objective lenses for imaging the device facet and top surface respectively, PD are photodiodes and Osc. is a digital oscilloscope. CCD is an InGaAs CCD camera.

### 5.2.3   Cavity stabilization scheme

Using the local thermal heater detailed above it is possible to control the relative position of the laser injection wavelength and cavity resonance. This control method makes use of the known spectral transfer function of the device. It is possible to measure the linear losses, the resonator Q-factor and lineshape and the central resonant wavelength by measuring the cold cavity spectrum of the device. It has been demonstrated that, given the thermal refractive index coefficient of silicon, along with the absorption in the resonator and thermal dissipation, the transfer function can be calculated as a function of injection power [124]. Using this transfer function in Matlab, simulated transmission spectra of a $\pi$-phase shifted grating are calculated using the same parameters of the fabricated device. The simulations has the injection power as parameter and are shown in Figure 5.4. The simulation was obtained using a transfer matrix method solution to the coupled mode equations [132], where the refractive index is a function of the power in the resonator mode volume.
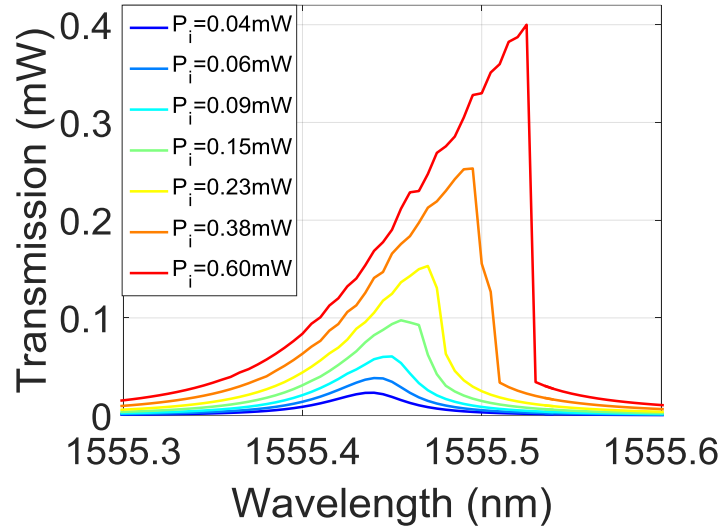
**Figure 5.4:** Simulated transmission spectra of a π-phase shifted grating as a function of injection power.

A schematic of the stabilization scheme is presented in Figure 5.5. The response of the resonator can be calculated, given its transfer function and a measurement of the input power, using the same model built for the simulations, stored in a microprocessor controller. In order to stabilize the device it is necessary to first manually set the device to the optimal working point and then to initiate the feedback control system. Once the relative position of the resonator and laser injection wavelength changes, due to all the effects described before, the system will generate an error signal dependent on the shift away from the previously set operating point and the spectral model. The error is then fed-back to the local thermal heating element to shift the position of the resonant line in order to align the system back to the optimum point.
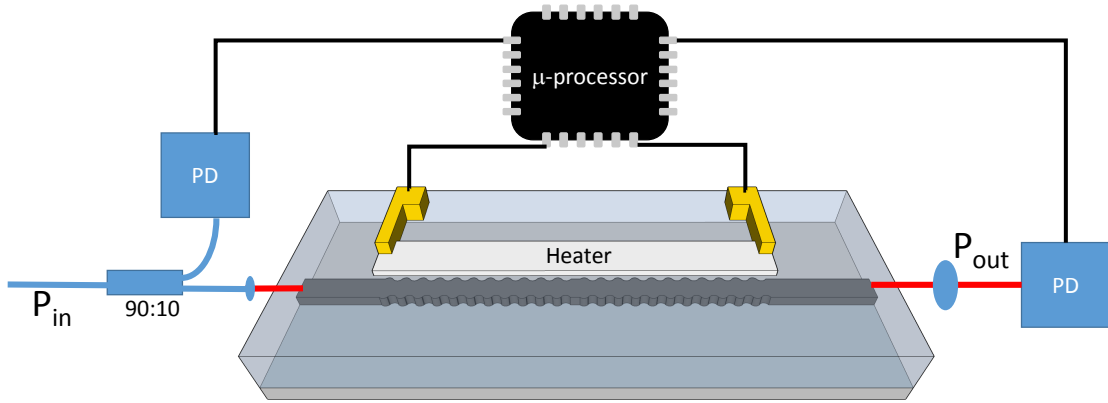
**Figure 5.5:** Schematic of the feedback control scheme for the micro-resonator device. The micro-processor stores the TMM model of the device and calculates an error signal based on the measured transmitted power and injection power, taking the on-resonance position as a working point.

The micro-processor that deals with the feedback control operations is obtained using an USB voltage control hardware operating on the probe channels and an Arduino UNO board. Arduino/Genuino Uno is a microcontroller board based on the ATmega328P [133]. It has 14 digital input/output pins (of which 6 can be used as PWM outputs), 6 analog inputs, a 16 MHz quartz crystal and a USB connection. A schematic of the micro-controller is shown in Figure 5.6
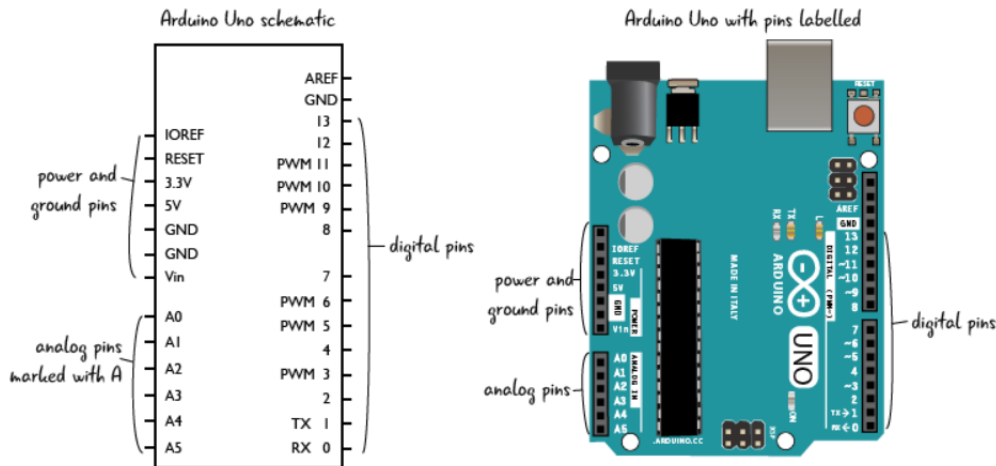


**Figure 5.6:** Schematic of the micro-controller in use showing all the analog and digital I/O available.

To operate the micro-controller it is only necessary to write the code that will then constantly run when the USB cable is connected. Arduino also supports Labview functioning

and in this work this capability is used. To run the feedback loop properly it is necessary to start from a stable and optimum condition. The maximum of bistability is manually reached controlling the laser wavelength and tuning the sample to a mid-point bias from where the system can be tuned back or forward independently. Once the optimum point is reached the micro-processor will, only for the first time from reset, read the output value from the oscilloscope and store it as a setpoint. After this stage the feedback loop will be in action, the micro-controller continuously read the output extinction value and compare it with the stored setpoint creating an error value from their difference. The generated error will then be sent to the LabView based software, whose front panel is shown in Figure 5.7, that, using the algorithm obtained from the cold cavity transfer function, will calculate and apply, on top of the constant bias, the necessary thermal tuning related to the amplitude and direction of the read error value.
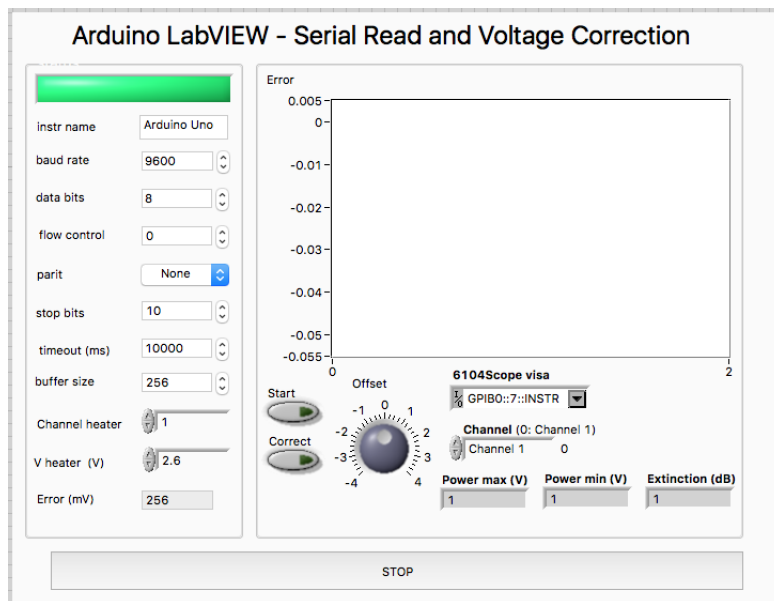


**Figure 5.7:** Main VI used during the feedback loop operations to read the error value and generate the related voltage change.

## 5.3 Results and Discussion

### 5.3.1 $\pi$-phase shifted grating response

The measured transmission spectrum of the $\pi-$phase shifted grating device is shown in Figure 5.8(a). In this case the spectrum is obtained using a low injection power to avoid non-linear effects. The injection power is referenced to the optical power in the access waveguide coupled to the resonator. The measured transmission power is instead related to the power in the post-resonator waveguide. The inset in Figure 5.8(a) shows an enlargement of the resonance mode, with a Q-factor of $\approx 40\,\mathrm{k}$.

To better understand the device functioning, NIR camera images of the light scattered vertically from the grating filter and access waveguides, where light is injected from the left hand side of the images, are shown in Figure 5.8(b). These images were taken before fabrication of the metal heater elements and show three important scenario in this device operations. (I) refers to the out of band transmission. The figure shows scattering along the waveguide length. (II) refers to the in-band rejection where little light transmitted from the input to the output waveguide is shown. Figure (III) represents instead the on-resonance transmission mode showing clear localization to the centre of the grating device.
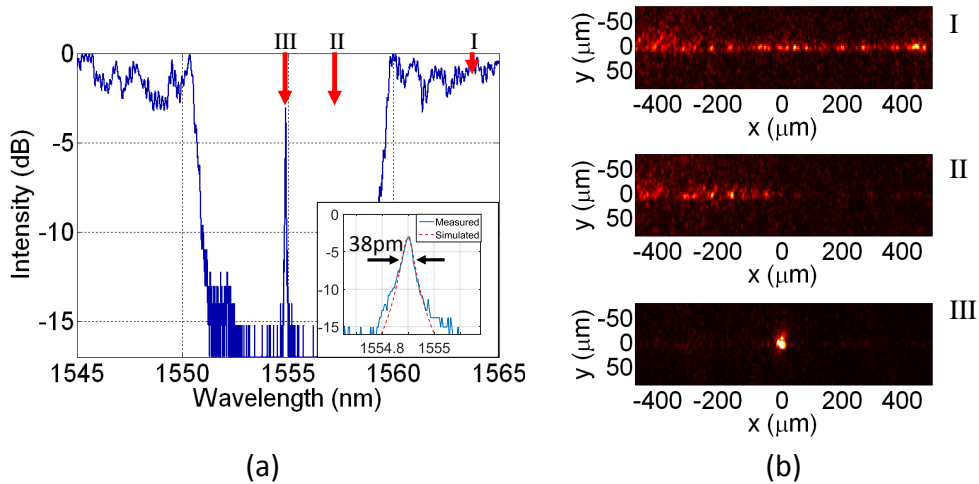


**Figure 5.8:** (a) Measured transmission spectrum of a $\pi-$phase shifted grating with a length of $\approx 200\mu m$. (b) NIR images of vertically scattered light from the grating and access waveguides, corresponding to spectral positions detailed in (a).

A plot of the measured transmission spectra of the device as a function of input power is presented in Figure 5.9(a), along with the simulated spectra from Figure 5.4. In this figure it is possible to notice the onset of the thermal non-linear behaviour, clear at around 0.09 mW of power on-chip. Figure 5.9(b) shows instead the tuning effect of the on-chip thermal heating element. It is possible to shift the device to longer wavelength by increasing the power dissipated on the heater. Even though the global spectrum is shifted, the device still retains the non-linear thermal resonance shift as a function of injected optical power.
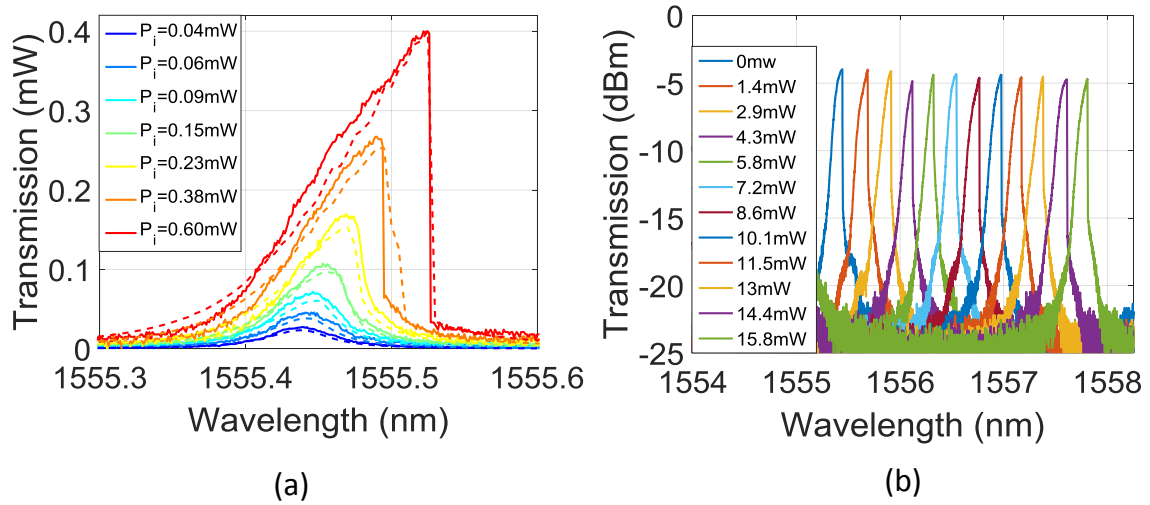


**Figure 5.9:** (a) Measured and simulated transmission spectra of the $\pi-$phase shifted grating as a function of on-chip injection power. Simulated curves are dashed lines, solid lines correspond to measured spectra. (b) Measured transmission spectra of the device at 0.6 mW injection power as a function of the power dissipated on the thermal heating element. (The y-axis is given in dBm in order to illustrate the asymmetric transmission spectra across the wide wavelength range.)

For the demonstration of the feedback loop stabilization system, the device is operated at its maximum resonance position for an injection power of 0.6 mW. In this work, the bistable switching of the cavity [124], was chosen to demonstrate that the device, using the developed system, remains in this optimal condition. When an injection wavelength, set to the optimal working point, is coupled through the resonator, it is possible to measure the device hysteresis curve, shown in Figure 5.10(a).

At point (1) the laser wavelength is on the red side of the resonance line and at a low value of transmission. Increasing the injection power to point (2) increases the power trapped in the resonator, and the resonance line is shifted to the red towards the injection wavelength setting

94

the device to the high transmission state. The trapped optical power maintains this high transmission state as a function of reducing power through point (3). At this point the power is insufficient to cause a red shift alignment of the resonant line with the injection wavelength and the resonator returns to point (4) where its cavity resonance line is blue detuned from the laser wavelength and the device is again in the low transmission state.
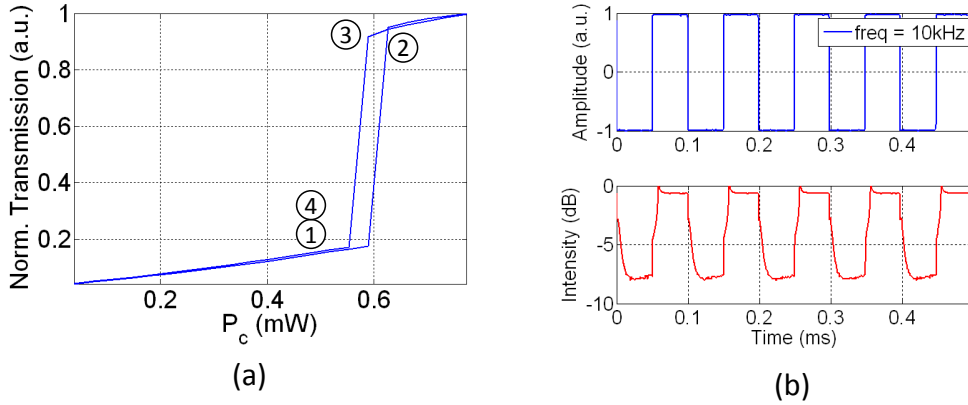


**Figure 5.10:** (a) Measured transmitted power of the grating device as a function of injected power showing hysteresis effects. The laser wavelength was set on the red side of the cold cavity resonance peak. (b) Input modulation signal and micro-resonator response for thermal bistability operation.

The bistable switching used to demonstrate the device operation was achieved by using a signal generator to apply a direct modulation to the tunable laser output power. The laser was set at an average power on-chip of $0.6\,\text{mW}$ with a modulation amplitude of $0.09\,\text{mW}$. The device is operated with an initial bias on the heater; this first shift allows both positive and negative detuning via the thermal heating element. All the results below were taken at an initial operating wavelength of $1556.980\,\text{nm}$. A square wave at $10\,\text{kHz}$ was used as a source, with the optical device temporal response shown in Figure 5.10(b). The extinction of the switching depends on the working point of the device with respect to the cavity resonance and the maximum obtained in this case is $\approx 7.5$ dB. From the extinction ratio value it is possible to obtain an estimate of the operating point of the system.

The measured bistable switching extinction ratio as a function of laser signal detuning from the optimal working point, is shown in Figure 5.11. When the wavelength is tuned from the blue side towards the cold cavity peak of the resonance the extinction increases (i). Once the injection wavelength approaches the peak of the resonance the device starts to exhibit

incomplete bistable switching. Increasing the extinction, a full switching is achieved and the optimal working point is approached (iii). When the wavelength moves too far to the red side of the resonance peak, the device is back into the low state (iv). A very important point to notice is that the detuning range of the optimal bistable region (shown in (iii)) is less than 7 pm. This value can be related to what said in the chapter introduction, in a Bragg grating device with a period of 318 nm and an effective index of 2.445, a change of 0.1 K can result in a resonance shift of over 10 pm. These clarify the necessity for device stabilization.
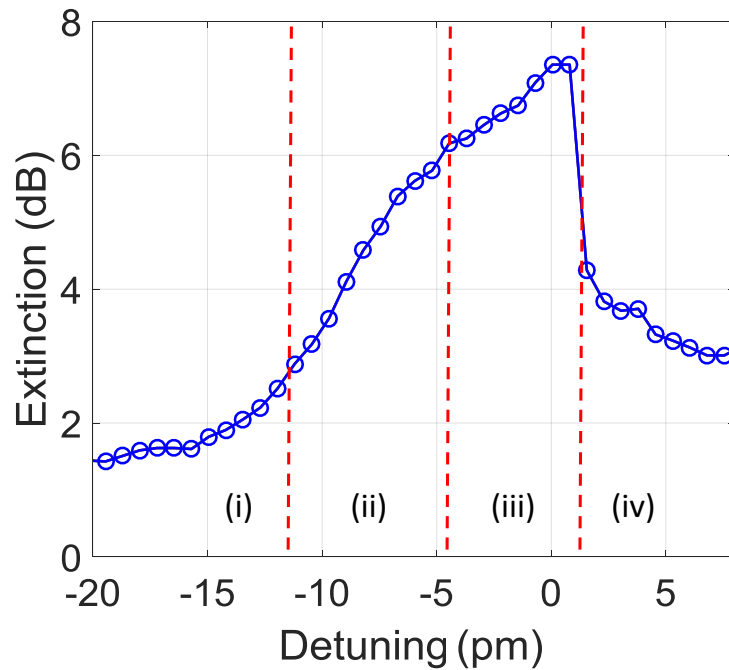


**Figure 5.11:** Measured extinction ratio of the device as a function of injection wavelength detuning from working point. (i) Injection on the blue side of the resonance, (ii) incomplete bistable switching, (iii) bistable switching, (iv) injection on the red side of the resonator past "switch off" point.

### 5.3.2 Cavity stabilization

First of all, the device was mounted on a Peltier control stage and the temperature of the laboratory environment was kept stable throughout the experiment. Nevertheless, when the device is not connected to the stabilisation setup, in a "free running" case, after the initialisation at its optimal working point, the lifetime of the operation, before a complete detuning, was in the order of minutes. A major improvement was observed when the feedback system was enabled. No drift in measured extinction ratio of the bistable switching was in

fact registered over an 8 hour period of operation. In order to confirm the performance of the stabilisation loop, the system was then forced by detuning the laser injection wavelength from the optimal working point in both positive and negative directions. The results of this experiment are shown in Figure 5.12. The figure shows the switching extinction ratio as a measure of operation in the bistable regime for laser detuning wavelength.
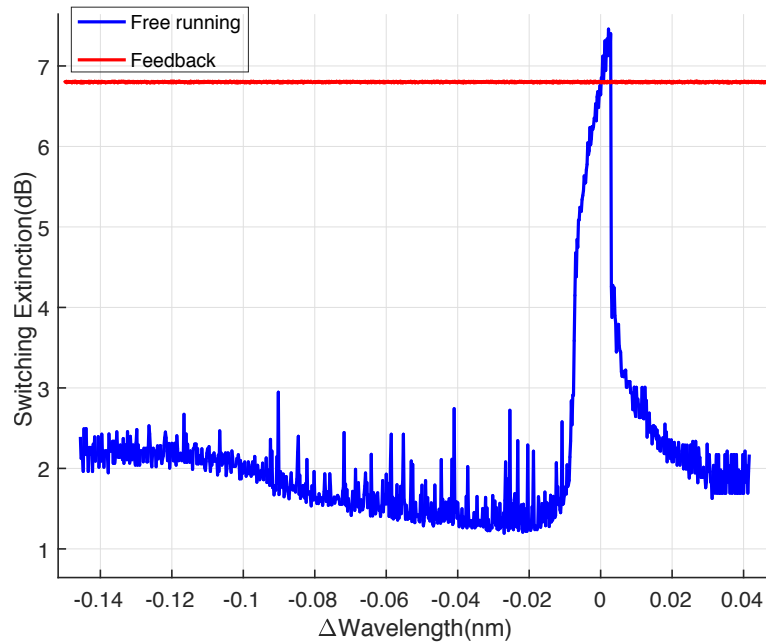


**Figure 5.12:** Measured switching extinction ratio as a function of laser detuning from the optimal "free running" bistable setpoint, detail.

The behaviour of the system is shown for both the "free running" case and the case where the feedback system has been implemented. When no feedback control is active, the bistable switching appears to be stable over only a few picometres of laser detuning. When the control loop is engaged the laser wavelength can be detuned over a 1.5 nm range without affecting the bistable switching operation, limited only by the resistive heater's operation range, as shown in Figure 5.13.
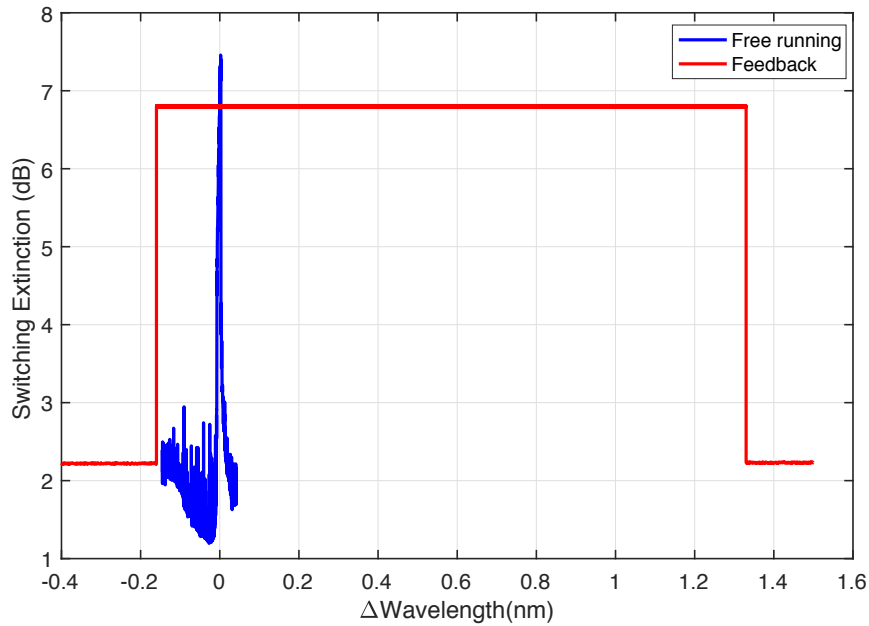
**Figure 5.13:** Measured switching extinction ratio as a function of laser detuning from the optimal free running bistable setpoint, total plot.

As a final experiment, the Peltier stage was used to vary the ambient thermal conditions of the device. The temperature values detailed in Figure 5.14 relate to measurements on the surface of the Peltier stage in contact with the silicon substrate of the device. The lab was kept at a constant temperature of $20\,^oC$ throughout the measurements.
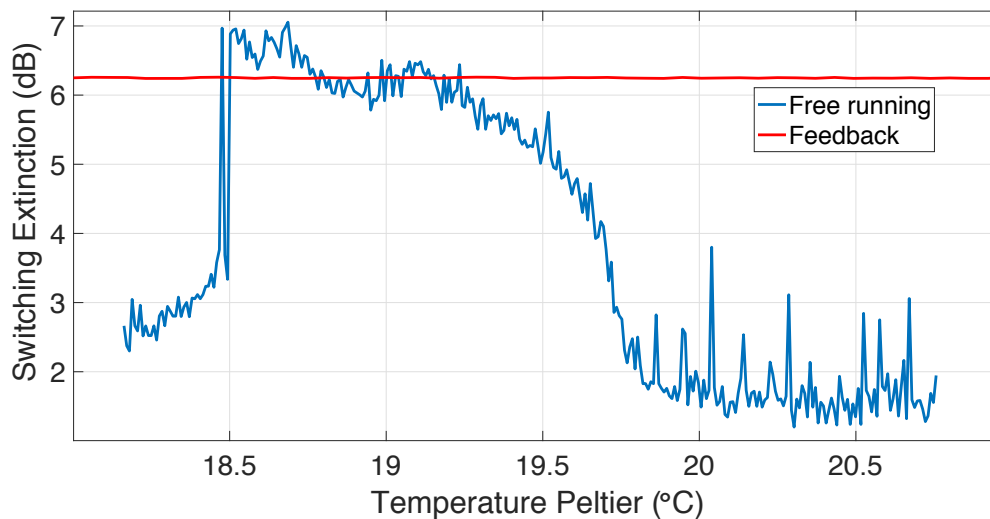


**Figure 5.14:** Measured switching extinction ratio as a function of temperature of the Peltier stage, detail.

Again, a comparison between the "free running" operations and the feedback loop controlled

system is given. As it is possible to see in Figure 5.15, in the "free running" case, a temperature variation of only $\approx 1\,^{o}$C is sufficient to detune the device while, using the feedback control, the system exhibits stable switching over a temperature range of $40\,^{o}$C, limited by the Peltier tuning range.
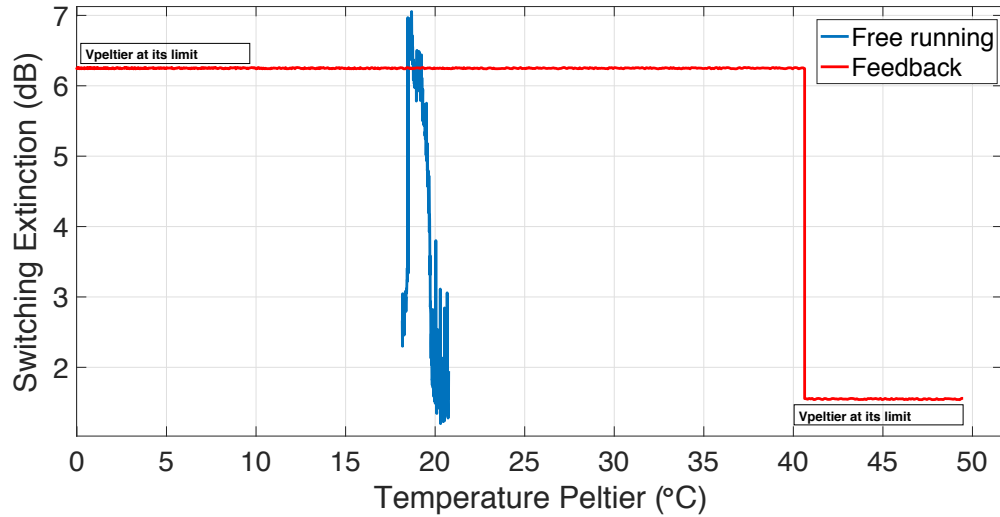


**Figure 5.15:** Measured switching extinction ratio as a function of temperature of the Peltier stage, total plot.

## 5.4 Conclusions

In this chapter, the stabilization of a high-Q micro-resonator operating in the non-linear regime was presented. In order to demonstrate the performance of the stabilisation feedback loop, a silicon $\pi$-phase shifted grating was fabricated incorporating a local resistive heater element for wavelength tuning of the resonance. Bistable switching of the device was demonstrated and a simple transmission function method using a microprocessor based feedback loop was detailed. Implementing a micro-processor based feedback loop the device improves its stability from a detuning range of a few picometres in injection wavelength or $1\,^{o}$C in ambient temperature to a laser detuning range of $1.5\,$nm and a temperature range of $40\,^{o}$C.

# Chapter 6

# Development of a direct writing laser lithography tool

The development of a novel and entirely custom-made laser photolitography system is demonstrated for rapid prototyping of PIC designs. This tool is designed to overcome the costs of the typical lithography systems and to drastically decrease the time for multiple micro-fabrications adding the chance of making all the necessary variations of a single pattern simply changing the software parameters. A full description of the hardware and the software created for this tool is presented together with the first results obtained on the fabrication and characterisation of the main PICs building blocks (waveguides, bends, Mach Zehnder interferometers and ring resonators), using SU-8 on $SiO_2$.

## 6.1  Maskless lithography

Performance of mask aligner lithography can be determined by two parameters: resolution and overlay. The first is defined to be the minimum feature size that can be transferred with high fidelity to a resist layer on a wafer. The overlay refers to the alignment accuracy of the patterns on successive masks overlaid with respect to previously defined patterns on the same wafer. Using mask aligner photolithography the resolution is limited by diffraction effects. The diffraction limit is defined as the minimum angular separation of two sources

that can be distinguished by an objective. This depends on the wavelength of the light being observed and the diameter of the objective itself. A way to overcome this limit is to use vacuum contact where the air in-between mask and wafer is evacuated. Using this technique it is possible to obtain submicron resolution but for vacuum contact lithography, very tight requirements regarding flatness and cleanliness apply. Any remaining particle will increase the mask-to-wafer distance and will deteriorate the printing results. The most common system is instead proximity lithography, a system that allows low costs and high throughput. In the mask aligner lithography system present in the Institute of Photonics cleanroom, the achievable resolution decreases with increasing proximity gap due to diffraction and the limit is fixed around 8 μm.

Another limitation on the use of mask aligner photo-lithography is that it is necessary to have a photomask for every pattern that needs to be fabricated. In a research project the cost of making a new photomask every time that fabrication changes are required, is unsustainable. The cost for a 4"sq mask can go over a few hundreds of dollars, it is therefore difficult for a research group to produce as many masks as may be necessary [134].

An alternative to the use of mask aligner lithography is electron beam lithography. Electron-beam lithography works scanning a focused beam of electrons in order to create an exposure pattern on the sample photoresist. Using e-beam lithography it is possible to beat the optical diffraction limit of the mask aligner lithography creating very small structures with nanometer features. The big drawback related to the use of the e-beam lithography is the cost. An e-beam writing system can be very expensive ($>$ US\$1M). This form of maskless lithography has also high resolution but low throughput, limiting its usage to photomask fabrication, low-volume production of semiconductor devices, and research and development. A solution to some of the problems presented before is represented by the use of a different photolithography technique, direct laser lithography, a mask-less photolithography that helps on cutting the cost of mask manufacturing and increases the achievable resolution down to submicron dimensions [54].

## 6.2 Direct laser lithography tool

Direct Laser Lithography (DLL) presented in this work is a custom made tool designed to overcome the costs of mask manufacturing without the need to buy an electron beam lithography setup that can cost several millions of dollars. Using the DLL tool the time for multiple micro-fabrications decreases drastically and it is possible to make all the necessary variations of a single pattern simply changing the software parameters. In this section the hardware development of this structure is presented. The hardware structure of the DLL tool is shown in Figure 6.1.
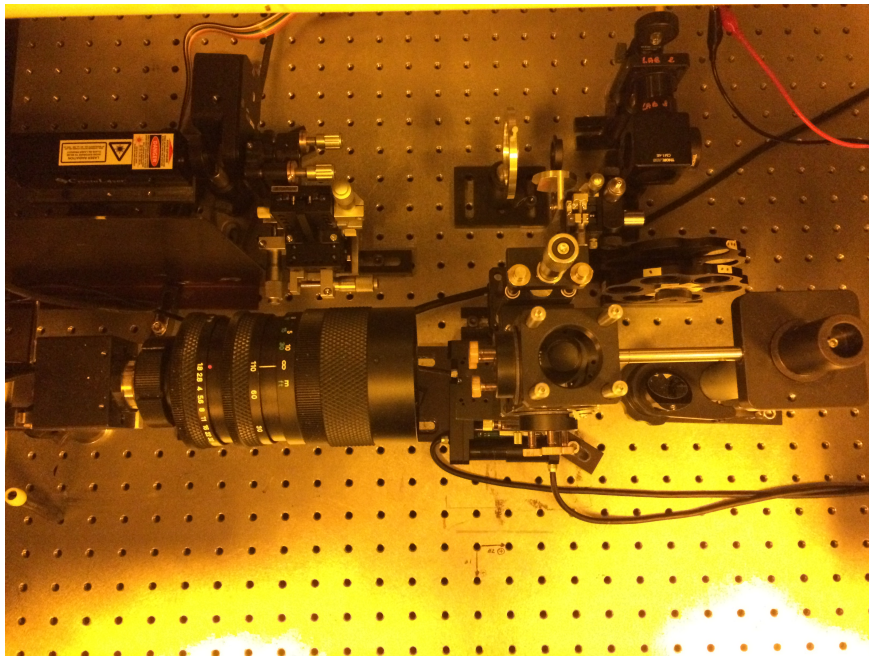


**Figure 6.1:** Direct laser lithography system mounted on a clean room optical table.

To better understand the functioning of this tool and the role of each component a schematic, describing the light path on a typical exposure process, is shown in Figure 6.2.
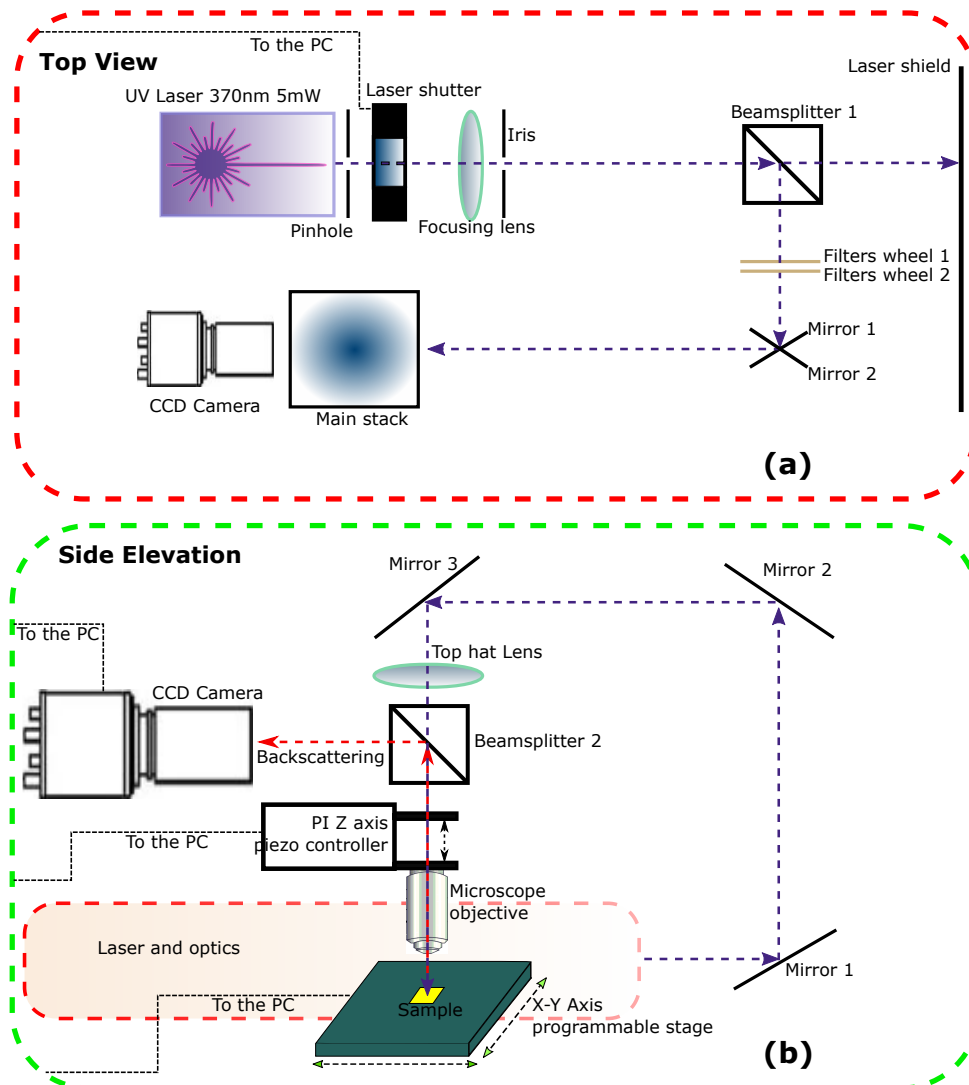
**Figure 6.2:** Direct laser lithography system schematic.

The light source is a high-reliability, high-stability, single-longitudinal-mode, circular beam UV laser produced by CrystaLaser [135]. Its wavelength is around 370 nm and the maximum power is around 5 mW. This laser has a beam divergence of 0.6 mrad and a beam diameter of 1 mm at $1/e^2$ [135]. The laser beam is then centered to an optical beam shutter. The SH05 Optical Beam Shutter, produced by Thorlabs, utilizes a rotary, electro-mechanical actuator to provide millisecond shutter operation. During operation, the shutter remains in a closed position and then opens when a pulse control signal is applied. The frequency at which the device is opened and closed can be controlled. This makes it ideal when it is necessary, as in this case, to avoid an unwanted region of the sample become exposed by the UV light.

In line with the beam path, after the shutter, a spatial filter is placed. This is an optical device which uses the principles of Fourier optics to alter the structure of a beam of light or other electromagnetic radiation, typically coherent laser light. In this case the filter is represented by an aperture placed in the beam that allows the desired light to pass, while blocking light that corresponds to undesired structure in the beam. This small circular aperture or "pinhole" passes only the central bright spot and removes nearly all fine structure from the beam, producing a smooth transverse intensity profile.

After the pinhole the light is collimated and guided through the path using a series free space optics components such as lenses and beamsplitter. Before directing the UV light onto the sample's surface the laser power can be reduced by a series of neutral density filters. The lenses' Optical Density (OD), is related to the light transmission, T, by the following equation:

$$OD = \log 10(1/\text{T}) \ ,$$
$$\text{T} = 10^{-\text{OD}} \ .$$

(6.1)

The filter in use can be dynamically changed during exposure because they are all mounted on a dual manual filter wheel. Each filter wheel is designed to accommodate six 1" diameter filters and can rotate independently. The first wheel mounts OD = [0.0 ; 0.2 ; 0.3 ; 0.4 ; 0.5 ; 0.6] allowing transmission of T = [100%; 63%; 50%; 40%; 32%; 25%] of the injected power. The second wheel mounts OD = [0.0 ; 1.0 ; 2.0 ; 3.0 ; 4.0 ; 5.0] allowing transmission of T = [100%;10%; 1%; 0.1%; 0.01%; 0.001%] of the injected power. Two filters on the two wheels can be combined in 36 different configurations all listed in Table 6.1.

| Transmission Fraction | | | | | | |
|---|---|---|---|---|---|---|
| Optical Density (OD) | 0.0 | 1.0 | 2.0 | 3.0 | 4.0 | 5.0 |
| 0.0 | 1 | 1e-1 | 1e-2 | 1e-3 | 1e-4 | 1e-5 |
| 0.2 | 6e-1 | 6e-2 | 6e-3 | 6e-4 | 6e-5 | 6e-6 |
| 0.3 | 5e-1 | 5e-2 | 5e-3 | 5e-4 | 5e-5 | 5e-6 |
| 0.4 | 4e-1 | 4e-2 | 4e-3 | 4e-4 | 4e-5 | 4e-6 |
| 0.5 | 3e-1 | 3e-2 | 3e-3 | 3e-4 | 3e-5 | 3e-6 |
| 0.6 | 2e-1 | 2e-2 | 2e-3 | 2e-4 | 2e-5 | 2e-6 |

**Table 6.1:** List of all the 36 possible combination of transmission percentage that is possible to obtain using the filter wheels.

As an example, if the first wheel is aligned on an OD = 0.2 and the second on an OD = 1.0 the total transmission will be given by:

$$T_{\text{output}} = (10^{-0.2})(10^{-1.0})T_{\text{incident}} \ . \tag{6.2}$$

therefore:

$$T_{output} = 0.06\%(T_{incident}) \ . \tag{6.3}$$

After the filter wheel the light is then guided by a series of mirrors on a vertical direction through the main part of the system shown in Figure 6.3 which follow the schematic in Figure 6.2(b).
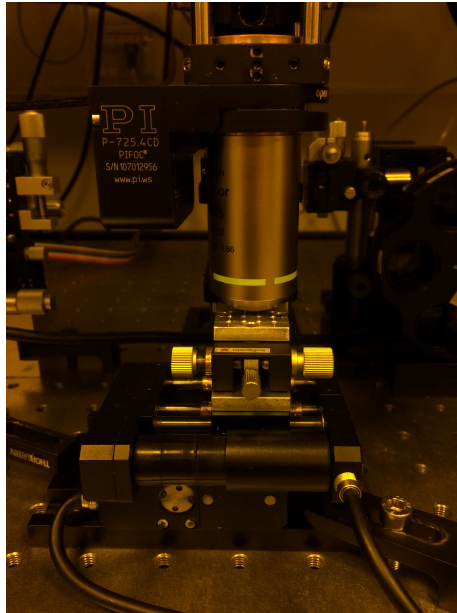
**Figure 6.3:** Main section of DLL tool containing directional mirrors, beamsplitter and a microscope objective that focuses the light on the sample placed in the x-y stage underneath.

The quality and the geometry of the beam is then modified by a top-hat beam shaping lens.



Without FBS shaper: diffraction limited Gaussian profile

With FBS shaper: near diffraction limited Top Hat profile
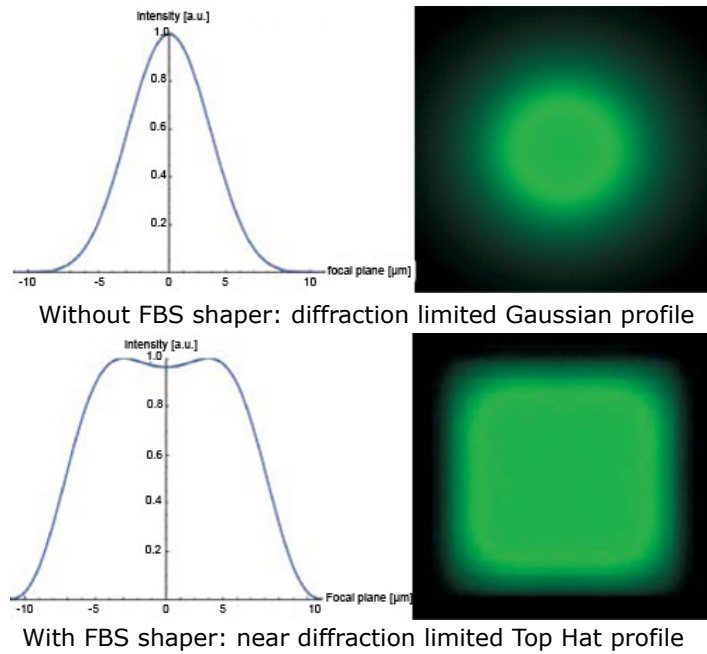
**Figure 6.4:** Comparison between laser beam output without (Top) or with (Bottom) Top Hat lens at focal plane. [136]

By introducing the top-hat beam shaper into the beam path in front of a lens/objective the initial diffraction limited Gaussian spot will be transformed into a homogeneous top-hat profile [136]. The main benefit on using a top hat shaping lens is in the uniform power density profile obtained after the beam shaping. The effect of this lens is shown in Figure 6.4 The smallest achievable Top-Hat size is $1.5\times$ the diffraction limited Gaussian-spot at $1/e^2$, the achievable Top Hat profiles can be either square or round, the choice of which lens to use relies on the type of features to fabricate. In this work both a square and a round top hat beam have been used. All the details and the reasons for these choices are explained in the following sections.

After the top hat beam the light is injected into a beamsplitter. The role of this component is to couple the light scattered from the sample's surface, to a Charge-Coupled Device (CCD) camera. The CCD camera allows operations on the imaged beam that will lead to beam autofocus and positioning. All these features are described in section 6.3. Through the use of a $10\times$ objective lens with numerical aperture of 0.75 the beam is then focused onto the surface of the sample. Both the objective lens and the sample are fixed to two different translational stages that can be programmed in order to follow the pattern configuration and maintain the laser beam focus. The Z translational stage where the objective lens is mounted is a P-725 produced by Physik Instrumente. It has a travel range of 460 µm and it is fully programmable through the use of a piezo-controller system that can be operated in either analogic or digital mode. The sample is positioned on a X-Y translational stage. This, as well as the one used for the microscope objective, is fully programmable with resolution of 500 nm. This stage can translate at variable speed and the X and Y direction are fully independent allowing simultaneous movement of both axes. A simple diagram to summarise the steps of a typical exposure process is shown in Figure 6.5.
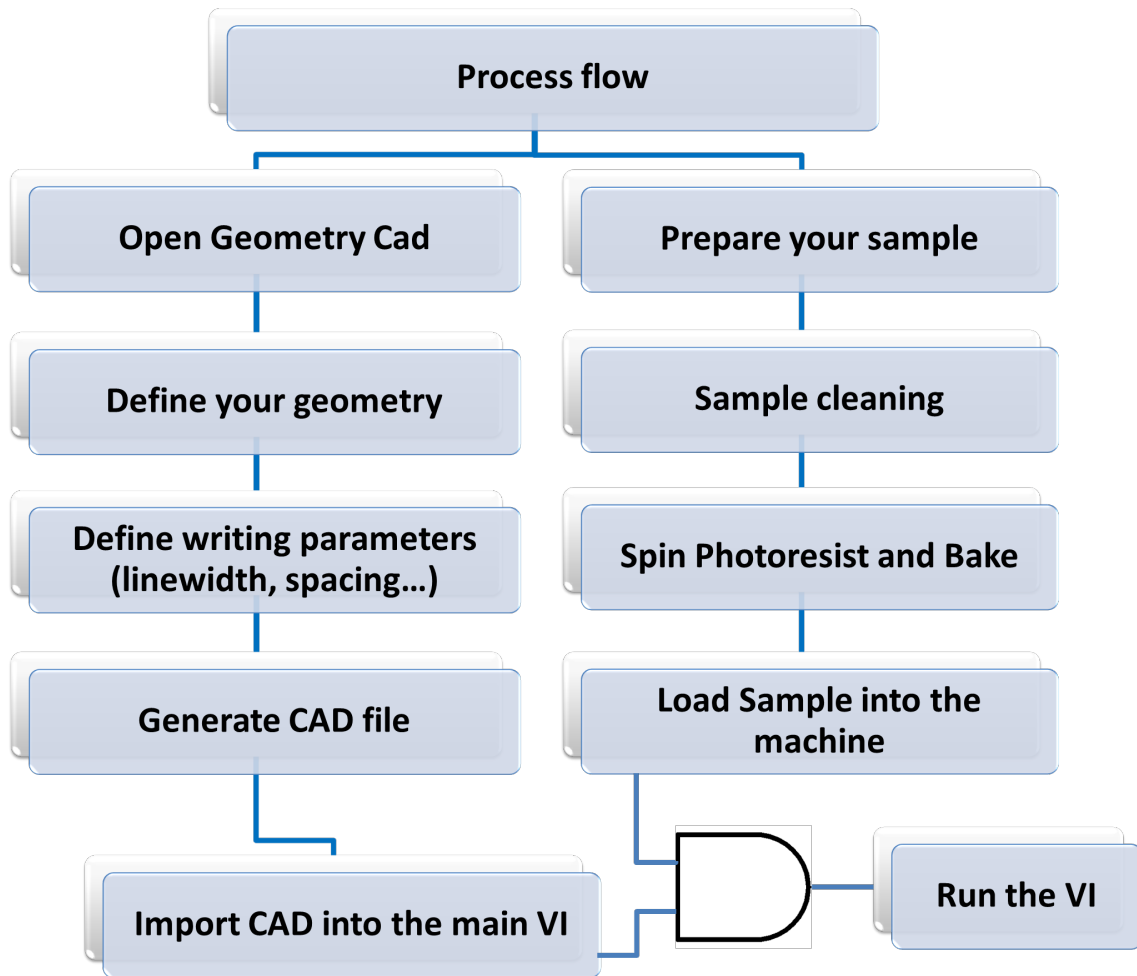
**Figure 6.5:** Diagram to summarise the steps of a typical exposure process

Details on the software operations of this system are provided in section 6.3.

## 6.3 Software design and operations

Two types of software are used to run the DLL tool before and during the exposure process. The first is Matlab based and is related to the pattern generation, while the second is LabView based and controls all the hardware functioning during the exposure process.

### 6.3.1 Matlab pattern generation

The way a laser lithography works is by the use of paths that need to be designed in advance. The first software to be programmed was therefore a geometry Computer-Aided Design (CAD) and is programmed using Matlab. The output of this software is a text file containing all the informations necessary to translate the desired patterns into movements for the x-y translational stage. The photoresist is selectively exposed moving the sample and maintaining the microscope objective in the same x-y position. Combining two main building blocks, lines and bends, it is possible to obtain every type of geometrical patterns. Using this tool it is therefore possible to create waveguides, Y-juctions, Mach-Zehnder interferometers, ring resonator and many more geometries. The DLL tool allows to expose, as well as defined patterns, also solid portions of the sample. All the details on the procedure to obtain this result are shown in section 6.3.4.
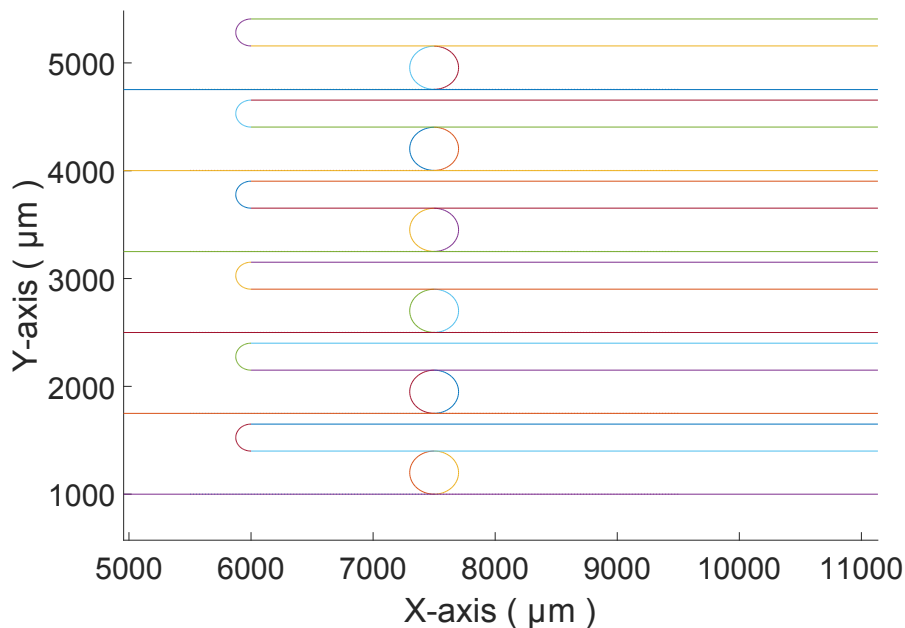


**Figure 6.6:** Example of mask patterns obtained using the Matlab CAD software. The different colors explain how the software sees the entire device as a junction of different building blocks (straight lines and bends).

A second output file allows to transfer the produced pattern to more complex CAD software like L-Edit to give the opportunity to produce the physical photomask if necessary. An example of the patterns that can be produced using this software is shown in Figure 6.6.

### 6.3.2 LabView pattern exposure

To run the exposure process the Matlab generated pattern is then transferred to the LabView software. This second software is installed on a PC dedicated to the DLL tool and is programmed in LabView. The main page of the software is shown in Figure 6.7.
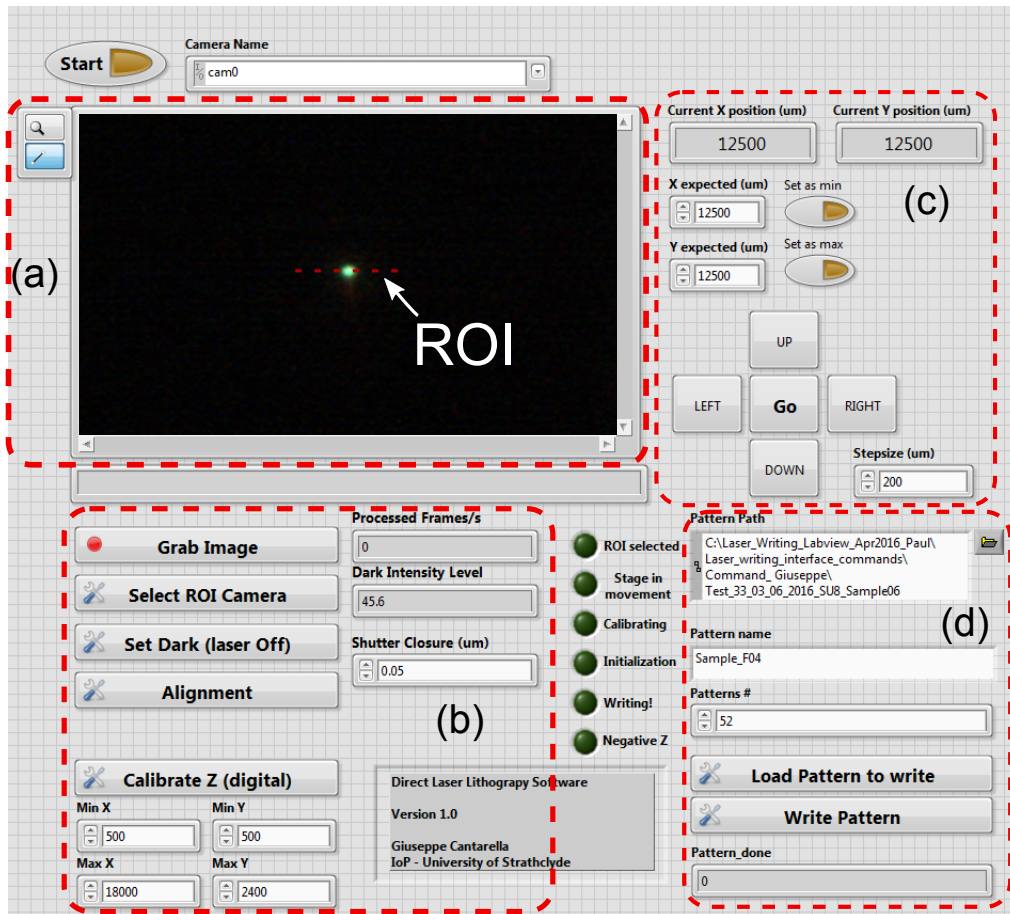


**Figure 6.7:** Screenshot of the main page of the LabView VI used to run the lithography process.

The software can be divided in different parts involved in different stages of the lithography process. Once the software has been started, an automatic realignment of all the components is executed and the X-Y stage is brought to the initial (0;0) position. Figure 6.7(a) shows the first interaction that the user has with the software. The screen shows the light that is backscattered from the sample's surface to the beamsplitter and therefore to the CCD camera. It is very important at this stage, in order to avoid unwanted exposure, that the sample is positioned in a way that the (0;0) point, where the beam is first directed, corresponds to a

part of the sample outside of the area to expose. Details on the first sample positioning are shown in Figure 6.8.
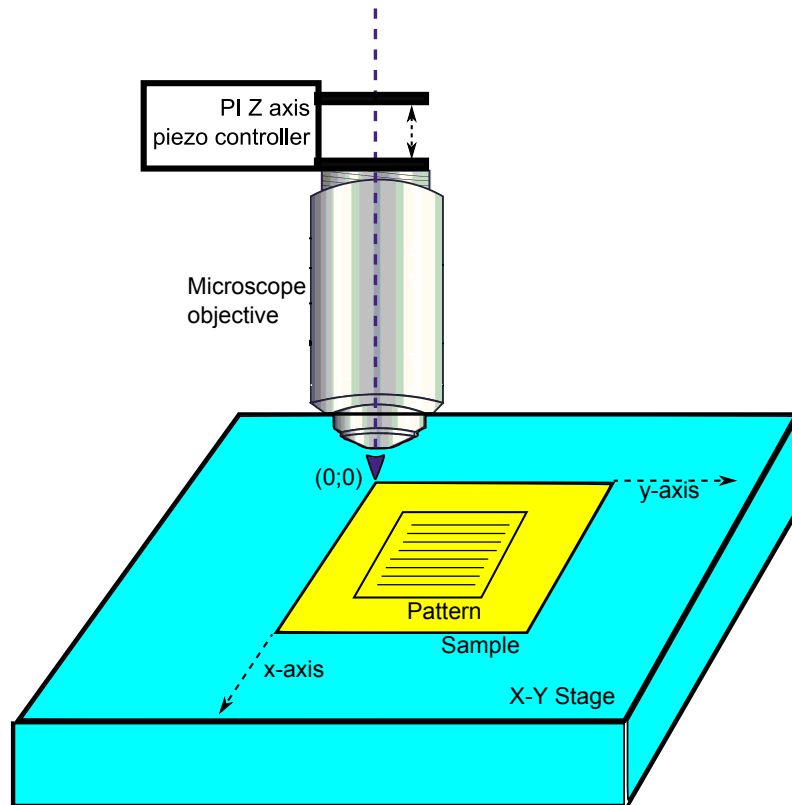
**Figure 6.8:** Example of a correct sample first positioning to avoid unwanted pattern exposure during the setup calibration.

The visualisation of the laser beam is necessary to run an autofocus algorithm. It is possible, during the lithography process, that the sample is positioned with a small tilt with respect to the plane of the stage. Because the DLL tool is a lithography system based on focused laser light, the presence of a surface not perfectly parallel to the stage, will change the correct focal distance at every point. Using the beam profile in the CCD camera it is therefore possible to calibrate the system creating a grid of the correct focal distances to stabilise the position of the objective lens throughout the full sample. The system will therefore check the beam intensity at every time of the exposure process and will change the height of the objective lens when necessary. The autofocus algorithm is described in Section 6.3.5. The software deals also with the initialisation of all the components and allows manual movement of the X-Y stage to a better sample positioning Figure 6.7(c). Details on the system calibration

and the autofocus algorithm are shown in Section 6.3.5.

Once the sample is positioned on the stage and the calibration is done successfully it is possible to operate with the last part of the software, shown in Figure 6.7(d). This portion of the software loads and transfers gradually the commands to the X-Y translational stage that will then follow the movement as stated in the layout created before. Once the last pattern has been exposed the system will automatically pause waiting for a new pattern to process.

Many components on this system have been calibrated and characterised in order to obtain a successful final result. Figure 6.9 shows a comparison between the first (Figure 6.9(a)) and the final (Figure 6.9(b)) pattern obtained using the laser lithography tool. From this comparison it is clear that a long troubleshooting phase has been carried out.



(a)         (b)
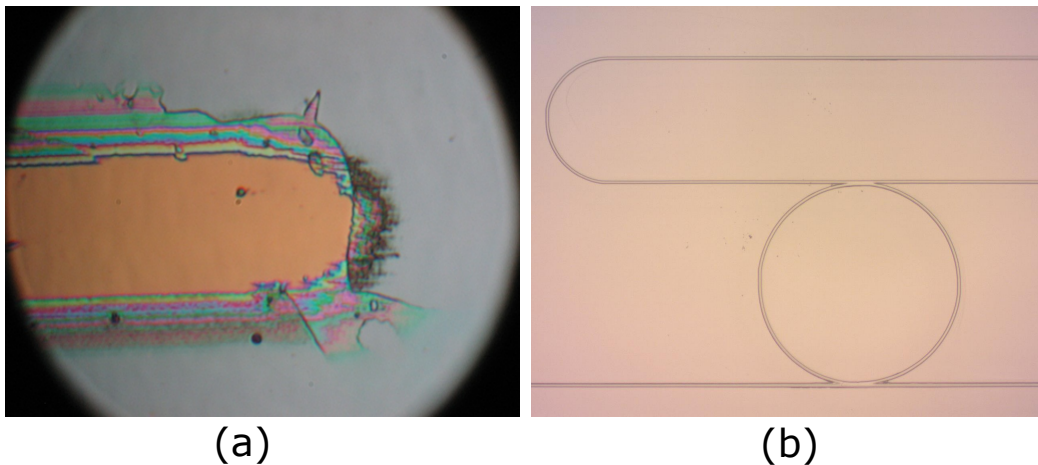
**Figure 6.9:** Comparison between the first and the last pattern obtained using the laser lithography tool.

Before presenting the results obtained using this tool it is therefore useful to describe and discuss, in Sections 6.3.3 and 6.3.4, all the problems encountered during the system characterisation and all the solution implemented to solve those problems.

### 6.3.3 Hardware troubleshooting

The problems encountered during the system characterisation can be divided in two categories, one related to the hardware and one to the bugs in the software. Focusing on the hardware, the first problem that was necessary to address was the level of cleanliness. In a lithography system

113

it is necessary to maintain all the components in a dust free environment. The system was therefore previously mounted and characterised for basic use and then, once the functioning of all the components has been ensured, the system was moved inside the clean room. The new location of the DLL tool solved the contamination issue completely.

**Vibrations and stability**

The second problem related to the hardware of the system is the alignment of all the components and their stability. As seen in the schematic in Figure 6.2, the DLL consists of an ensemble of components all correctely aligned to the beam path. This is a precision work that requires a high level of attention. First of all the components are placed in position and then bolted on the optical table for stability. Then the power of the laser beam is controlled all along the setup to ensure the minimum loss for each of the components. Some of the parts used are custom made (e.g. the sample holder); the production of a project and the use of a mechanical workshop was therefore required to produce these components. The most critical part in terms of alignment is the main stack, described in Figure 6.2(b). This part is obtain assembling all the optics with the use of cage mounts. The entire stack is then bolted into a manual translational stage used to position all the component to a correct starting point in height.

Once all the components are set in position and their stability has been checked, a first sample pattern was run and the results showed two stability issues that could only be addressed actually using the system. The two issues are described in Figure 6.10.
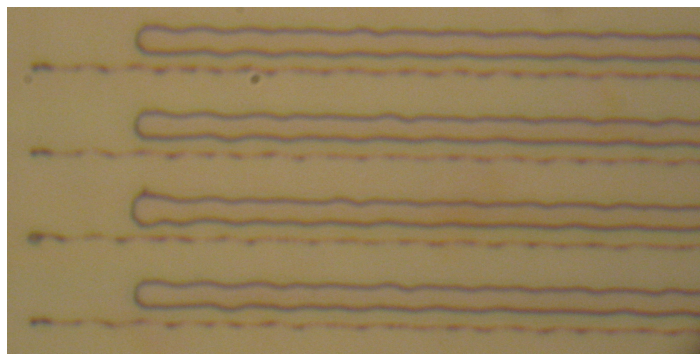


**Figure 6.10:** First test pattern made to characterise any stability problems in the system. It shows vibrational issues and the presence of a second beam path.

The first thing that is possible to notice on this path is that all the lines exposed present a vibrational issue ($\approx 500$ nm). It was identified that this problem is due to the system sensitivity on environmental low frequencies vibration. Any movement on the surrounding area during the exposure process leads to those unstable patterns. The solution to this problem was to float the entire optical table from its base. Using a series of air pipes and cantilevers it is possible to isolate the optical table from the environmental vibration. This solution is of common use in high sensitivity optical setup like this one. After this solution was applied all the patterns exhibited a more stable linear shape in which is not possible to see any features due to vibrations.

Another issue that can be spotted from Figure 6.10 is the presence of a second "ghost" pattern following the main structure. This is due to the fact that the light is focused on the sample using a series of optical components that can generate a back reflection that can be focused on the sample as a second, less powerful beam. The issue was found to be in the beamsplitter surface and alignment and, once the component has been changed and better aligned, the issue was solved.

### 6.3.4 Software optimisation

Once all the problems related to the hardware were addressed and solved it was necessary to fix all the possible bugs related to the software. The main VI used to run the exposure process, and shown in Figure 6.7, has a very complicated tree of dependencies. Every component is in fact made from other VIs and all of them are synchronised to work together and use each other's outputs as inputs, and vice versa. The first layer of VIs counts more than 100 different blocks and each of them is custom made using even more VIs. The entire VI hierarchy is a very complicated net of more than 300 custom made sub-blocks. Each of these has a key role on the functioning of the DLL tool and each of them is characterised and well installed in the system.

**Laser shutter control**

In this work only the main bugs will be addressed. The first issue is related to the laser shutter. This is one of the many components available to be programmed and controlled, as well as in manual mode, digitally using LabView. The problem related to the shutter is introduced using the results in Figure 6.11.
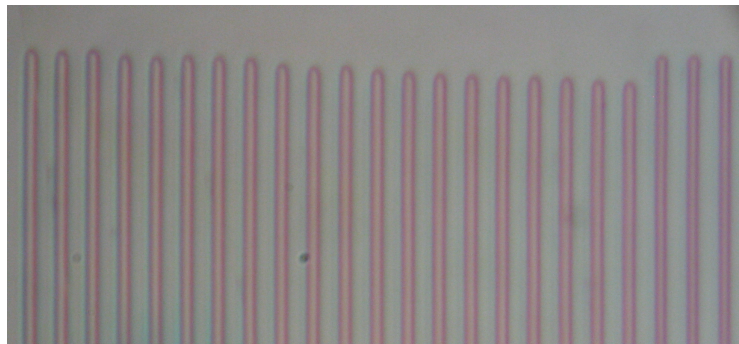


**Figure 6.11:** Problem on lines alignment due to a communication delay between the software and the laser shutter.

To better understand the nature of this bug it is necessary to consider an example of a simple exposure process. The first schematic in Figure 6.12 shows the main software flow once the VI starts the exposure process, the second schematic in Figure 6.13 gives then all the details on the actual sample exposure.
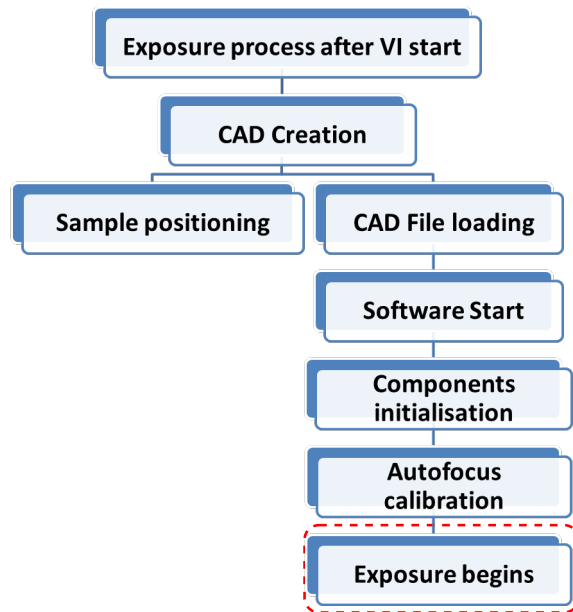
**Figure 6.12:** A schematic describing a simple exposure process after the VIs runs.
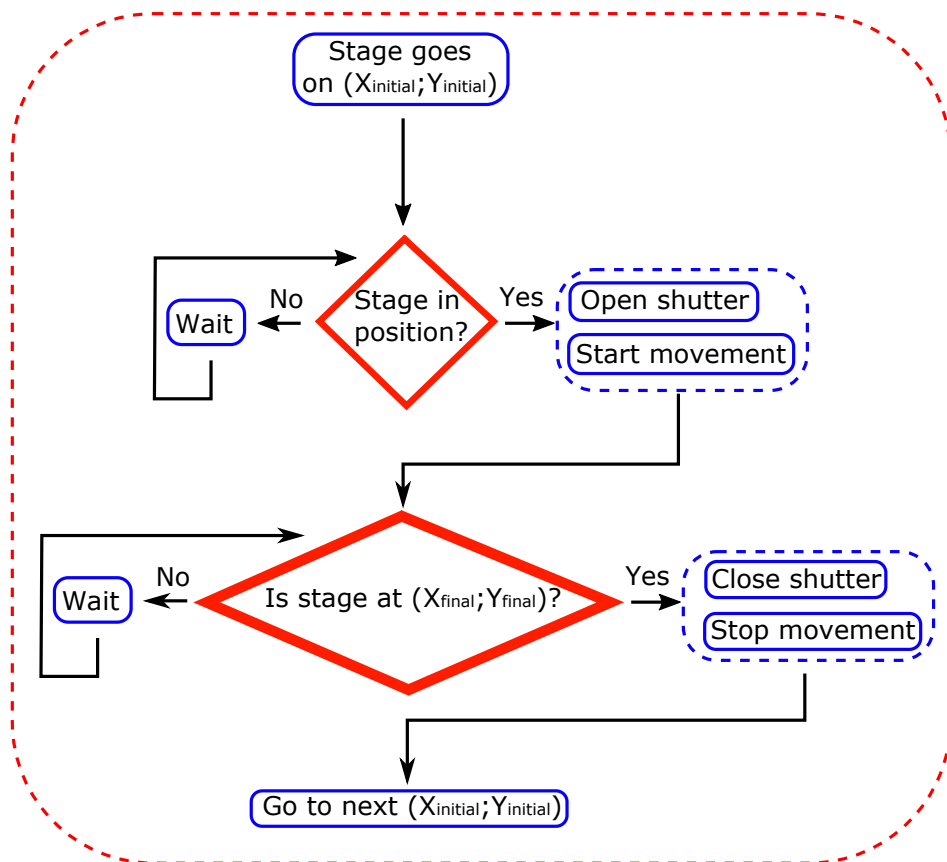


**Figure 6.13:** A schematic describing the software flow during sample exposure.

If e.g. the pattern consists on a simple straight waveguide only, a CAD file is first created. This file will contain all the coordinates necessary to the X-Y stage to reproduce the movement. These coordinates are the point by point X and Y position and the relative speed on each axis (both features will be explained in Section 6.4.1). Once the file is loaded into the software and the writing process starts, the stage will first move to what is indicated to be the starting point of the pattern and, once in position, the system will simultaneously start the movement and open the laser shutter to begin the exposure. In Figure 6.11 this example is shown using a set of lines exposed at different stage speed. It is clear from the image that a delay between the beginning of the movement and the shutter opening is present and is therefore related to the stage speed; the faster the stage goes, the bigger is the exposure delay presented. This problem needs to be fixed to obtain features where the actual start coordinates can be trusted and aligned with others. Unfortunately this delay can not be eliminated since the two components are already working at their maximum frequency. It therefore represents a bottle neck impossible to fix unless changing the CPU of both components to a faster one. An example of a distorted pattern cause by the second software bug is presented in Figure 6.14.
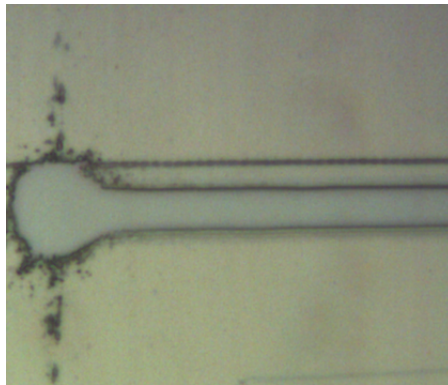


**Figure 6.14:** Over exposure due to a communication delay between the software and the laser shutter.

This time the bug is related to the end coordinates of a waveguide pattern. During the exposure process the software interacts dynamically with the system in many ways, some of them are related to the autofocus, as will be described in Section 6.3.5, but some others are related to the X-Y stage. The only way for the software to understand when the pattern reached the final coordinates is to instantly check the position of the X-Y stage point by

point during the writing process. The way this query takes place is time consuming and the speed of the response is dependent on the speed of the stage. Once the stage receives the "on-target" signal that communicates that the stage reached its final position the software sends a command to the shutter to close. From this description, also available in Figure 6.13, it is possible to understand how the big exposure spot present at the end of the waveguide in Figure 6.14 is again due to a delay of communication between the X-Y stage and the laser shutter which leaves the lasers on for enough time to induce an over exposure of the photoresist at the last coordinates of the pattern.

The solution found to fix both bugs has nothing to do with the software, it is instead a solution that comes from an understanding of the exposure process with the DLL tool. As it will be found in Section 6.4.1, the exposure dose that goes into the sample can be changed using the filter wheel on the setup or the speed of the X-Y stage, the faster the stage moves, the lower is the dose that exposes the sample. It is therefore possible, using a dosage test, fully described in Section 6.4.1, to find a combination of filter and stage speed that provide an energy dose not sufficient to expose the sample. Once these settings are found the solution is very straightforward. It is in fact necessary, in order to write a simple waveguide, only to add in the desired pattern a first and last "fast-lines" that will not be exposed, having the actual "correct-speed" pattern between them. Being both bugs related only to the reaction time of the software at the start and stop coordinates this solution will allows the software to open the shutter at some point in the first "fast-line" starting to expose the pattern at the right coordinate where the speed will decrease and the energy dose increase. To solve the end point problem it is only necessary to set as final coordinates not the very last point of the pattern but a point in the middle of the second "fast-line". This will allow the setup to close the shutter while writing the "fast-line" where a possible delay is not of interest. A schematic that makes this process more clear is shown in Figure 6.15
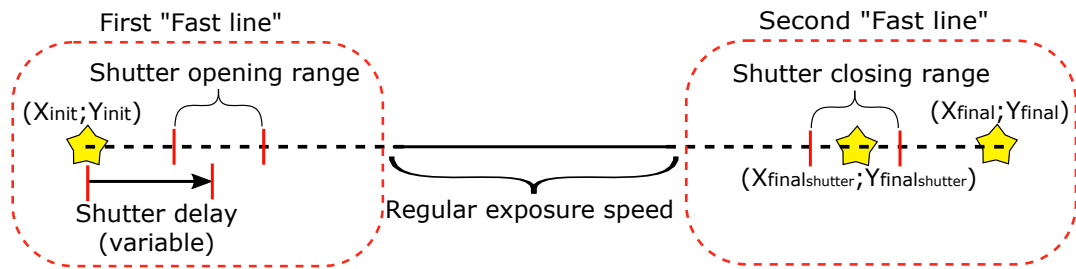
**Figure 6.15:** fast lines.

The main parameter to control in an exposure process is the energy dose to the sample. The 36 possible filter combinations have already been described in Section 6.2 but those are not the only way possible to adjust the exposure dose in the system. Due to the fact that it is possible to change the X-Y stage speed in order to change the energy dose to the sample, to find the optimum pattern linewidth, a system calibration is necessary. Section 6.4 will therefore deal with the system characterisation necessary before that a sample exposure can be operated.

### 6.3.5 Autofocus

As explained in Section 6.3.2 the DLL tool is a lithography system based on focused laser light and the presence of a tilt in the sample position will change the focal distance at every point. This is why an autofocus algorithm is necessary. To better understand the problem, an example of a pattern produced by an out of focus beam is provided in Figure 6.16.
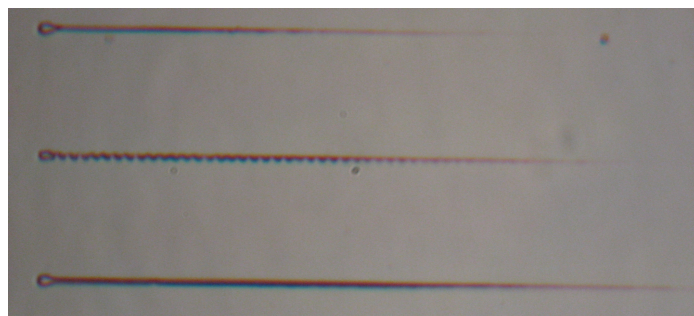


**Figure 6.16:** Some gradually under exposed patterns due to loss of focus on the laser beam. The first part of the third line shows the results of a writing process for a correct focal distance. The patterns visible in the other lines are due to the vibrational issue discussed before not yet solved when the autofocus issue was found.

As it is possible to see from Figure 6.16 the patterns gradually lose all their exposure due to a not-corrected focal point between the sample surface and the microscope objective that focuses the laser beam. The autofocus algorithm make use of the backscattered light coming from the sample surface and directed through a beamsplitter to the CCD camera. The assumption is that, taking as a Region Of Interest (ROI) an horizontal line of pixels passing through the center of the beam these will have their maximum of intensity when the beam is at its correct focal point.
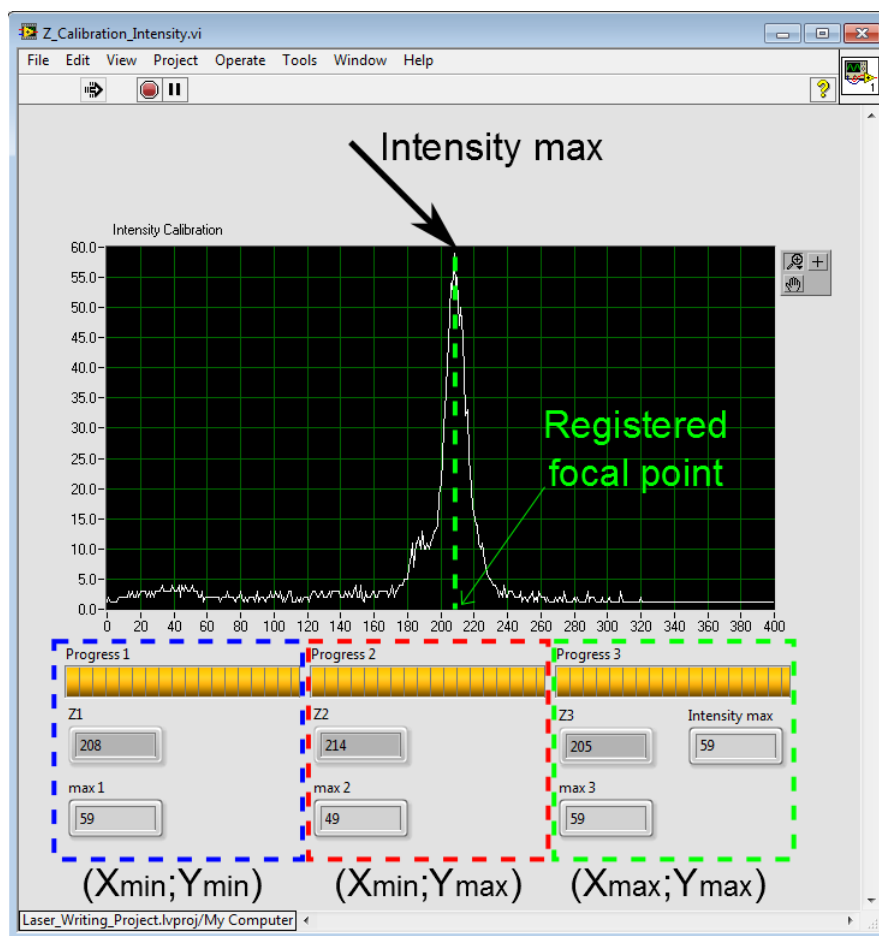


**Figure 6.17:** Example of the plot obtained in $(X_{min}; Y_{min})$ of pixels maximum intensity in function of the Z position.

The calibration take place once the sample is positioned and the maximum and minimum coordinates of the pattern to write are loaded into the software. Once the calibration runs the stage will move to $(X_{min}; Y_{min})$ and once in position the shutter will open. At this point the Z

translation stage will move the microscope objective of $\Delta Z = 400$ μm and the software will register the maximum of intensity for the ROI with a 1 μm resolution. These values will then be plotted, as shown in Figure 6.17 and the Z position relative to the maximum of intensity will be registered. The same operation will then be performed in other two corner points $(X_{min}; Y_{max})$ and $(X_{max}; Y_{max})$. Using this three point calibration it is therefore possible to calibrate the system creating a grid of the correct focal distances to stabilise the position of the objective lens throughout the full sample. The system will therefore check the beam intensity at every time of the exposure process and will change the height of the objective lens when necessary.

## 6.4 System Characterisation

The exposure dose and wavelength required to achieve the desired properties changes with the photoresist. Different photoresists exhibit different sensitivities to different wavelengths. The dose will also vary with resist thickness. Chosing the correct dose is very important since many effects like edge scattering or diffraction can drastically change the exposure results. If an image is overexposed for example, the photoresist image results eroded along the edges for positive photoresist or dilated if the photoresist used is negative. In case of underexposure instead, the pattern is not fully transferred and could results undefined. Some example of the three possible phases of exposure are shown in Figure 6.18.
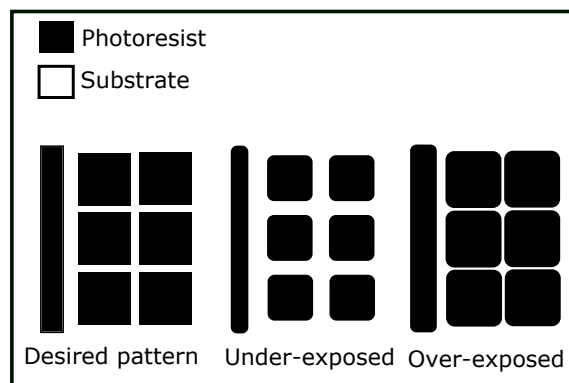


**Figure 6.18:** Comparison between possible exposure output depending on the UV energy dose on the sample.

### 6.4.1 Dosage test

In the case of a mask aligner tool it is possible to simply change the time of the exposure and the gap between the mask and the sample in order to achieve the optimum dose. Using the DLL tool the process is slightly different. The UV laser in use emits light with a maximum power output of 5 mW. This power is reduced by the pinhole and the free space optics down to a level of around 1 mW. It is then possible to reduce this maximum power level to lower values changing two different parameters, the filter value on the filter wheel and the speed of the X-Y stage during the exposure. As explained before, the filter wheel allows 36 different configurations and the total intensity output follows Eq. 4.1.

The X-Y stage can move from a minimum speed of 50 μm/s up to a speed of 1600 μm/s. Combining these two effects together it is possible to change the exposure dose on the sample and consequently the width of the desired exposure patterns. It is therefore necessary to choice the correct filter-speed pair necessary to obtain the desired exposure. To do so it is good practice to run a "dosage test" every time a new material or a new photoresist is introduced into the DLL tool.
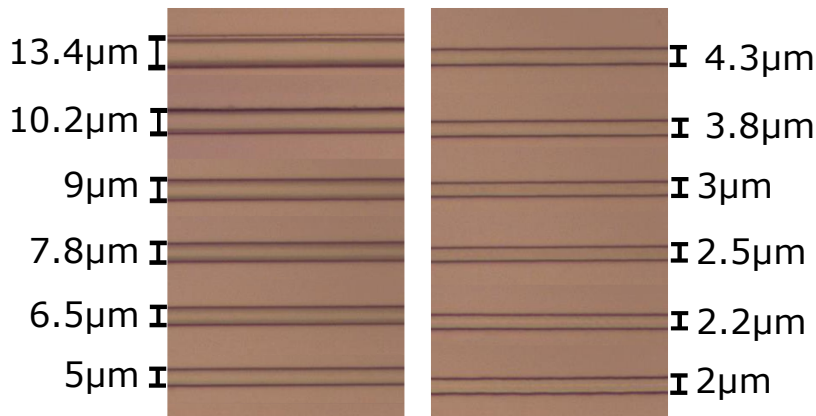


**Figure 6.19:** Example of some characterisation lines obtained in a typical dosage test to study the linewidth of waveguides in function of the exposure dose. The different width of the lines was obtained fixing the filter wheel to a value of 1.0 and varying the stage speed from 100 μm/s to 1200 μm/s.

A dosage test consists on a series of straight lines written with an increasing speed using increasing filter order. Using this test it is possible to scan all the available combinations in

order to find the right one to use. Analysing the results allows the user to obtain the correct linewidth every time that particular material and resist is used. An example of a dosage test result is shown in Figure 6.19. After a correct dosage test the user can run the DLL tool using optimal parameters for the pattern to be written.

## 6.5 Devices Fabrication

In order to show the full system calibration some examples of photonic integrated polymer devices have been fabricated. The results show that using the DLL tool it is possible to obtain high quality optical devices on a custom built setup. In order to demonstrate the versatility of DLL for fabrication of PICs, a range of test devices were characterised, including ring resonators, Y-junctions and Mach Zehnder interferometer.

The first devices fabricated using the DLL tool were straight waveguides. They were made using a simple microscope cover slip $SiO_2$ substrate, which has a refractive index of $n_{SiO_2} = 1.52$ at 1550 nm as a cladding and a polymer negative photoresist (SU-8) as a core material ($n_{SU-8} = 1.55$ at 1550 nm). At this stage the objective was to create a tool capable of improving or at least replicating the performance of the mask aligner tool in use in our cleanroom.

### 6.5.1 Fabrication of waveguides

Before running the exposure process it is necessary, in order to make single mode waveguides, to run mode solving software to obtain the correct waveguide width and height to use. A simulation was obtained using a Matlab code varying the width of the core at a fixed height at a wavelength of 1550 nm. This function calculates the modes of a dielectric waveguide using the semivectorial finite difference method. Using this function it is possible to determine all the field components of both TE and TM mode propagation. The full version of the algorithm used in this mode solver is described in [137]. A schematic of the waveguide simulated is shown in Figure 6.20.
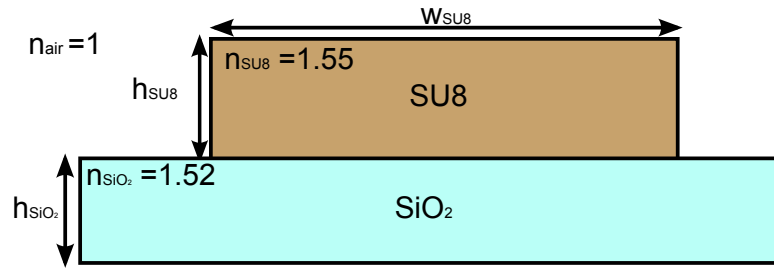
**Figure 6.20:** Schematic of the simulated and fabricated single mode waveguide.

The height and width values for the SU8 core are fixed at $h_{SU8} = 3.8$ μm and $w_{SU8} = 5$ μm respectively. The height of the $SiO_2$ under cladding is considered to be much higher than the core ($h_{SiO_2} > 100$ μm. The refractive index are considered to be $n_{SU8} = 1.55$ and $n_{SiO_2} = 1.52$ respectively. These are extracted results of the simulation shown in Figure 6.21 and Figure 6.22.
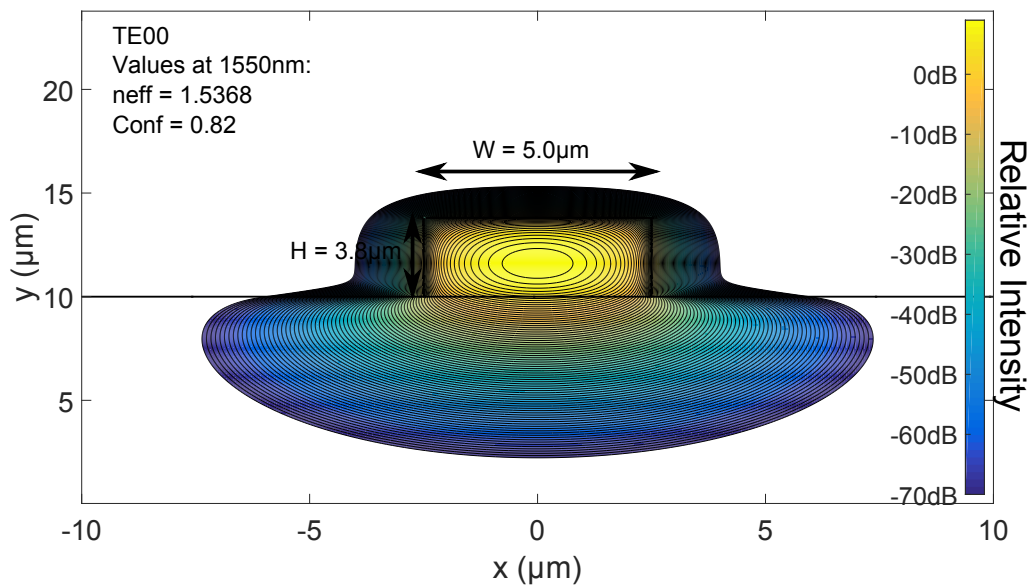


**Figure 6.21:** Mode propagation simulation for SU-8 waveguides with 3.8 μm height and 5 μm width for $TE_{00}$ mode.
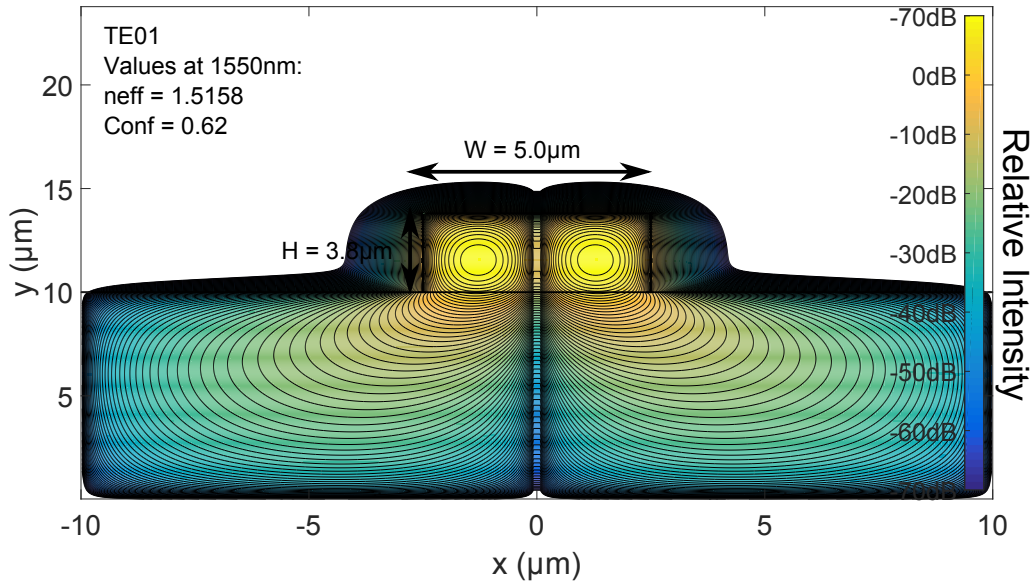
**Figure 6.22:** Mode propagation simulation for SU-8 waveguides with 3.8 μm height and 5 μm width for $TE_{01}$ mode.

Two values that it is possible to extract from these simulations are the effective refractive index, discussed in the chapter introduction, and the confinament factor. This latter value represents the ratio between the total intensity of the propagating mode and the mode intensity confined in the waveguide's core. This values have been obtained for $TE_{00}$, $TE_{01}$, $TM_{00}$ and $TM_{01}$ guided modes. The results are shown in 6.2 together with the related effective refractive index calculated at 1550 nm.

| Propagating mode | Confinement factor | Effectice index $n_{eff}$ |
|---|---|---|
| $TE_{00}$ | 0.82 | 1.537 |
| $TE_{01}$ | 0.62 | 1.516 |
| $TM_{00}$ | 0.71 | 1.521 |
| $TM_{01}$ | 0.51 | 1.515 |

**Table 6.2:** Confinement factor and effective index values obtained for all the possible 4 propagating mode in an SU-8 waveguides with width = 5 μm and height = 3.8 μm at 1550 nm.

It is possible, using the effective index and confinement factor values to extrapolate the boundary condition for single mode propagation in a waveguide.

126
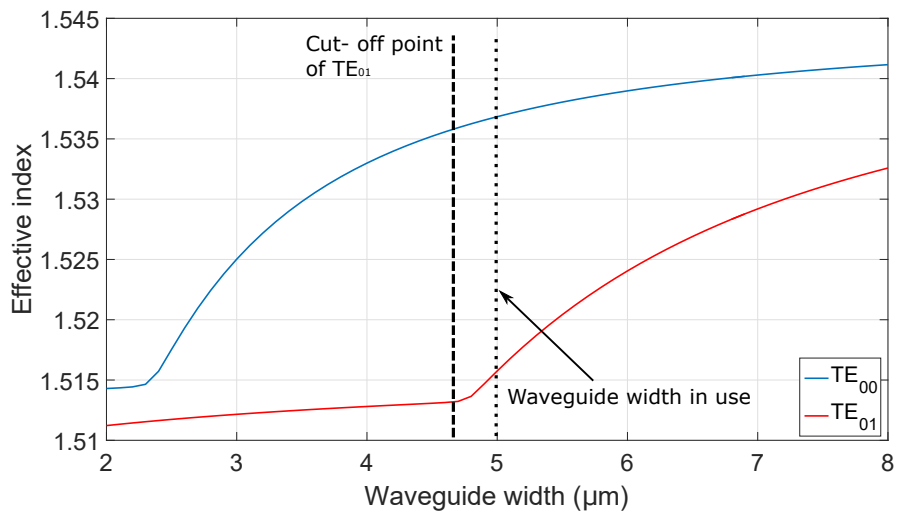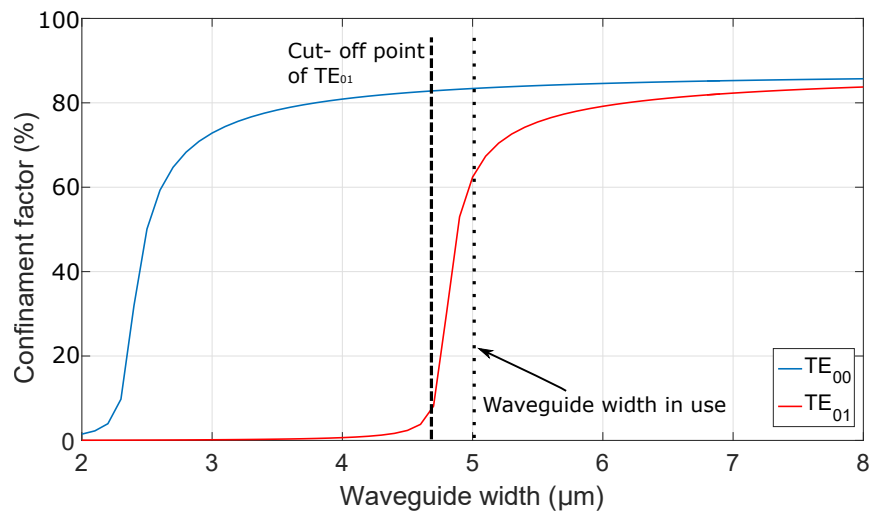
**Figure 6.23:** Effective refractive index (a) and confinement factor (b) variation as a function of waveguide width for a fixed height of 3.8 μm. The cut off point is shown to be around 4.7 μm.

Figure 6.23 shows the results of the simulations of effective refractive index, Figure 6.23(a), and confinement factor Figure 6.23(b), as a function of waveguide width for a fixed height = 3.8 μm. In both plots the calculated values that refer to the first order mode rapidly increase past the 4.7 μm width for the waveguide. That point represents the cut-off point for the first order mode. In our case, even if the dimensions are slightly above the cut-off point, the single mode condition is still ensured due to the high confinement for the fundamental mode and the high losses values for the first order propagation. Choosing the correct settings it is therefore possible, using the DLL tool to obtain single mode waveguides on SU-8 on $SiO_2$. An example of the obtained devices is shown in Figure 6.24
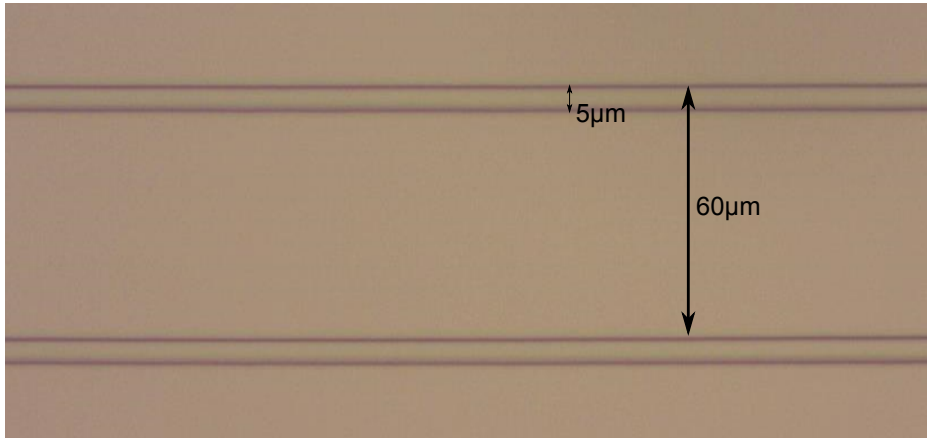


**Figure 6.24:** Example of waveguides obtained using the DLL tool.

Starting from this building block component it is possible to obtain more complex structures. Curved waveguides for example allow the fabrication of structures like splitters or combiners, Mach Zehnder Interferometers or ring resonators. But before to do so it is necessary to test the obtained waveguides and characterise their transmission loss. After the fabrication the sample was therefore cleaved in both facets to allow light coupling from lensed fibers. An example of a cleaved facet waveguide is shown in Figure 6.25.
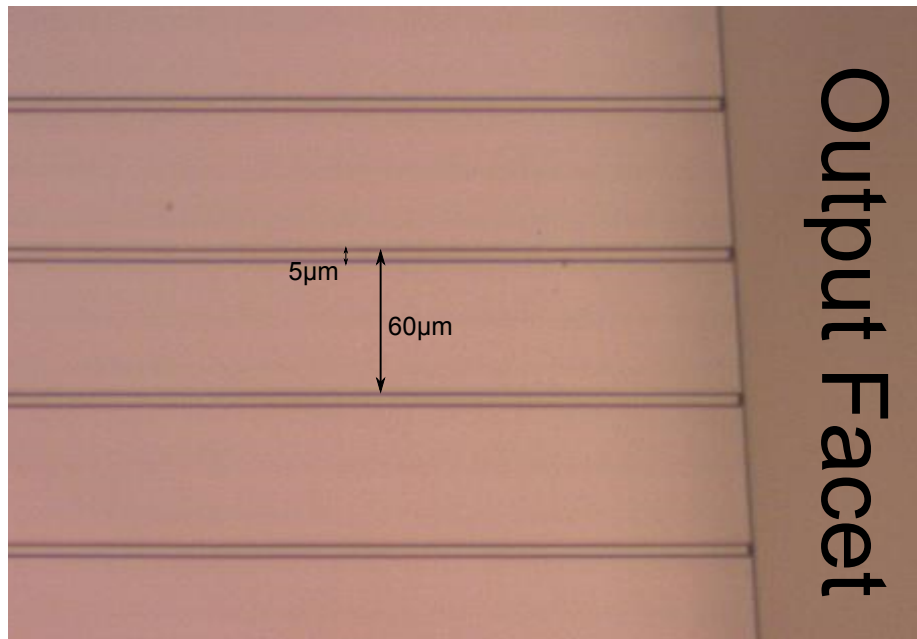
**Figure 6.25:** Picture of one of the facets of a series of cleaved waveguides fabricated with the DLL tool.

Cleaving $SiO_2$ manually is a very delicate process and involves the use of a diamond pen to scratch the surface and create a plane break to snap off the excess material. The first step on a cleaving procedure is to spincoat a protective layer of high thickness photoresist (e.g. MICROPOSIT S1818 SERIES positive photoresist), that will allow to make gentle pressure on the material without affecting the fabricated patterns. The second phase is to position a ruler, with some dust free paper underneath, on the sample surface covering everything but the portion to cleave. After that it will be possible to make some scratches on the opposite sides of the portion to cleave using the diamond pen and following the line of the ruler. The diamond pen marks do not have to scratch the actual sample but only its edges. Once two clear marks are made the sample is placed in a raised position by the use of an aluminium stage aligning the stage edge with the marks on the sample, leaving the region to cleave floating. A this point is only necessary to apply a gentle pressure on the side to cleave maintaining the rest of the sample firm in position. If the marks are well done a gentle pressure will be enough to snap the material with a line that will connect the two marks. Once cleaved the waveguides are then tested for transmission measurements using the optical setup described in Figure 6.26.
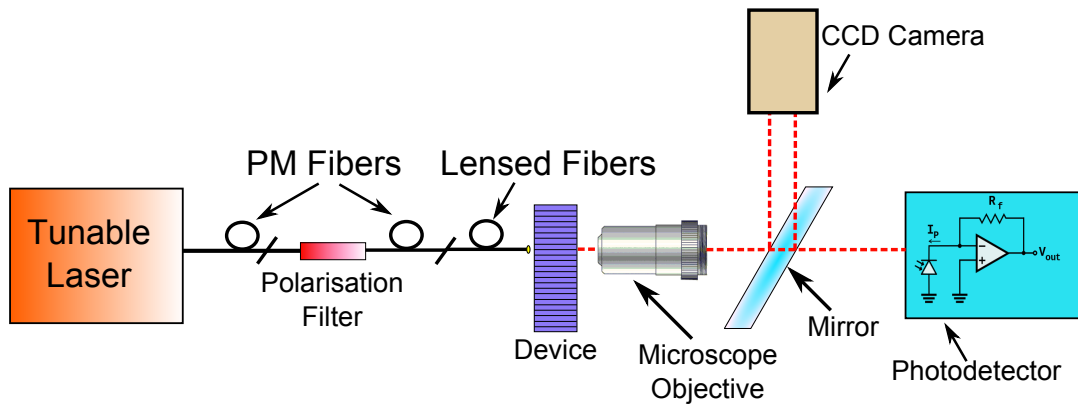
**Figure 6.26:** Schematic of the experimental setup used for the transmission measurements.

The transmission spectra of the filters were measured by coupling light, using PM fibre, from a tunable laser through a polarisation filter with an extinction ratio of 20 dB aligned with the TE mode to a PM lensed fibre and into the input polymer waveguide. The output light was coupled into a long working distance microscope objective and focused in a photodetector made of a transimpedance amplifier with variable gain. It is possible to visualise the output beam using a CCD camera.
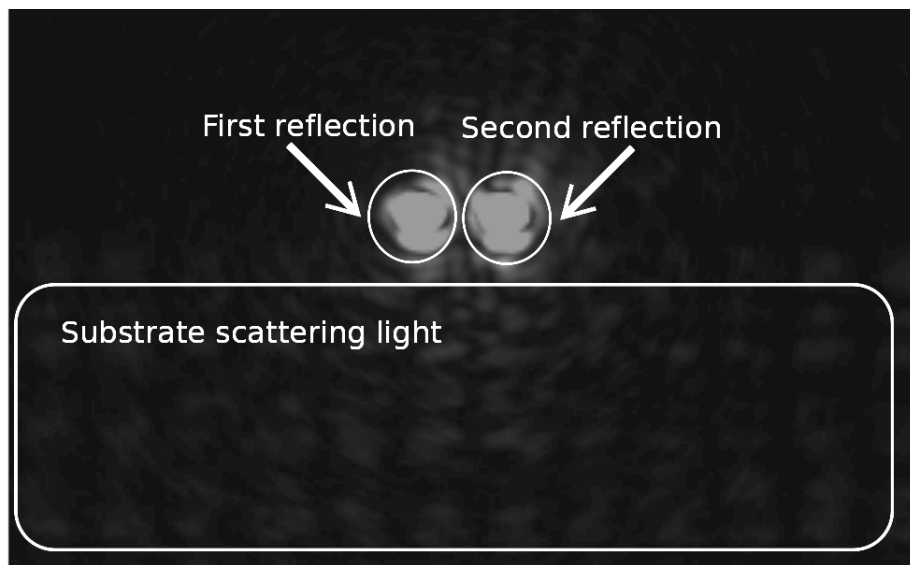


**Figure 6.27:** CCD Camera image of a single mode output obtained using the experimental setup shown in Figure 6.26.

The light is directed to the camera using a microscope slide as a mirror. The light that the CCD camera will capture is related to the two reflections from the two sides of the mirror.

A single mode beam will therefore be seen as two spots in the image. An example of a single mode waveguide output obtained using the CCD camera is shown in Figure 6.27 . An overview of the transmission measurements of the fabricated SU-8 straight waveguides is shown in Figure 6.28. These three waveguides are nominally identical. The setup loss during this measurements is calculated to be around 4 dB, this value has been subtracted from all the measurements shown in this work.
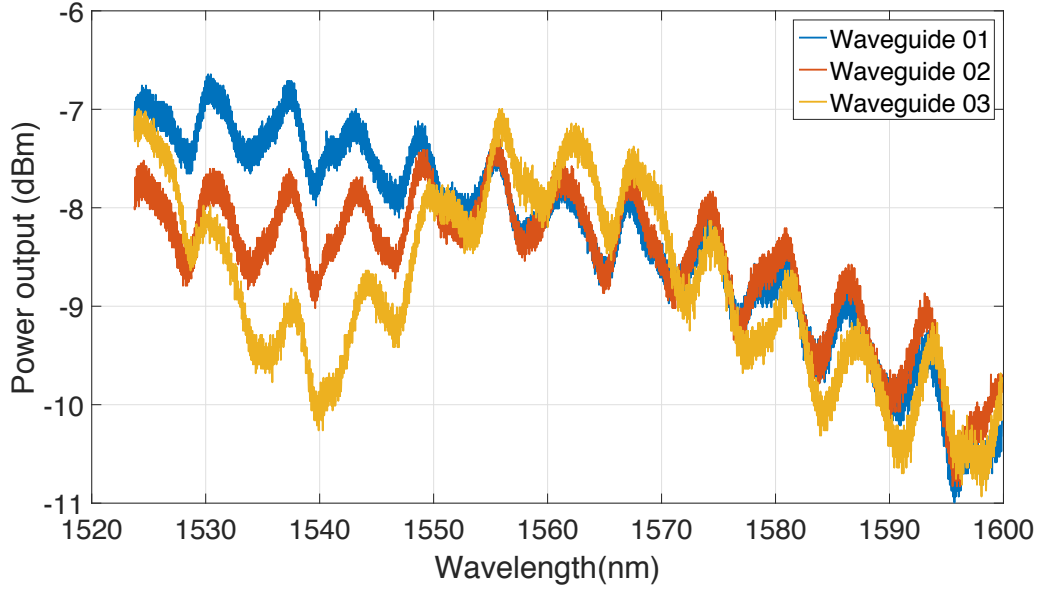


**Figure 6.28:** Results obtained using a set of nominally identical waveguides.

The first value that is possible to extract from the results in Figure 6.28 is the -8 dB average insertion loss. This level refers to the total loss of the waveguides comprising the facet coupling loss and the propagation loss (measured in dB$cm^{-1}$). In the waveguide presented the reflectivity is estimated to be:

$$R = \frac{(1 - \mathrm{n_{eff}})^2}{(1 + \mathrm{n_{eff}})^2} = \frac{(1 - 1.532)^2}{(1 + 1.532)^2} = 0.0441 \; . \tag{6.4}$$

This very low value of reflectivity doesn't allow to accurately measure the propagation loss using the Fabry Perot (FP) method presented in Section 3.3 from Eq.3.5 [99]. It is instead possible to empirically assess the value of the facet loss from measurements of a series of

fabricated device. A total facet coupling loss is empirically assessed to be around 2 dB per facet and, considering the length of these waveguide to be in the order of 11 mm it is possible to estimate the propagation loss on a value of 3.6 dB cm$^{-}$1. These results suggest that it is possible, using the DLL tool, to fabricate SU-8 single mode waveguides. The next step is therefore to try and fabricate more complex structures, starting from bend waveguide up to more useful devices like Mach Zehnder interferometers and ring resonators.

### 6.5.2 Fabrication of bend waveguide

A complete bend characterisation is necessary to obtain information about this structure and chose the correct geometrical parameters to use. To fabricate curved waveguides is important to know how the loss changes as a function of the bend radius and the bend angle. Using the DLL tool it is possible to fabricate bend with a minimum radius of 50 μm and a minimum angle of 10 degrees. A full characterisation of this last parameter has been carried out fabricating the samples which layout are shown in Figure 6.29 and Figure 6.30.
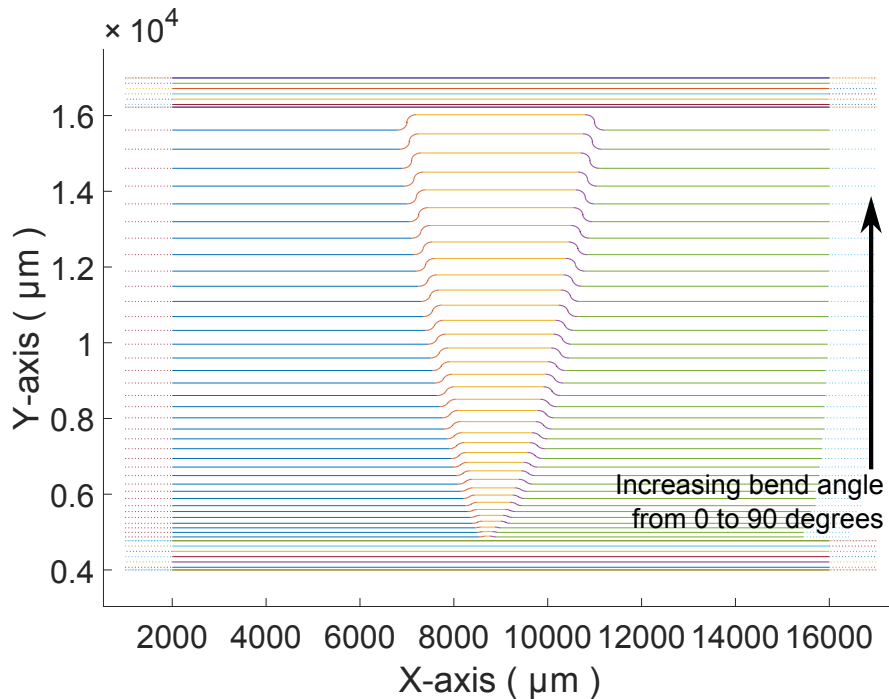


**Figure 6.29:** Mask design used to study the bend losses in function of the bend angle for a fixed radius of 200 μm.
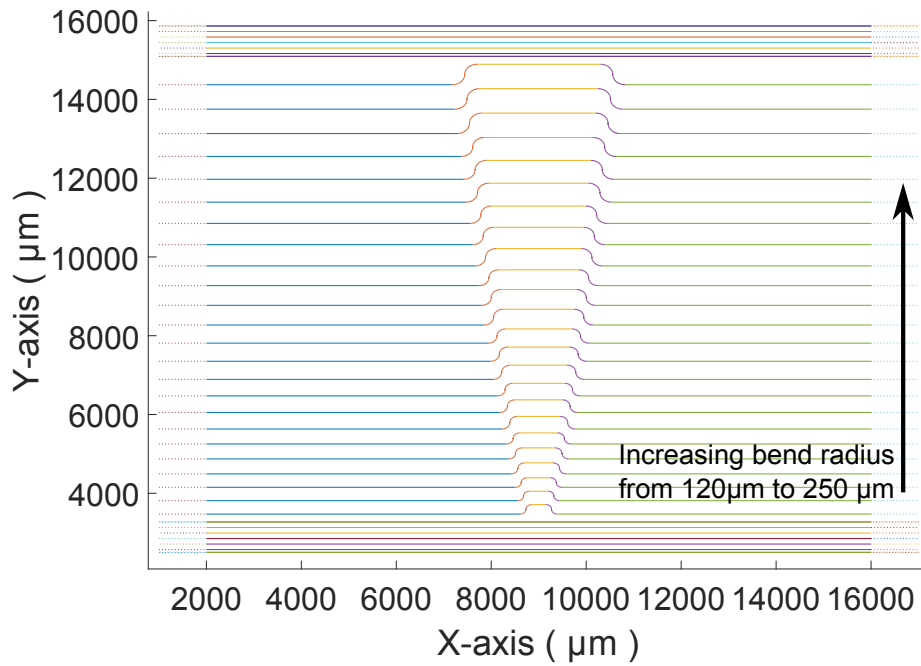
**Figure 6.30:** Mask design used to study the bend losses in function of the bend radius.

The first sample described in Figure 6.29 was fabricated maintaining the radius constant to 200 μm and varying the angle of curvature from 0 to 90 degrees while the in the second sample, described in Figure 6.30, all the bends were maintained at 90 degree with varying radius from 50 μm to 300 μm.

Transmission measurements were carried out for all the devices presented in both Figure 6.29 and Figure 6.30 in order to find the perfect combination of angle and radius to obtain the lower transmission loss. The main result obtained after these tests is shown in Figure 6.31. In this figure the average output power of the 5 straight waveguides is compared with the one related to 3 nominally identical S bends with 200 μm radius and 90 degrees angle. These angle and radius values have been chosen as the best configuration to give the lowest transmission loss values.

| Bend Radius (μm) | Bend full drop (μm) | Bend Angle (°) | Photodetector output (mV) | Power output (dBm) | Average pwr out (dBm) |
|---|---|---|---|---|---|
| 0 | 0 | 0 | 2060 | **-9.40** | |
| 0 | 0 | 0 | 2030 | **-9.47** | |
| 0 | 0 | 0 | 1950 | **-9.64** | **-9.55** |
| 0 | 0 | 0 | 1920 | **-9.71** | |
| 0 | 0 | 0 | 2000 | **-9.53** | |
| 200 | 400 | 90.00 | 970 | **-12.67** | |
| 200 | 400 | 90.00 | 985 | **-12.61** | **-12.62** |
| 200 | 400 | 90.00 | 990 | **-12.59** | |

**Figure 6.31:** Comparison between output power obtained for the set of straight waveguides and the set of S bend, with 200 μm radius and 90 degrees angle, found in the sample which layout is presented in Figure6.29.

From these results it is possible to say that using a bend configuration of 90 degrees and 200 μm radius every bend in the sample introduces an extra loss of around 0.75 dB. This because the power output difference between the straight waveguides and the S bend samples can be approximated to 3 dB and in every S bend samples there are two S bend structures which are equal to 4 bends. This loss is due to a limitation on the X-Y translational stage. During an S bend movement the stage passes through 4 steps. A first where only one of the two axes is moving, a second where both X-Y are on a circular motion path to write the first bend, a third when this movement is reversed for the second bend and a fourth step where again only one of the two axes is moving. It has been observed that a small vibration characterises all the junctions point between every step, probably due to an interference between a single axis motion signal and a dual axis motion signal. This results demonstrate that it is possible to use 90 degree curved waveguides as building blocks for more complex structures.

### 6.5.3   Fabrication of Y Junction

One of the key elements required in PIC design is the beam splitter/combiner. This is most simply obtained using a single mode optical Y-junction, a combination of two waveguides with an intersection point forming a Y geometry. Using a Y-junction, signals from separate sources can be combined, or, signals from a single source can be divided between two channels. Power dividers [138], power combiners [139], switches [140, 141], modulators [142, 143, 144], samplers [145, 146], multipliers [145], A/D converters [147], and logic gates [148] using single-mode Y-junctions have been also demonstrated. The Y-junction structure that has been fabricated follows the model in Figure 6.32. Experimental results on fabricated single mode waveguide

Y-junction are presented in Figure 6.33
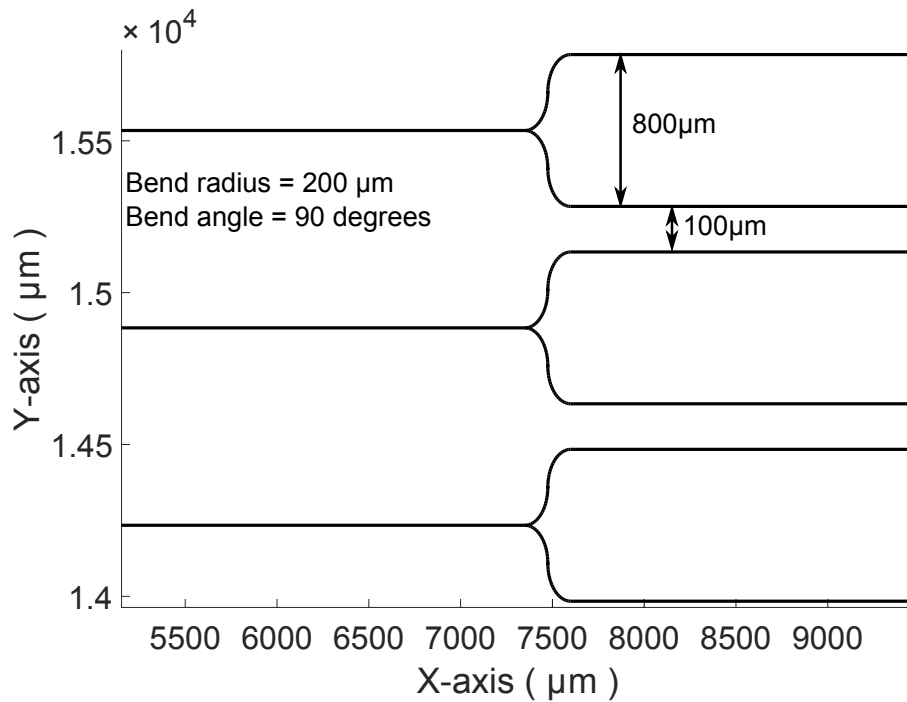


**Figure 6.32:** Mask design used to study the properties of SU-8 Y-Junction.
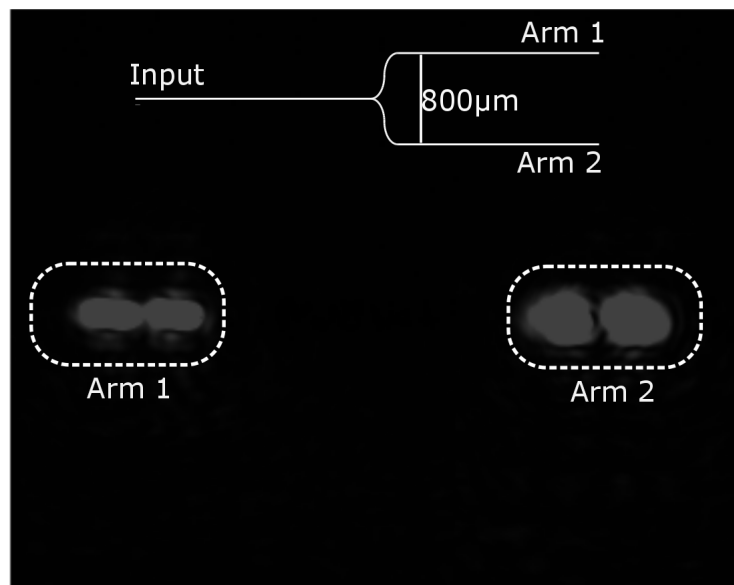


**Figure 6.33:** Mask design used to study the loss of SU-8 Y-Junction.

In Figure 6.33 (b) is possible to see the output from the CCD camera after light transmission through one of the Y-Junction. The figure shows that after the light has been coupled into

the input waveguide it is divided in two from the Y-junction and the two correlated output, whose power was measured with an InGaAs photodetector, presents a power splitting ratio of 38%:62% that can be collected separately.

In order to obtain a figure for the loss introduced from a single Y junction the full layout contains a set of straight waveguides for the loss baseline, a set of single Y-junction devices and a set with double Y-junctions. The layout is shown in Figure 6.34. Results on the output power obtained with the sample shown in Figure6.34 are shown in Figure 6.35.
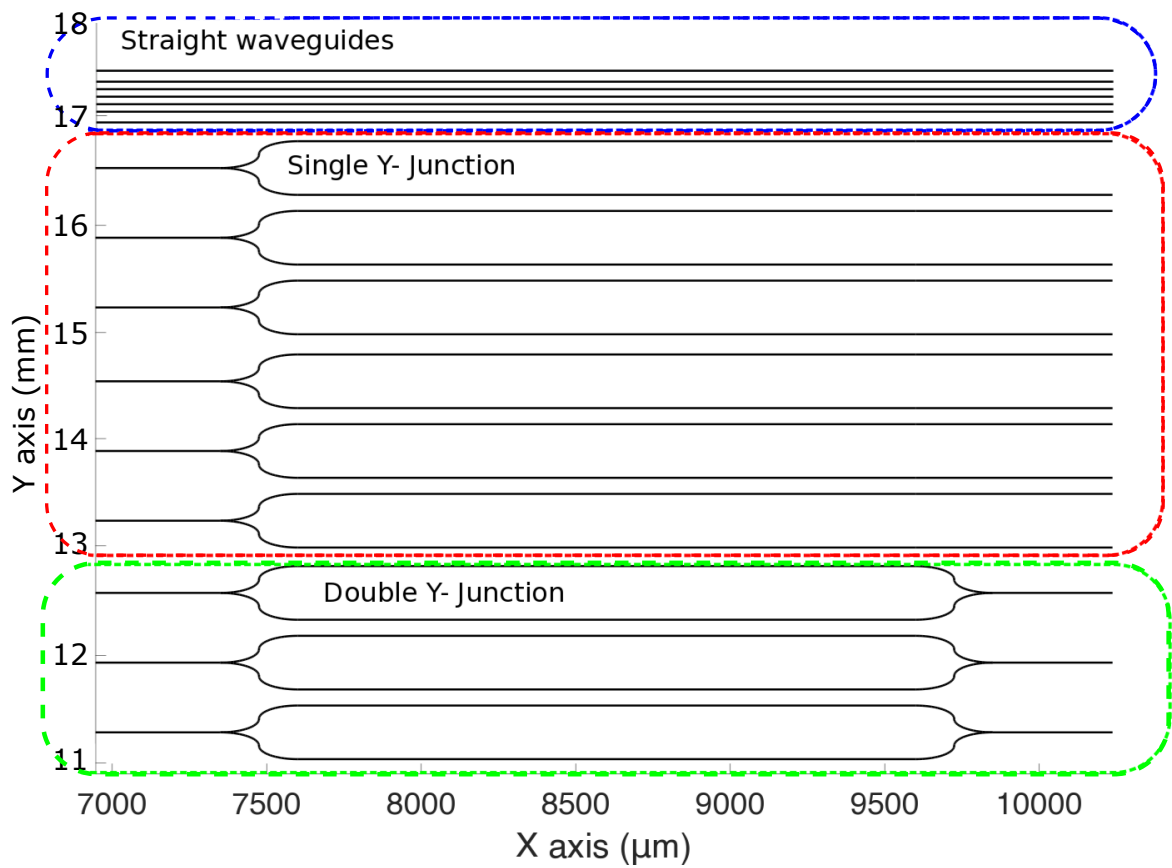


**Figure 6.34:** Mask design used to study the loss of SU-8 Y-Junction.

| Device | Bend Radius (um) | Bend Angle (°) | Total Pwr output (dBm) | Average pwr out (dBm) | Loss per Junction (dB) |
|---|---|---|---|---|---|
| Waveguide 1 | 0 | 0 | -10.09 | | |
| Waveguide 2 | 0 | 0 | -11.06 | | |
| Waveguide 3 | 0 | 0 | -12.11 | -10.30 | 0 |
| Waveguide 4 | 0 | 0 | -9.29 | | |
| Waveguide 5 | 0 | 0 | -9.97 | | |
| Single Y junction Bar | 200 | 90 | -12.01 | | |
| Single Y junction Cross | 200 | 90 | | | |
| Single Y junction Bar | 200 | 90 | -9.25 | | |
| Single Y junction Cross | 200 | 90 | | | |
| Single Y junction Bar | 200 | 90 | -9.85 | | |
| Single Y junction Cross | 200 | 90 | | -11.88 | 1.57 |
| Single Y junction Bar | 200 | 90 | -12.60 | | |
| Single Y junction Cross | 200 | 90 | | | |
| Single Y junction Bar | 200 | 90 | -13.86 | | |
| Single Y junction Cross | 200 | 90 | | | |
| Single Y junction Bar | 200 | 90 | -13.69 | | |
| Single Y junction Cross | 200 | 90 | | | |
| Double Y junction | 200 | 90 | -13.60 | | |
| Double Y junction | 200 | 90 | -13.89 | -13.64 | 1.67 |
| Double Y junction | 200 | 90 | -13.42 | | |

**Figure 6.35:** Output power measurements for the device presented in Figure 6.34.

From the results obtained using this layout it is possible to say that, for similar reason to the one introduced for the bend waveguides, introducing a Y-junction to a layout adds an extra loss value of around 1.5 dB per junction. Y-junctions are very useful for fabrication of more complex structure like MZI. These geometries are the focus of section 6.5.4.

### 6.5.4 Fabrication of Mach Zehnder interferometers

Using the DLL tool a layout of a single output Mach Zehnder, using the same dimensions used in the simulation, has been fabricated. An optical micrograph of a detail of the obtained structure is presented in Figure 6.36.
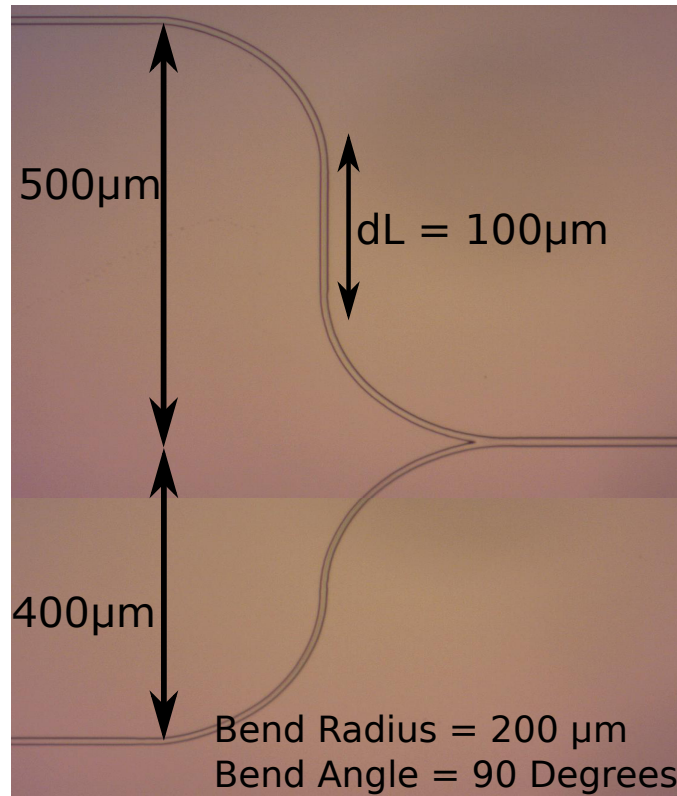
**Figure 6.36:** Picture of the final beamsplitter in the fabricated MZI. The image is a merge of two 10X microscope images.

This 200 µm length difference introduced between the right and the left path will produce the wavelength dependent interferometer in which the periodicity between constructive and destructive interference is dependent on the $\Delta$L bias introduced. Experimental results on single output MZI transmission measurements are shown in Figure 6.37.
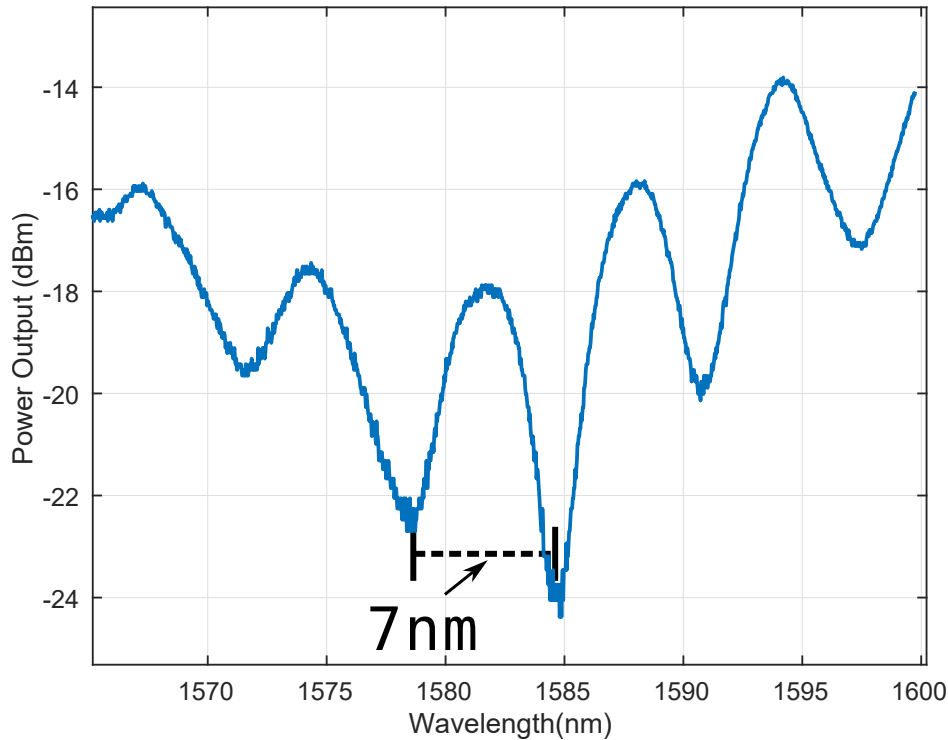
**Figure 6.37:** Transmission measurements obtained using one of the fabricated MZI.

Even though the FSR obtained in this device is similar to what obtained for the straight waveguide's results (shown in Figure 6.28) the effect of the MZI is noticed from the increasing extinction ratio of the features shown in Figure 6.37 which can't be related to polarisation rotation effects due to the abscence of an output polariser.

The results in Figure 6.37 confirm that it is possible to use the DLL tool to fabricate complex polymer structure like this Mach Zehnder interferometer. The plot shows in fact the typical transmission spectrum of an interferometer and the experimental FSR respect the predicted 7 nm value obtained in the simulation shown in Figure2.10. Part of the total insertion loss of 14 dB is due to an 6 dB average loss from the coupling to the straight waveguide (3 dB per facet) plus 3 dB loss due to the presence of two Y-Junctions. The 5 dB extra loss comes from two scattering points introduced for the same reasons explained for the bends and the Y-Junction with the only difference that in this case the stage adds one more step (therefore more loss due to vibrations) in the bend motion due to the fact that a straight vertical path is introduced between the two bends. These results prove that is is

possible to obtain complex PICs using the DLL and that, with some improvements on the hardware sensitivity it would be possible to obtain better performance in terms of losses or extinction ratio.

### 6.5.5 Fabrication of ring resonator

As it has been explained in the previous chapter, ring resonators can find its application in a variety of fields from telecommunication, to non-linar optics and bio-sensing.[149, 150]. The main reason why microring resonators are a good choice for biosensing is that, using this technology, it is possible to keep the analyte sensitivity high reducing the device sizes and also maintaining a low time response [151]. The resonant nature of this device also allows to reduce the amount of analytes needed for detection with respect to other sensing devices [152, 153, 154]. SU-8 present some interesting characteristics for this technology. This material is in fact characterised by a high structural flexibility and a high thermal stability [155].

Here, as shown before for straight waveguides and Mach Zendher interferometer, we report on the fabrication of single mode ring resonator using SU-8 as a core material. Two different types of ring resonator geometry have been designed and tested. The first one is an all pass ring resonator structure while the second is an add drop ring resonator. In both cases a characterisation of the coupling coefficient as a function of the waveguide to ring gap has been carried out. All the ring resonators fabricated in this sample have a ring radius of 200 μm, this value is related to the radius loss characterisation carried out previously. An example of the structure fabricated is presented in Figure 6.38.
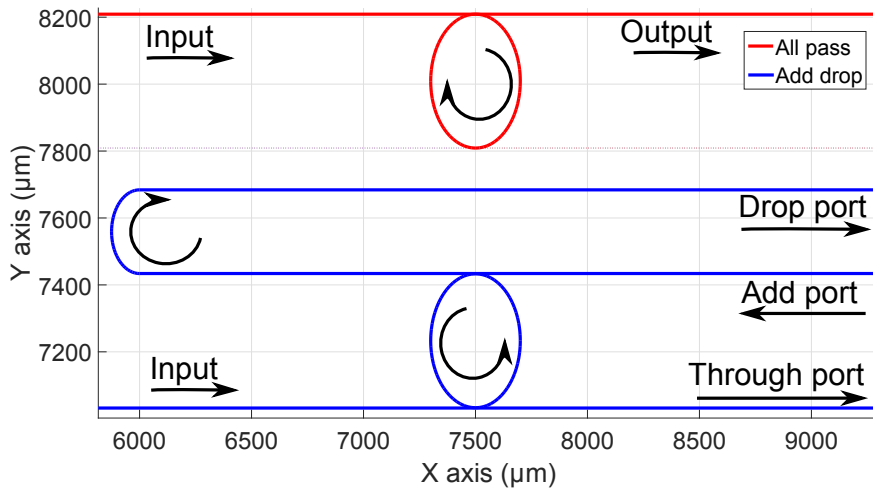
**Figure 6.38:** Mask design used to fabricate all pass and add drop ring resonators. The ring and bends have a 90 degrees angle and the ovalization in the figure is only due to a different x-y scaling.

For both the all pass and the add drop structure 6 different devices were fabricated with 0.5 μm of increasing gap, starting from 0 up to 2.5 μm gap between the ring and both waveguides. The results of the fabrication shown in Figure 6.39 and Figure 6.40 show how this gap relates only to the distance between the centre of the straight waveguide and the centre of the ring resonator waveguide in the closest point. Due to the width of the waveguides (around 5.5 μm) all of the structures have an overlap between the two waveguides but, a change of coupling coefficient is generated due to the varying distance of the two centres.
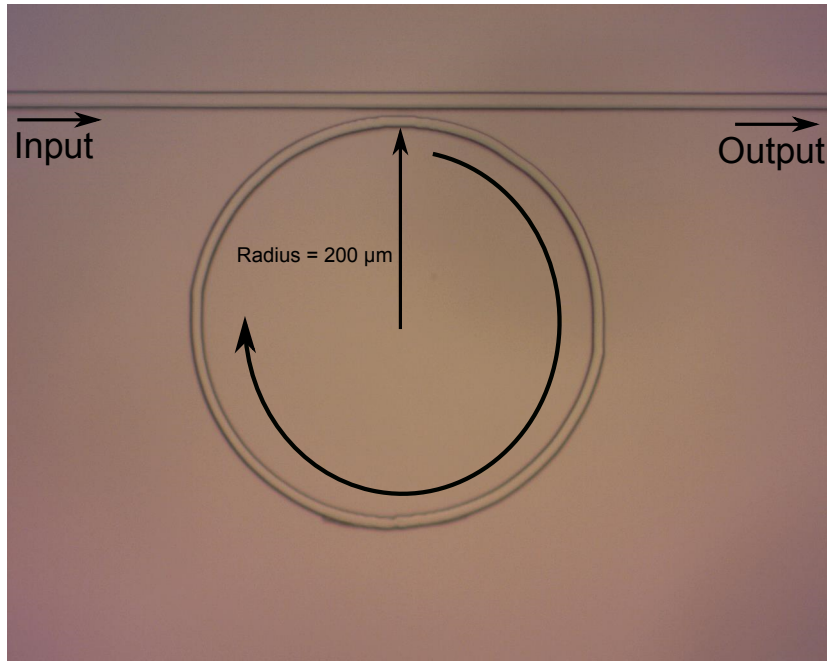
**Figure 6.39:** Microscope image of one of the fabricated all pass ring resonators.
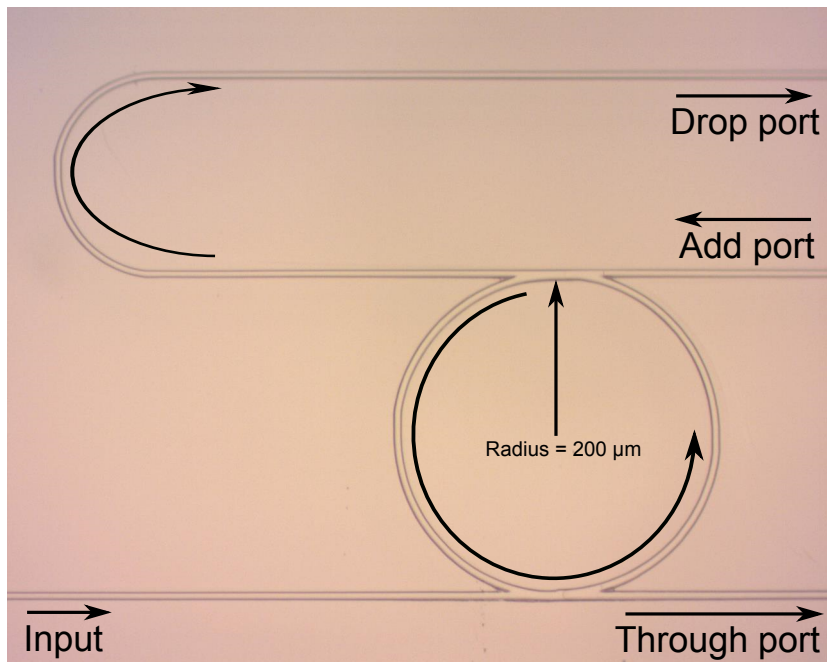


**Figure 6.40:** Microscope image of one of the fabricated add drop ring resonators.

Transmission measurements are obtained using the same experimental setup detailed in the previous section. The results regarding the all pass ring are shown in Figure 6.41
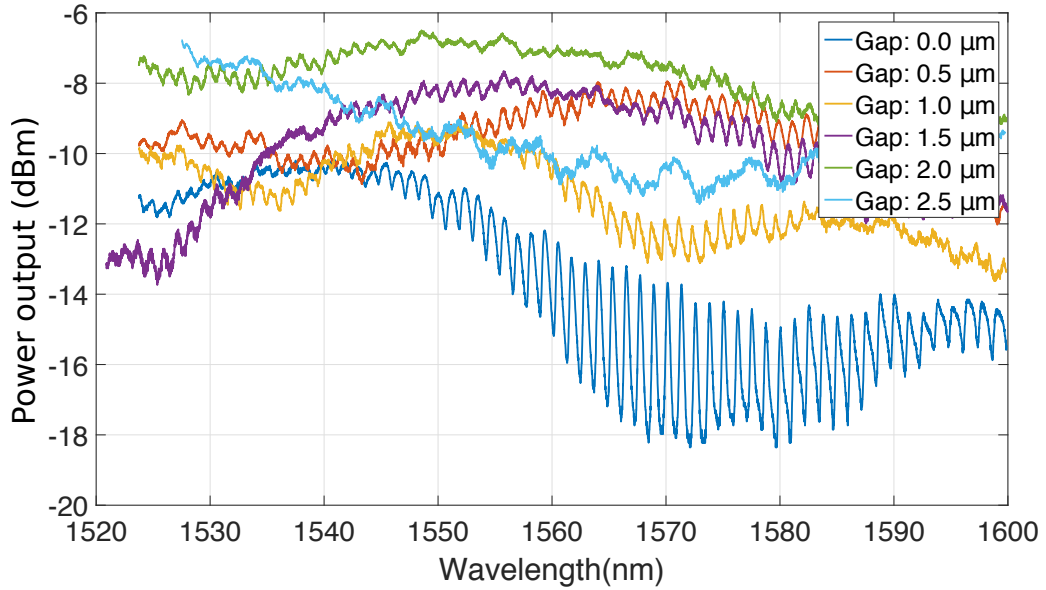
**Figure 6.41:** Transmission measurements of the fabricated all pass ring resonators in function of the gap.

The results show transmission measurements of 6 different all pass ring resonators. The difference between these devices is the designed gap between the centre of the straight coupling waveguide and the origin point of the ring resonator. This gap goes from 0 µm up to 2.5 µm with 0.5 µm steps. The results confirm that increasing this gap reduces the portion of light coupled into the ring and therefore the extinction ratio that starts from a value around 4 dB for the 0 µm gap case down to less than 1 dB for the 2.5 µm gap structure.

Using the resonances relative to the 0 µm gap ring it is possible to extract information on the ring losses, coupling coefficient $\kappa$ and Q-factor, fundamental parameters that identify the performance of this ring resonator and which theory has been described in the introduction in Section 2.2. These values are obtained curve fitting one of the ring resonances with the field propagation function with the coupling coefficient and the propagation loss as free parameters. The coupling coefficient results to be $\kappa$=0.2714 and the Q-factor is nearly 3.7 K. The obtained results are shown in Figure 6.42.
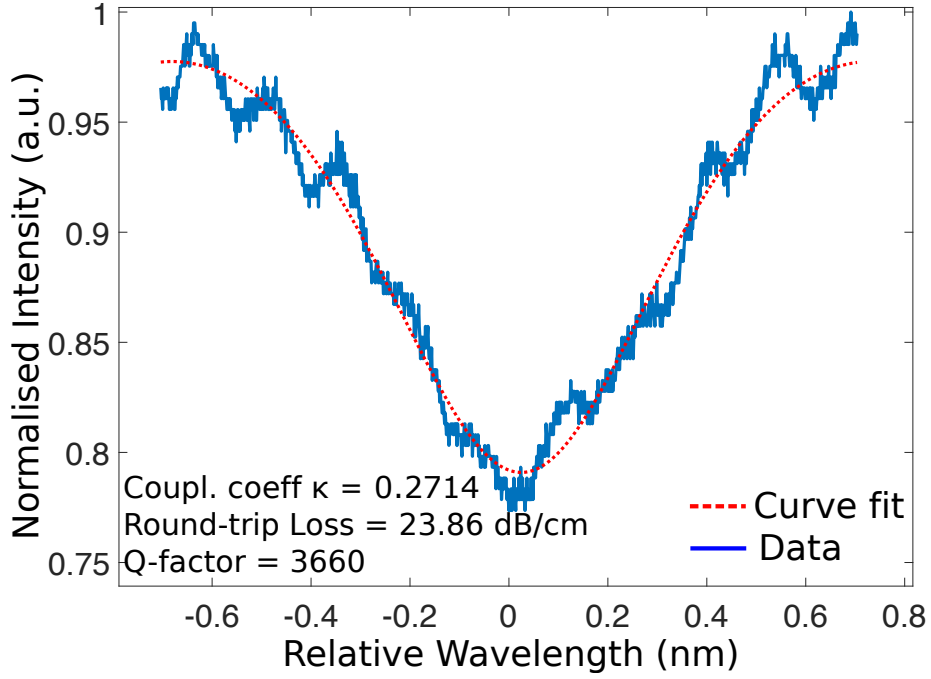
**Figure 6.42:** Linear fit of a 0 μm gap ring resonator.

The average insertion loss of 11 dB considered in this structures takes in account the 8 dB insertion loss on the straight waveguide and the 3 dB coupling loss on the ring (due to the presence of two couplers considered as two Y-Junctions). The ring's round trip loss can therefore be estimated from the length of the ring of radius R=200 μm:

$$L_{\text{Ring}} = 2\pi R = 0.1257\text{cm}$$

$$\alpha_{\text{Ring}} = \alpha_{\text{Coupling}} \times N_{\text{roundtrip}}(\text{cm}) \ . \tag{6.5}$$

where $\alpha_{\text{Coupling}}$ represents the coupling loss of the ring, estimated to be $\alpha_{\text{Coupling}} = 3$ dB and $N_{\text{roundtrip}}(\text{cm})$ represents the number of round trip that cover a distance of 1 cm (necessary to calculate the round trip loss in dB/cm. The value obtained is shown in Eq. 6.6.

$$\alpha_{\text{Ring}} = 3\text{dB} \times \frac{1\text{cm}}{L_{\text{Ring}}} = 23.86\text{dBcm}^{-1} \ . \tag{6.6}$$

From Figure 6.41 it is possible to observe that the ring FSR = 1.2 nm. Within a first order approximation of the dispersion, the FSR can be expressed as a function of the waveguide

group index:

$$\text{FSR} = \frac{\lambda^2}{n_g L} \ . \tag{6.7}$$

therefore:

$$n_g = \frac{\lambda^2}{\text{FSR}L} = 1.60 \pm 0.02 \ . \tag{6.8}$$

The $\pm$ 0.02 is due to the precision on the FSR measurements which, being measured with a precision of $\pm$ 0.1 nm gives a 2% change in the $n_g$ calculation. Using the DLL tool it was possible not only to create all pass ring resonator structures but also add drop ring resonator, as shown in Figure 6.40. A result obtained using one of the add drop configuration (with 0 µm gap) is shown in Figure 6.43. Due to the way the drop port has been designed, the presence of 2 more bends with respect to the through port increase losses of 5 dB more in this output.
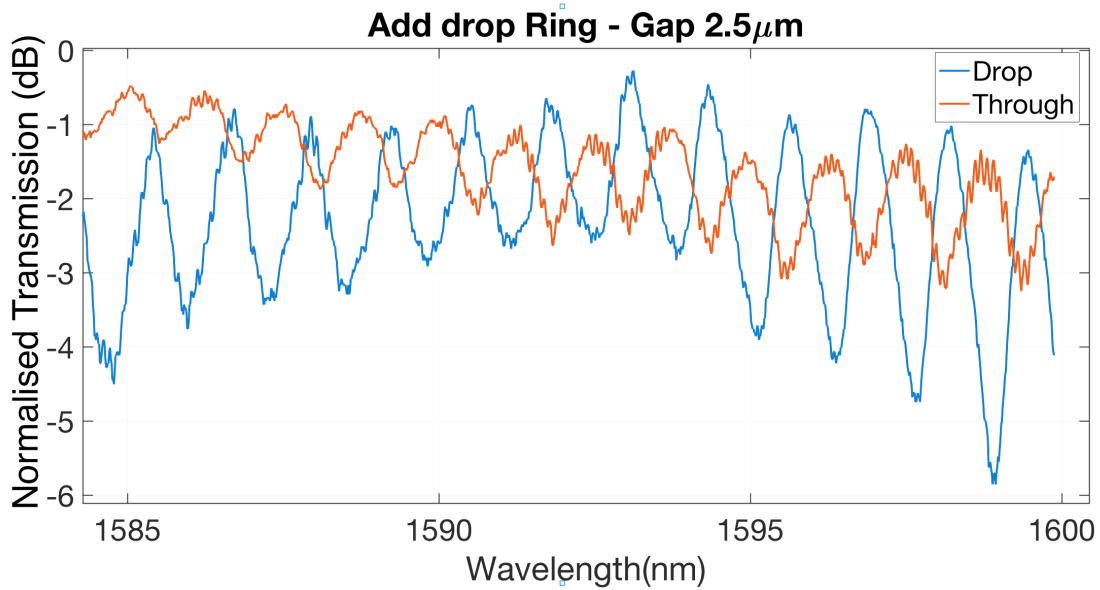


**Figure 6.43:** Example of the transmission measurements obtained using the fabricated add drop ring resonators.

Although the losses for the drop port in this case are high, the main focus of this fabrication at this stage was to demonstrate that the laser lithography tool is capable of fabricating a working add-drop ring resonator geometry able to couple light from the injection waveguide to the drop port output. For this reason in order to better visualise the effect of the add-drop

ring resonator the results presented in Figure 6.43 are normalised to their maximum value.

## 6.6    Conclusions

In this chapter a new custom made mask-less lithography system based on direct laser lithography has been presented. This system, defined as the direct laser lithography, has been proved to be useful to fabricate many of the principal photonic integrated designs using polymer SU-8. With the DLL tool it is possible to fabricate devices starting from simple building blocks such as straight waveguides and bends to more complex structure like MZI and ring resonators. The fabrication of these devices is less expensive and time consuming than using the ordinary mask aligner or electron beam lithography, it allows in fact to generate a sample, starting from the mask layout to the made device, in only couple of hours allowing the user to test the sample and make any necessary changes in new layouts all in the same day. All the obtained devices show similar characteristics to what can be fabricated using other lithography techniques.

# Chapter 7

# Conclusion

In conclusion, a summary of all the experiments and results shown in this doctoral dissertation is here described with links to possible future work and applications of the technology described.

## 7.1 Summary of key findings

In this doctoral dissertation the design, fabrication and characterization of state of the art PICs for non-linear application have been described. In the first chapter an introduction on the theory and application of the main PICs have been carried out with details on Ring resonators and Bragg grating and on non-linear process like FWM.

The focus of the work is then moved on the performance of state of the art SOI photonic integrated circuits. At first, the effect of TE and TM polarised modes in standard ring resonator and Bragg grating structures is presented and then two dual polarisation filter geometries with a dual polarisation high rejection ratio are demonstrated, with the aim of solving the filter polarisation mode dependency. One of the main key finding in this chapter is the possibility of using plasmonic waveguides or dual TE/TM gratings to be able to filter, on chip, all the injected light without regarding the polarisation, with extincion levels up to $\approx 60dB$.

The described three rings cascade filter is then used in applications in non-linear optics. In particular results on non-linear FWM experiments are demonstrated. In this case, ring

resonators are used for both photon pair generation and residual pump filtering. In this chapter, the non-linear four-wave mixing effect has been exploited including a review of possible applications in integrated photonics with particular attention on application with ring resonators. It has also been shown how the FE factor has a main role on the FWM efficiency optimisation and how, given fabrication tolerances, this value can shift drastically only with a change in resonator cross-coupling coefficient of a few percent. An active tuning of the device post-fabrication needs therefore to be implemented in the chip electrically controlling with resistive heating elements, the ring coupling coefficient. FWM efficiencies were demonstrated at milliwatts power levels using this tunable ring device. In the last section, monolithically integrating this non-linear generation device with the ring resonator cascade filter technology shown in Chapter4, FWM experiments were carried out obtaining an on chip dual polarisation pump extinction of 62 dB and low insertion loss of the transmitted signal and idler of 1.8 dB. In this chapter, analysis on the substrate scattering light have also been carried out.

In Chapter 4, stabilization of silicon micro-resonators using a micro-processor based feedback control loop is presented. This process of stabilisation is a key requirement for the inclusion of PIC micro-resonator in larger photonic integrated circuits. In particular, thermal refractive index shift in non-linear applications can detune devices from their optimal working point. The key findings regard the results obtained using a cavity stabilization scheme based on a micro-processor feedback control loop. The stabilisation system is based on a local thermal heater element on-chip and, using this method, a silicon $\pi$-phase shifted grating with a cavity Q-factor of 40k is demonstrated to operate over an ambient temperature detuning range of 40 $^o$C and injection wavelength range of 1.5 nm, nearly 3 orders of magnitude greater than the resonant cavity linewidth.

In Chapter 5 the realisation of a custom made laser lithography system and the related results obtained on microfabrication of PICs are in fact described. The direct laser lithography presented is a mask-less photolithography system that helps on cutting the cost of mask manufacturing and as well as this, increase the achievable resolution, with respect to the one obtained using mask aligner lithography, up to submicron dimensions. The first part of the chapter deal with the description of all the system hardware and software including all

the main fixed bugs. Once characterised, the system has been used to fabricate $SU-8$ on $SiO_2$ PIC like straight waveguides, bends, Mach-Zehnder interferometer and ring resonator. A full characterisation of those fabricated device is also presented in this chapter. One of the key finding in this work is that with the DLL tool it is possible to fabricate devices starting from simple building blocks such as straight waveguides and bends to more complex structure like Mach Zehnder interferometers and ring resonators. The fabrication of these devices is less expensive and time consuming than using the ordinary mask aligner or electron beam lithography, it allows in fact to generate a sample, starting from the mask layout to the made device, in only couple of hours allowing the user to test the sample and make any necessary changes in new layouts all in the same day. All the obtained devices show similar characteristics to what can be fabricated using other lithography techniques. All the more complex structures also show possibilities of being used for further applications, i.e. sensing.

## 7.2   Future research

The main focus of this doctoral dissertation is toward new technology for non-linear operations in PICs. One of the main reason for this is the possible applications that non-linear processes in PICs can have in telecommunication and also in quantum optics. This because e.g. the generated signal and idler photons in a FWM process are correlated and their average energy must be equal to two of the pump photons that create them. This means that FWM can also be used to generate entangled photons [38, 39], key elements for Bell type experiments. Furthermore, ring resonator based spontaneous FWM photon-pair sources can be made highly indistinguishable with small spectral correlations [156].

The produced photon pair in a FWM experiments can also finds applications in wavelength conversion [40, 41] and all-optical signal processing [42, 43]. In all these applications the performance required for photonic filters are different but a common characteristic is the necessity of filtering the light without regards on the polarisation. This is why the system presented can be used for this application that requires dual TE and TM filtering and, depending on the level of extinction required, chaning the number of rings involved this

technology can easily be customised. The feedback loop control system introduced can also be used for stabilisation of this non-linear processes. This because, with its maximum speed of tens of KHz, is found to be on track with the performance that can be obtained in quantum optics experiments, were the bottle neck is represented by the photon pair generation rate [109] [156]. It is clear therefore that the integration of high-performance components, like the one described in this work, is necessary for building quantum devices to exploit photonic entanglement on the large scale.

# Bibliography

[1] S. Assefa *et al.*, "A 90nm cmos integrated nano photonics technology for 25 gbps wdm optical communications applications," *IEEE International Electron Devices Meeting*, 2012.

[2] Intel, "The 50G Silicon photonics link," *Intel labs*, 2010.

[3] V. Heuring *et al.*, "Bit-serial architecture for optical computing D = AC + BC," *Applied optics*, vol. 31, no. 17, pp. 3213–3224, 1992.

[4] M. Salib *et al.*, "Silicon photonics," *Intel Technology Journal*, vol. 8, pp. 143–161, 2004.

[5] V. Almeida *et al.*, "Optical bistability on a silicon chip." *Opt. Lett., 29(20):2387–2389*, 2004.

[6] L. Wada *et al.*, "On-chip interconnection beyond semiconductor roadmap - Silicon microphotonics," *Proc. SPIE*, vol. 4870, pp. 437–443, 2002.

[7] G. Reed *et al.*, *Silicon Photonics: An Introduction.* Wiley, 2004.

[8] W. Bogaerts *et al.*, "Nanophotonic Waveguides in Silicon-on-Insulator Fabricated With CMOS Technology," *Journal of Lightwave Technology*, vol. 23, pp. 401–412, 2005.

[9] C. Gunn *et al.*, "CMOS Photonics for High-Speed Interconnects," *IEEE Micro*, vol. 26, pp. 58–66, 2006.

[10] A. Biberman *et al.*, "First demonstration of long-haul transmission using silicon microring modulators." *Optics Express*, vol. 18, pp. 15544–15552, 2010.

[11] S. Xiao *et al.*, "Compact silicon microring resonators with ultra-low propagation loss in the C band." *Optics Express*, vol. 15, pp. 14467–14475, 2007.

[12] K. D. Vos *et al.*, "Optical biosensor based on silicon-on-insulator microring cavities for specific protein detection." *Proc. SPIE, 6447:6447DK–1*, 2007.

[13] G. Pryde *et al.*, "Demonstration of an all-optical quantum controlled-NOT gate," *Letters to Nature*, vol. 426, pp. 108–111, 2003.

[14] J. Silverstone *et al.*, "On-chip quantum interference between silicon photon-pair sources," *Nature Photonics*, vol. 8, pp. 2–6, 2013.

[15] A. Politi *et al.*, "Integrated Quantum Photonics," *IEEE Journal of Selected Topics in Quantum Electronics*, vol. 15, pp. 1673–1684, 2009.

[16] J. Sun *et al.*, "Large-scale nanophotonic phased array." *Nature*, vol. 493, no. 7431, pp. 195–9, 2013.

[17] S. Meister *et al.*, " Photonic Integrated Circuits for Optical Communication," *Optik and Photonik*, vol. 7, pp. 59–62, 2012.

[18] C. Sun *et al.*, "Single-chip microprocessor that communicates directly using light," *Nature*, vol. 528, no. 7583, pp. 534–538, 2015.

[19] S. Cheung *et al.*, " Ultra-Compact Silicon Photonic 512 ÃŮ 512 25 GHz Arrayed Waveguide Grating Router," *IEEE Journal Of Selected Topics In Quantum Electronics*, vol. 20, pp. 4–10, 2014.

[20] "Kaiam corp transcivers manufacturing," http://www.kaiam.com/, accessed: 2017-05-12.

[21] J. O'Brien *et al.*, "Continuous-variable entanglement on a chip," *Nature Photonics*, vol. 3, p. 687, 2009.

[22] A. Faraon *et al.*, " Off-resonant coupling between a single quantum dot and a nanobeam photonic crystal cavity ," *New Journal of Physics*, vol. 13, p. 055025, 2011.

[23] S. Wang *et al.*, "A 14 x 14âĂĽ$\mu m^2$ footprint polarization-encoded quantum controlled-NOT gate based on hybrid waveguide ," *Nature Communications*, vol. 7, p. 11490, 2016.

[24] J. Lukens *et al.*, "Frequency-encoded photonic qubits for scalable quantum information processing ," *Arxiv*, vol. 1, pp. 1–13, 2016.

[25] Z. Zhou *et al.*, "Orbital Angular Momentum-Entanglement Frequency Transducer ," *Phys. Rev. Lett.*, vol. 117, p. 103601, 2016.

[26] J. Howell *et al.*, "Realization of the Einstein-Podolsky-Rosen Paradox Using Momentum- and Position-Entangled Photons from Spontaneous Parametric Down Conversion," *Phys. Rev. Lett.*, vol. 92, p. 210403, 2004.

[27] R. Hadfield, " Single-photon detectors for optical quantum information applications," *Nature Photonics*, vol. 3, pp. 696–705, 2009.

[28] J. Spring *et al.*, "Single-Photon Generation and Detection: Physics and Applications," *Science*, vol. 339, p. 798, 2013.

[29] A. Politi *et al.*, "Silica-on-silicon waveguide quantum circuits," *Science*, vol. 320, p. 646, 2008.

[30] J. Carolan *et al.*, "Characterization of optical quantum circuits using resonant phase shifts," *Science*, vol. 349, p. 711, 2015.

[31] G. Marshall *et al.*, "Laser written waveguide photonic quantum circuits," *Optics Express*, vol. 17, p. 12546, 2009.

[32] C. Xiong *et al.*, "Broadband nanophotonic waveguides and resonators based on epitaxial GaN thin films," *Optics Express*, vol. 19, p. 10462, 2011.

[33] H. Jin *et al.*, "On-chip generation and manipulation of entangled photons based on reconfigurable lithium-niobate waveguide circuits," *Physical Review Letters*, vol. 113, p. 103601, 2014.

[34] J. Wang *et al.*, "Single-photon emission of InAs/InP quantum dashes at 1.55 $\mu$m and temperatures up to 80âĂĽK," *Optics Communication*, vol. 327, p. 49, 2014.

[35] D. Bonneau *et al.*, "Active temporal multiplexing of indistinguishable heralded single photons," *New Journal of Physics*, vol. 17, p. 043057, 2015.

[36] N. Harris *et al.*, "Bosonic transport simulations in a large-scale programmable nanophotonic processor," *arXiv:1507.03406*, 2015.

[37] Q. Lin *et al.*, " Single Silicon waveguides for creating quantum-correlated photon pairs," *Optics Letters*, vol. 31, p. 21, 2006.

[38] S. Clemmen *et al.*, "Continuous wave photon pair generation in silicon-on-insulator waveguides and ring resonators." *Opt. Express, 17(19):16558–16570*, 2009.

[39] H. Takesue *et al.*, "Entanglement Generation Using Silicon Photonic Wire Waveguide." *J. Nanosci. Nanotechnol., 10(3, Sp. Iss. SI):1814– 1818*, 2010.

[40] S. Preble *et al.*, "Changing the colour of light in a silicon resonator." *Nature Photonics, 1(5):293– 296*, 2007.

[41] A. Turner *et al.*, "Ultra-low power parametric frequency conversion in a silicon microring resonator." *Opt. Express, 16(7):4881–4887*, 2008.

[42] R. Salem *et al.*, "Signal regeneration using low- power four-wave mixing on silicon chip." *Nature Photonics, 2(1):35–38*, 2008.

[43] K. Yamada *et al.*, "All-optical signal processing using nonlinear effects in silicon photonic wire waveguides." *In 2006 IEEE LEOS Annual Meeting Conference Proceedings, Vols 1 and 2, IEEE Lasers and Electro-Optics Society (LEOS) Annual Meeting, pages 613–614, Montreal, Canada*, 2006.

[44] M. Ferrera *et al.*, "Low power four wave mixing in an integrated, micro-ring resonator with Q = 1.2 million." *Optics Express*, vol. 17, pp. 14 098–14 103, 2009.

[45] P. Dong *et al.*, "GHz-bandwidth optical filters based on high-order silicon ring resonators." *Optics Express*, vol. 18, pp. 23 784–23 789, 2010.

[46] X. Wang *et al.*, "Narrow-band transmission filter using phase-shifted Bragg gratings in SOI waveguide," *IEEE Photonic Society 24th Annual Meeting*, vol. 19, no. 12, pp. 25–26, 2011.

[47] X.Wang *et al.*, "Silicon photonic slot waveguide Bragg gratings and resonators." *Optics Express*, vol. 21, pp. 19 029–39, 2013.

[48] T. Liow *et al.*, "Silicon High-Order Coupled-Microring-Based Optical Interconnects," *IEEE Photonics Technology Letters*, vol. 24, pp. 821–823, 2012.

[49] J. Ong *et al.*, "Silicon microring-based wavelength converter with integrated pump and signal suppression." *Optics Letters*, vol. 39, pp. 4439–4441, 2014.

[50] N.Harris *et al.*, "Integrated Source of Spectrally Filtered Correlated Photons for Large-Scale Quantum Photonic Systems," *Physical Review X*, vol. 4, pp. 1–10, 2014.

[51] J. Ong *et al.*, "Ultra-High-Contrast and Tunable-Bandwidth Filter Using Cascaded High-Order Silicon Microring Filters," *IEEE Photonics Technology Letters*, vol. 25, pp. 1543–1546, 2013.

[52] F. Morichetti *et al.*, "Roughness Induced Backscattering in Optical Silicon Waveguides," *Physical Review Letters*, vol. 1, pp. 1–4, 2010.

[53] C. Reimer *et al.*, "Cross-polarized photon-pair generation and bi-chromatically pumped optical parametric oscillation on a chip," *Nature Communications*, vol. 6, no. October, p. 8236, 2015.

[54] R. Völkel *et al.*, "Microlens Lithography and Smart Masks," *Microelectronic Engineering 35 (1997) 513-516*, 2000.

[55] W. Bogaerts *et al.*, "Silicon Microring Resonators," *Laser & Photonics Reviews*, vol. 6, pp. 47–73, 2012.

[56] A. Yariv *et al.*, "Critical coupling and its control in optical waveguide-ring resonator systems," *IEEE Photonics Technology Letters*, vol. 14, no. 4, pp. 483–485, 2002.

[57] A.Othonos *et al.*, *Fiber Bragg Gratings. Fundamentals and Applications in Telecommunications and Sensing.* Artech House, 1999.

[58] D. Lam *et al.*, "Characterization of single-mode optical fiber filters." *Applied Optics*, vol. 20, no. 3, pp. 440–445, 1981.

[59] C. Klitis *et al.*, "Polarisation selective bragg filters on silicon-on-insulator," *Ph.D. Research in Microelectronics and Electronics (PRIME), 2015*, pp. 353–356, 2015.

[60] T.Erdogan, "Fiber Grating Spectra," *Journal of Lightwave Technology*, vol. 15, no. 8, pp. 1277–1294, 1997.

[61] A. Yariv, "Coupled-mode theory for guided-wave optics." *IEEE J. Quantum Electron.*, vol. QE-9, pp. 919–933, 1973.

[62] F. Ouellette, "Dispersion cancellation using linearly chirped Bragg grating filters in optical waveguides," *Optics Letters*, vol. 12, pp. 847–849, 1987.

[63] K. Hill *et al.*, "Fiber Bragg grating technology fundamentals and overview," *Journal of Lightwave Technology*, vol. 15, p. 8, 1997.

[64] C. Lacava *et al.*, "Integrated nonlinear Mach Zehnder for 40 Gbit/s all-optical switching," *Optics Express*, vol. 21, no. 18, pp. 21 587–21 595, 2013.

[65] G. Mashanovich *et al.*, "Mid-infrared photonics devices in SOI," *Proc. SPIE 8629, Silicon Photonics VIII, 86290J*, pp. 2–7, 2013.

[66] B. Jalali *et al.*, "Light generation, amplification, and wavelength conversion via Stimulated Raman Scattering in silicon microstructures." *Silicon Photonics*, vol. 94, pp. 199–238, 2004.

[67] R. Claps *et al.*, "Anti-Stokes Raman conversion in silicon waveguides," *Opt. Express, 11(22):2862–2872*, 2003.

[68] R. Claps *et al.*, "Stimulated Raman scattering in silicon waveguides," *Electron Lett., 38(22):1352–1354*, 2002.

[69] A. Liu *et al.*, "Net optical gain in a low loss silicon-on-insulator waveguide by stimulated Raman scattering," *Opt. Express, 12(18):4261–4268*, 2004.

[70] T. Johnson *et al.*, "Self-induced optical modulation of the transmission through a high-q silicon microdisk resonator," *Opt. Express, 14(2):817–831*, 2006.

[71] T. Liang *et al.*, "Efficient Raman amplification in silicon-on-insulator waveguides," *Appl. Phys. Lett., 85(16):3343–3345*, 2004.

[72] R. Jones *et al.*, "Net continuous wave optical gain in a low loss silicon-on-insulator waveguide by stimulated Raman scattering," *Opt. Express, 13(2):519–525*, 2005.

[73] R. C. D. Dimitropoulos *et al.*, "Observation of stimulated Raman amplification in silicon waveguides," *Opt. Express, 11(15):1731–1739*, 2003.

[74] H. Rong *et al.*, "An all-silicon Raman laser," *Nature, 433(7023):292–294*, 2005.

[75] O. Boyraz *et al.*, "Demonstration of directly modulated silicon Raman laser," *Opt. Express, 13(3):796–800*, 2005.

[76] O. Boyraz *et al.*, "Demonstration of a silicon Raman laser," *Opt. Express, 12(21):5269–5273*, 2004.

[77] E. Dulkeith *et al.*, "Self-phase-modulation in submicron silicon- on-insulator photonic wires," *Opt. Express, 14(12):5524– 5534*, 2006.

[78] R. Dekker *et al.*, "Ultrafast Kerr-induced all- optical wavelength conversion in silicon waveguides using 1.55 mumfemtosecond pulses," *Opt. Express, 14(18):8336– 8346*, 2006.

[79] R. Soref *et al.*, "Electrooptical effects in silicon," *J. Quantum Electron., 23(1):123 – 129*, 1987.

[80] H. Tsang *et al.*, "Optical dispersion, two-photon absorption and self-phase modulation in silicon waveguides at 1.5 mu m wavelength," *Appl. Phys. Lett., 80(3):416–418*, 2002.

[81] P. Dumon *et al.*, "Linear and nonlinear nanophotonic devices based on silicon-on- insulator wire waveguides," *J. Appl. Phys. part 1, 45(8B):6589–6602*, 2006.

[82] R. Jacobsen *et al.*, "Strained silicon as a new electro-optic material," *Nature, 441(7090):199–202*, 2006.

[83] A. Bristow *et al.*, "Two-photon absorption and Kerr coefficients of silicon for 850 - 2200 nm," *Journal of Lightwave Technology*, vol. 90, p. 191104, 2007.

[84] R. Espinola *et al.*, "C-band wavelength conversion in silicon photonic wire waveguides." *Opt. Express, 13(11):4341– 4349*, 2005.

[85] I. Hsieh *et al.*, "Supercontinuum generation in silicon photonic wires." *Opt. Express, 15(23):15242–15249*, 2007.

[86] A. Savchenkov *et al.*, "Tunable optical frequency comb with a crystalline whispering gallery mode resonator." *Phys. Rev. Lett., 101(9)*, 2008.

[87] M. Popovic *et al.*, "General approach to hitless switching and FSR extension for resonators in integrated photonic circuits." *National Fiber Optic Engineers Conference, pages 714–716, Anaheim, CA*, 2006.

[88] M. Ferrera *et al.*, "Low-power continuous-wave nonlinear optics in doped silica glass integrated waveguide structures," *Nature Photonics*, vol. 2, no. 12, pp. 737–740, 2008.

[89] B. Corcoran *et al.*, "Green light emission in silicon through slow-light enhanced third- harmonic generation in photonic-crystal waveguides." *Nature Photonics, 3(4):206–210*, 2009.

[90] H. Fukuda *et al.*, "Four-wave mixing in silicon wire waveguides." *Opt. Express, 13(12):4629–4637*, 2005.

[91] P. Orlandi *et al.*, "Photonic Integrated Filter With Widely Tunable Bandwidth," *Journal of Lightwave Technology*, vol. 32, pp. 897–907, 2014.

[92] S. Ristic *et al.*, "An Optical Phase-Locked Loop Photonic Integrated Circuit," *Journal of Lightwave Technology*, vol. 28, pp. 526–538, 2010.

[93] A. Huang *et al.*, "A 10Gb/s photonic modulator and WDM MUX/DEMUX integrated with electronics in 0.13/spl mu/m SOI CMOS," *Solid-State Circuits Conference, 2006. ISSCC 2006. Digest of Technical Papers. IEEE International*, vol. 13, pp. 922–929, 2006.

[94] T. Claes *et al.*, "Multiplexed Antibody Detection With an Array of Silicon-on-Insulator Microring Resonators," *IEEE Photonics Journal*, vol. 1, pp. 457–458, 2009.

[95] D. Grassani *et al.*, "A micrometer-scale integrated silicon source of time-energy entangled photons," *Optica*, vol. 2, pp. 88–94, 2015.

[96] V. Almeida *et al.*, "All-optical control of light on a silicon chip," *Letters to Nature*, vol. 431, pp. 1081–1084, 2004.

[97] M. Strain *et al.*, "Multi-wavelength filters in silicon using superposition sidewall Bragg grating devices." *Optics Letters*, vol. 39, pp. 413–6, 2014.

[98] D. Hofstetter *et al.*, "Theory of loss measurements of Fabry Perot resonators by Fourier analysis of the transmission spectra," *Optics Letters*, vol. 22, no. 24, p. 1831, 1997.

[99] E. Kapon *et al.*, "Low-loss single-mode GaAs/AlGaAs optical waveguides grown by organometallic vapor phase epitaxy," *Applied Physics Letters*, vol. 50, no. 23, pp. 1628–1630, 1987.

[100] J. Poon *et al.*, "Designing coupled-resonator optical waveguide delay lines," *Journal of the Optical Society of America B*, vol. 21, p. 1665, 2004.

[101] J. Poon *et al.*, "Matrix analysis of microring coupled-resonator optical waveguides." *Optics Express*, vol. 12, pp. 90–103, 2004.

[102] F. Morichetti *et al.*, "Travelling-wave resonant four-wave mixing breaks the limits of cavity-enhanced all-optical wavelength conversion." *Nature communications*, vol. 2, no. 296, pp. 1–8, 2011.

[103] X. Sun *et al.*, "Experimental demonstration of a hybrid plasmonic transverse electric pass polarizer for a silicon-on-insulator platform." *Optics Letters*, vol. 37, pp. 4814–6, 2012.

[104] P. Orlandi *et al.*, "Tunable silicon photonics directional coupler driven by a transverse temperature gradient." *Optics Letters*, vol. 38, pp. 863–5, 2013.

[105] D. Tan *et al.*, "Chip-scale dispersion engineering using chirped vertical gratings." *Optics Letters*, vol. 33, pp. 3013–3015, 2008.

[106] C. Sima *et al.*, "Simple planar Bragg grating devices for photonic Hilbert transformer," *Journal of Physics: Conference Series*, vol. 276, p. 012089, 2011.

[107] L. Rivas *et al.*, "Picosecond linear optical pulse shapers based on integrated waveguide Bragg gratings," *Optics Letters*, vol. 33, pp. 2425–2427, 2008.

[108] Y. D. Koninck *et al.*, "Experimental demonstration of a hybrid III-V-on-silicon microlaser based on resonant grating cavity mirrors." *Optics Letters*, vol. 38, pp. 2496–8, 2013.

[109] M. Collins *et al.*, "Integrated spatial multiplexing of heralded single-photon sources," *Nature Communications*, vol. 4, pp. 1–7, 2013.

[110] S. Azzini *et al.*, "Ultra-low power generation of twin photons in a compact silicon ring resonator." *Optics Express*, vol. 20, pp. 23 100–7, 2012.

[111] G. Agrawal, *Nonlinear Fiber Optics, Second Edition (Cp 10).* San Diego, USA: Academic Press, 1995.

[112] R. Boyd, *Nonlinear Optics, Third Edition.* Elsevier Inc, 2008.

[113] R. Stolen *et al.*, "Optical Kerr effect in glass waveguide," *Applied Physics Letters*, vol. 22, no. 6, pp. 294–296, 1973.

[114] Y. Guo *et al.*, "Telecom-band degenerate-frequency photon pair generation in silicon microring cavities," *Optics Letters*, vol. 39, no. 8, pp. 2526–2529, 2014.

[115] P. Absil *et al.*, "Wavelength conversion in GaAs micro-ring resonators." *Optics letters*, vol. 25, no. 8, pp. 554–556, 2000.

[116] M. Strain *et al.*, "Tunable Q-factor silicon micro-ring resonators for ultra-low power parametric processes," *Optics Letters*, vol. 40, no. 7, pp. 4–7, 2014.

[117] S. Azzini *et al.*, "From classical four-wave mixing to parametric fluorescence in silicon microring resonators," *Optics Letters*, vol. 37, no. 18, p. 3807, 2012.

[118] L. Helt *et al.*, "How does it scale? Comparing quantum and classical nonlinear optical processes in integrated devices," *J. Opt. Soc. Am. B*, vol. 29, no. 8, pp. 2199–2212, 2012.

[119] M. Liscidini *et al.*, "Asymptotic fields for a Hamiltonian treatment of nonlinear electromagnetic phenomena," *Physical Review A - Atomic, Molecular, and Optical Physics*, vol. 85, no. 1, pp. 1–15, 2012.

[120] M. Foster *et al.*, "Broad-band continuous-wave parametric wavelength conversion in silicon nanowaveguides," *Optics Express*, no. 15, pp. 12 949–12 958, 2007.

[121] J. Ong *et al.*, "Efficient cw four-wave mixing in silicon-on- insulator micro-rings with active carrier removal." *IEEE Photonics technology letters*, no. 25, pp. 1699–1702, 2013.

[122] C. Wu *et al.*, "Degenerate four-wave mixing in si quantum dot doped si-rich sinx channel waveguide." *J. Light. Technol.*, no. 34, pp. 1–1, 2016.

[123] D. Grassani *et al.*, "Micrometer-scale integrated silicon source of time-energy entangled photons." *Optica*, no. 2, pp. 88–94, 2015.

[124] V. Almeida *et al.*, "Optical bistability on a silicon chip." *Opt. Lett.*, no. 29, pp. 2387–2389, 2004.

[125] J. Komma *et al.*, "Thermo-optic coefficient of silicon at 1550 nm and cryogenic temperatures." *Appl. Phys. Lett.*, no. 101, pp. 4–8, 2012.

[126] K. Padmaraju *et al.*, "Wavelength locking and thermally stabilizing microring resonators using dithering signals." *J. Light. Technol.*, no. 32, pp. 505–512., 2014.

[127] K. Padmaraju *et al.*, "Integrated thermal stabilization of a microring modulator." *Opt. Express*, no. 21, pp. 14 342–50, 2013.

[128] X. Wang *et al.*, "Narrow-band transmission filter using phase-shifted bragg gratings in soi waveguide." *IEEE Photonics Conf. (Arlington, VA)*, p. paper ThZ1, 2011.

[129] K. Rutkowska *et al.*, "Ultrafast all-optical temporal differentiators based on cmos-compatible integrated-waveguide bragg gratings." *Opt. Express*, no. 19, pp. 19 514–19 522, 2011.

[130] M. Strain *et al.*, "Multi-wavelength filters in silicon using superposition sidewall bragg grating devices." *Opt. Lett.*, no. 39, p. 413, 2014.

[131] M. Strain *et al.*, "Tunable q-factor silicon micro-ring resonators for ultra-low power parametric processes." *Opt. Lett.*, no. 40, pp. 4–7, 2014.

[132] M. Strain *et al.*, "Design and fabrication of integrated chirped bragg gratings for on-chip dispersion control," *Quantum Electron. IEEE J.*, no. 46, pp. 774–782., 2010.

[133] "Arduino website arduino datasheet," https://www.arduino.cc/en/main/arduinoBoardUno, accessed: 2017-05-12.

[134] K. Motzek *et al.*, "Microelectronic Engineering Optimization of illumination pupils and mask structures for proximity printing," *Microelectronic Engineering*, vol. 87, no. 5-8, pp. 1164–1167, 2010.

[135] Crystalaser, "Stabilized Violet-blue 375 nm 405 nm 444 nm lasers - Datasheet." [Online]. Available: www.crystalaser.com/Blue375-405-444.pdf

[136] "Eksma Optics fbs operational instruction," http://eksmaoptics.com/out/media/FBS.pdf, 2016, accessed: 2016-12-10.

[137] A. Fallahkhair *et al.*, "Vector finite difference modesolver for anisotropic dielectric waveguides," *Journal of Lightwave Technology*, vol. 26, no. 11, pp. 1423–1431, 2008.

[138] Y. Murakami *et al.*, "Single mode optical y-branching circuit using deposited silica guides (ds guides)," *Electronics Letters*, vol. 17, no. 12, pp. 411–413, 1981.

[139] T. J. Cullen *et al.*, "Radiation losses from single-mode optical Y junctions formed by silver-ion exchange in glass," *Optics Letters*, vol. 10, no. 4, pp. 134–136, 1984.

[140] H. Sasaki *et al.*, "Theoretical and Experimental Studies on Active Y-Junctions in Optical Waveguides," *IEEE Journal of Quantum Electronics, Vol. QE-14*, no. 11, 1978.

[141] M. Haruma *et al.*, "Electrooptical Branching Waveguide Switches and their Application to $1 \times 4$ Optical Switching Networks," *Journal of Lightwave Technology*, vol. 1, no. 1, pp. 223–227, 1983.

[142] W. Martin *et al.*, "A new waveguide switch / modulator for integrated optics," *Applied Physics Letters*, vol. 26, p. 562, 2016.

[143] T. Ranganath *et al.*, "Ti-Diffused $LiNb0_3$ branched waveguide modulators : Performance and Design," *Journal of Quantum Electronics*, vol. QE-13, no. 4, pp. 290–295, 1977.

[144] W. Burns *et al.*, "Interferometric waveguide modulator with polarization independent operation," *Applied Physics Letters*, vol. 33, no. 1978, p. 944, 2016.

[145] M. Izutsu *et al.*, "Picosecond Signal Sampling and Multiplication," *Journal of Lightwave Technology*, vol. LT1, no. 1, pp. 285–289, 1983.

[146] L. Molterorr *et al.*, "20 GHz Optical Waveguide Sampler," *IEEE Journal of Quantum Electronics*, vol. 19, no. 12, pp. 1877–1883, 1983.

[147] C. Woodward *et al.*, "Wide-Band Electrooptic Guided-Wave Analog-to-Digital Converters," *Proceedings of the IEEE*, vol. 72, no. 7, 1984.

[148] A. Lattes *et al.*, "An Ultrafast All-Optical Gate," *IEEE Journal of Quantum Electronics*, no. 11, pp. 1718–1723, 1983.

[149] G. Testa *et al.*, "A hybrid silicon-PDMS optofluidic platform for sensing applications," *Biomedica Optics Express*, vol. 5, no. 2, pp. 91–96, 2014.

[150] U. Levy *et al.*, "On-chip microfluidic tuning of an optical microring resonator On-chip microfluidic tuning of an optical microring resonator," *Applied Physics Letters*, vol. 88, p. 111107, 2016.

[151] I. Grimaldi *et al.*, "Fabrication and optimization of su-8 microring resonators," *2015 XVIII AISEM Annual Conference*, pp. 29–32, 2015.

[152] Y. Huang *et al.*, "Soft lithography replication of polymeric microring optical resonators," *Optics Express*, vol. 11, no. 20, pp. 1766–1768, 2003.

[153] G. Persichetti *et al.*, "Optofluidic jet waveguide for laser-induced fluorescence spectroscopy," *Optics Letters*, vol. 37, no. 24, pp. 5115–5117, 2012.

[154] F. Villani *et al.*, "Study of the interference effects in an optical cavity for organic light-emitting diode applications," *Optics Letters*, vol. 35, no. 20, pp. 3333–3335, 2010.

[155] I. Grimaldi *et al.*, "Polymer based planar coupling of self-assembled bottle microresonators Polymer based planar coupling of self-assembled bottle microresonators," *Applied Physics Letters*, vol. 105, no. 2014, p. 231114, 2016.

[156] J. Silverstone *et al.*, "Qubit entanglement between ring-resonator photon-pair sources on a silicon chip," *Nature Communications*, vol. 7948, pp. 1–7, 2015.

# Publications and presentations

The following is a full list of peer reviewed journal publications, conference presentations and proceedings papers that resulted and/or are related with this thesis.

## Journals

[1] G. Cantarella and M.J. Strain, "A Micro-Processor-Based Feedback Stabilization Scheme for High-Q, Non-Linear Silicon Resonators", Applied Science, vol.6, no.316, pp.1-9, Oct 2016.

[2] C. Klitis, G. Cantarella, M. J. Strain, M. Sorel, "High Extinction ratio TE/TM selective Bragg grating filters on silicon-on-insulator", in prep. Optics Letters.

[3] G. Cantarella, C. Klitis, M. Sorel, M. J. Strain, "Silicon photonic dual polarisation filters with high rejection ratio for on-chip Four Wave Mixing applications" in prep. Optics Express.

[4] D. Jevtics, J. McPhillimy, G. Cantarella, B. Guilhabert, A. Hurtado, Q. Gao, H. H. Tan, C. Jagadish, M. J. Strain, M. D. Dawson, "Heterogeneous Integration of Semiconductor Nanowire Lasers onto Planar and Flexible Waveguide Systems", in prep. Nano Letters.

## Conferences

[1] K. Charalambos and G. Cantarella and M.J. Strain and M. Sorel,"High Extinction Ratio Polarization Selective TE/TM Bragg Gratings filters on silicon -on - insulator.", 2017 CLEO San Jose Convention Center, San Jose, California, USA, Submitted conference proceeding.

[2] G. Cantarella and K. Charalambos and M.J. Strain and M. Sorel,"Integrated microrings for on-chip filtering and efficient FWM generation", 2016 Photonics North, DOI:

10.1109/PN.2016.7537980

[3] K. Charalambos and <u>G. Cantarella</u> and M.J. Strain and M. Sorel,"Integrated TE/TM grating filters with high extinction ratio", 2016 Photonics North, DOI: 10.1109/PN.2016.7537904.

[4] L. Mcknight and Y. Ding and <u>G. Cantarella</u> and C. Klitis and G. Sharp and L. Meriggi and B.M. Holmes and S. May and M. Sorel and M.J. Strain, "Advances in Integrated Photonics", META16, the 7th International Conference on Metamaterials, Photonic Crystals and Plasmonics, Torremolinos (Malaga), Spain, July 25, 2016 - July 28, 2016.

[5] K. Charalambos and <u>G. Cantarella</u> and M.J. Strain and M. Sorel,"Polarisation selective Bragg filters on silicon-on-insulator", IEEE PRIME 2015, Glasgow, 2015.